



HAL
open science

Numerical Simulation of a Water/Oil Emulsion in a Multiscale/Multiphysics context

Mani Chandan Naru

► **To cite this version:**

Mani Chandan Naru. Numerical Simulation of a Water/Oil Emulsion in a Multiscale/Multiphysics context. Fluid mechanics [physics.class-ph]. EDSorbonne University, 2021. English. NNT: . tel-03469455v1

HAL Id: tel-03469455

<https://hal.science/tel-03469455v1>

Submitted on 10 Apr 2021 (v1), last revised 7 Dec 2021 (v2)

HAL is a multi-disciplinary open access archive for the deposit and dissemination of scientific research documents, whether they are published or not. The documents may come from teaching and research institutions in France or abroad, or from public or private research centers.

L'archive ouverte pluridisciplinaire **HAL**, est destinée au dépôt et à la diffusion de documents scientifiques de niveau recherche, publiés ou non, émanant des établissements d'enseignement et de recherche français ou étrangers, des laboratoires publics ou privés.



École doctorale n° 391 : Sciences mécanique, acoustique,
électronique et robotique de Paris (SMAER)

THÈSE

pour obtenir le grade de docteur délivré par

Sorbonne Université
Spécialité doctorale “Mécanique”

présentée et soutenue publiquement par

NARU Mani Chandan

le 4 février 2021

Numerical Simulation of a Water/Oil Emulsion in a Multiscale/Multiphysics context

Directeur de thèse : **M. Stéphane Popinet**
Co-encadrant de thèse : **M. Guillaume Vinay**

Jury

M. VINCENT Stéphane	Professor Université Paris-Est Marne-la-Vallée	Rapporteur
Mme. CALHOUN Donna	Associate Professor Boise State University	Rapporteur
Mme. LINDNER Anke	Professor PMMH-ESPCI	Examineur
M. WACHS Anthony	Professor University of British Columbia	Examineur
M. FULLANA Jose-Maria	Professor Sorbonne University	Examineur
Mme. DALMAZZONE Christine	Research Engineer IFP Energies Nouvelles	Examineur

Institut Jean Le Rond d'Alembert
Campus Pierre et Marie Curie
Paris, France

IFP Energies Nouvelles
1-4 Avenue du Bois Préau
92852 Rueil-Malmaison

Numerical Simulation of a Water/Oil Emulsion in a Multiscale/Multiphysics context

Naru Mani Chandan

04 February 2021

Acknowledgement

I express my sincere gratitude to my advisors Dr. Stéphane Popinet and Dr. Guillaume Vinay for their immense support, patience, guidance and motivation during my Ph.D. research. I am forever indebted and grateful to my advisors for giving me an opportunity to work with them and investing their valuable time in long knowledgeable discussions resulting in better understanding and new insight into the subject of research. My sincere gratitude towards Dr. Vincke Olivier and Dr. Thierry Becue for their unconditional support at IFPEN. I would like to thank my jury members Dr. Donna Calhoun and Dr. Stéphane Vincent for correcting my manuscript and giving a valuable feedback.

I sincerely thank Prof. Emmanuel de Langre for encouraging me to pursue doctoral studies and Prof. Jean Francois Hetet and Prof. S. D. Pathak for encouraging me to pursue a career in research.

I am very much thankful to my colleagues Anand Kumar, Nelson Joubert, Dr. Imane Yalaoui, Constance Clément, Pierre Maltey, Dr. Philippe Gilbert, Dr. Loic Passard, Dr. Camilo Castro Lopéz, Dr. Zaineb Zaafouri, Rajesh Kumar and many others for their knowledgeable and fun discussions. My sincere thanks goes to Catherine Bergot and Simona Otarasanu for their continuous administrative support during my Ph.D.

It would have been impossible to make this journey without the continuous emotional support of Bappudi Sundar Karthik, Bhavani Prakash and Lalitha Anaparti. I am grateful towards my friends Rakesh, Chandrasekhar, Keerthi, Rohit, Harika, Sushma, Bhargav and Alina for believing in me and encouraging me to do a Ph.D.

Last but not the least, I would like to thank my parents for believing in me and supporting me throughout this journey.

Abstract

Crude oil extraction and production lead to the formation of an emulsion of water and oil (i.e. a multiphase flow). Water and oil must be separated before being conveyed to the process installation or re-injected in the reservoir. Reducing the cost of the separation by optimizing the system requires a good understanding of the physics of emulsions. Emulsions are a multiscale/multiphysics problem involving a wide range of length scales and time scales. In particular, coalescence is a key process to be understood. Due to the difficulty of physical experimentations, numerical simulations of emulsions are appealing to understand coalescence and eventually emulsions.

There are two limiting cases of multiphase flow simulations. One using a single VOF function, which always allows coalescence at the mesh size (numerical coalescence) and the other using different VOF functions for different drops to completely avoid coalescence. For a large number of drops it is computationally expensive to use as many VOF functions as there are drops to avoid coalescence. Based on the idea that drops far enough away from one another can use the same VOF function, an efficient algorithm is developed to avoid coalescence for a large number of drops using only a few VOF functions. Furthermore, these non-coalescing drops can also be tracked over time and allowed to coalesce after the desired amount of contact time. This opens the door for efficient subgrid-scale modelling of the coalescence process.

The qualitative and quantitative analysis of large coalescing and non-coalescing emulsions (domain sizes $\geq 52D$) with $Bo = O(1)$ and $Ar = O(1)$ have shown instabilities with a wavelength independent from the domain size. In coalescing emulsions, initially an instability characterized by the drop diameter appeared, followed by filaments formation controlled by the domain size, with a clear transition between these two characteristic scales. The delay in total settling time of an emulsion is also demonstrated by varying the coalescence time using the control coalescence algorithm.

Contents

Introduction	5
Crude oil	5
Destabilizing techniques	6
Separation techniques	6
Importance of improvement in separation	7
Emulsion, a multiphase problem	8
Multiscale approach of a multiphase simulation	10
The Objective of this PhD	10
1 Physics of Emulsions	12
1.1 Coalescence	14
1.1.1 Approach of drops	15
1.1.2 Contact and deformation	16
1.1.3 Film drainage	16
1.1.4 Coalescence	18
1.1.5 Effect of surfactants	19
1.2 Governing parameters	20
1.3 Experimental state of art	23
1.4 Summary	24
2 Modelling of multiphase flows	25
2.1 Governing equations	25
2.2 Numerical discretization	25
2.2.1 Basilisk	25
2.2.2 Navier-Stokes solver	28
2.2.3 Volume of Fluid method	31
2.3 Unique identification of the drops	33
2.3.1 Principle	33
2.3.2 Implementation	33
2.3.3 Algorithm	38
2.3.4 Some limitations of the tag function	39
2.4 Avoiding coalescence using VOF	39
2.4.1 Introduction	39
2.4.2 Principle	43
2.4.3 Summary of algorithm and implementation	45
2.5 Controlled coalescence	46
2.5.1 Principle	46
2.5.2 Summary of the algorithm	52

3	Results and analysis	55
3.1	Simulation setup	55
3.2	Evolution of coalescing emulsions	58
3.2.1	Qualitative description	59
3.2.2	Quantitative analysis	65
3.2.3	Effect of resolution on numerical coalescence	73
3.2.4	Effect of domain size in coalescing emulsions	75
3.3	Evolution of the non-coalescing emulsions	84
3.3.1	Effect of the domain size	87
3.3.2	Effect of the resolution	92
3.4	Evolution of the controlled-coalescing emulsions	93
3.4.1	Effect of the drainage time	95
3.5	Impact of the coalescence model on the behaviour of a 100 droplets emulsion	97
3.5.1	Separation front	97
3.5.2	Coalescence frequency	99
	Conclusion and perspectives	102

Introduction

Emulsions are ubiquitous in our daily life from butter, ice cream in the kitchen, shampoo in the wash room to water-in-oil emulsions on oil platforms. Our kitchen is one of the best experimental laboratory to observe emulsions and the processes involved in emulsions. The vinaigrette of the salad dressing, olive oil in water before cooking pasta or cooking some broth, and butter are all emulsions. Take some oil and pour it into the water, stir both of the substances together, and create several oil droplets. Now leave it to settle down. While settling down, observe the behavior of the mixture. We can observe the mixing of existing small droplets, breaking large droplets, and eventually oil separation from water. The physics involved in these processes are complex and not completely understood. The water-in-oil emulsions appearing in the oil platform undergo a similar process as in our kitchen emulsion experiment. Understanding these emulsion processes is essential to improve existing systems in oil platforms such as water/oil separators.

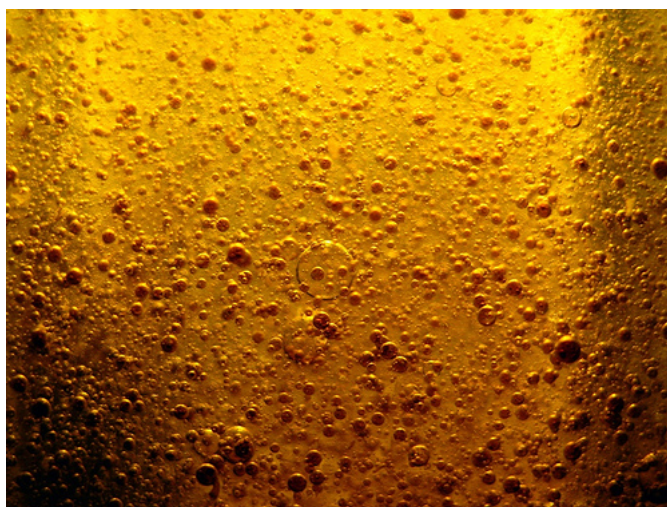


Figure 1: Vinaigrette emulsion, reproduced from [1].

Crude oil

When crude oil is extracted from an oil well, water is recovered along with oil. This is often a water-in-oil emulsion, where water is the dispersed phase and oil is the continuous phase [2]. The dispersed phase comprises multiple drops, whereas the continuous phase corresponds to the phase surrounding the drops. The high shear conditions at the production wellhead form emulsions [3]. The ratio of the volume

of water to the total volume of the fluid produced is called water cut (WC). This water cut increases as the lifetime of the oil well increases. The WC is very high for older oil wells (90%) [4].

Crude oil is composed of the various types of hydrocarbons associated with different polar activities and molecular mass. Oils composition is defined according to the solubility criteria. Crude oils are generally classified as saturates, aromatics, resins, and asphaltenes components. The high stability of emulsions is attributed to the presence of naturally occurring surface-active molecules such as asphaltenes. Crude oil also consists of other surface-active molecules such as resins and fatty acids, which can not stabilize an emulsion alone. Resins make asphaltenes soluble in the continuous phase by moving them away from the interface, destabilizing an emulsion. Whereas some fatty acids such as wax adsorb at the interface, increasing emulsion stability [5]. This stability consequently creates problems in the production and processing of crude oil. The water-oil mixture is often produced as a water-in-oil emulsion.

These emulsions can arise due to the mixing of water and oil from a flow-through porous media, due to the turbulence created in the well head, pressure difference created by choke valves and pipe topology. All of these belong to the oil reservoir structure [4]. The operating specifications demand that water and oil have to be separated before being conveyed to the process installation or re-injected in the reservoir.

Destabilizing techniques

Oil/water emulsions may be highly stable. In stable emulsions, droplets do not coalesce. For separation to occur, they have to be destabilized. The process of destabilization is to allow them to coalesce. There are many studies to understand the mechanism of destabilization of water and oil emulsions [6]. The majority of studies focused on chemically induced destabilization due to the external addition of surface-active molecules. These surface-active molecules influence the interfacial activity, which will promote coalescence.

Separation techniques

There are many ways used to separate water and crude oil. This process can be carried out on either onshore or offshore platforms. When carried out onshore, the space constraints are minimal, considering the cost. Some effort is required to design the onshore separation plant but much less compared to offshore. The space requirements are not a big problem in onshore cases despite being over-dimensioned most of the time. However, offshore separators must be much smaller considering the scarcity of floor space and the material costs. The separation of water and oil is not fully understood yet and it has to be much better understood to help optimizing separators.

Many techniques are available for the separation, such as freezing (cryological technologies) and hydrocyclones [4]. The simple, straightforward, and inexpensive method involves a gravity settler that may be advanced by combining with microwave, ultrasonic, electrostatic, chemical demulsifiers, mechanical barrier (e.g.,



Figure 2: Oil platform, reproduced from [7].

fibrous beds, plates, grids, baffles, etc.), or thermal (heating) means [4]. In the gravity settlers, buoyancy drives the settling and coalescence of the droplets, leading eventually to separation.

The mixing of multiple drops of the same phase to become one drop is coalescence, whereas settling due to gravity is called sedimentation. These two processes are the key governing phenomena in the gravity settlers. These two phenomena can occur simultaneously. This is governed by various factors such as drop diameter, surfactants, water cut, continuous phase viscosity, density ratio between the two phases and surface tension [4].

Importance of improvement in separation

The need to efficiently separate crude oil and water is getting very important. With the technology based on the current understanding of emulsions, the size of the separator is large which will increase the cost. Oil properties such as viscosity and density have a direct effect on the separators. The efficiency of separators has an impact on the price of oil.

The Oak Ridge National Laboratory Review states that, in 2002, nearly half of the oil being consumed in the world was exported from Saudi Arabia at a production cost of approximately 0.80\$ a barrel (Oak Ridge Natl. Lab. 2002) [8] whereas in the United States it costs 10\$ a barrel.

There is a lot of oil available at deeper sections of the earth (1524 meters) at the Gulf of Mexico, which, if it is accessible, will be much larger than that of Saudi Arabia. However, the main problem is that the WC is very high in this case (almost 90%) [8]. To develop technologies or to improve the existing demulsifiers and separation systems, we need a better physical understanding of the key phenomena involved in an emulsion system.

Emulsion, a multiphase problem

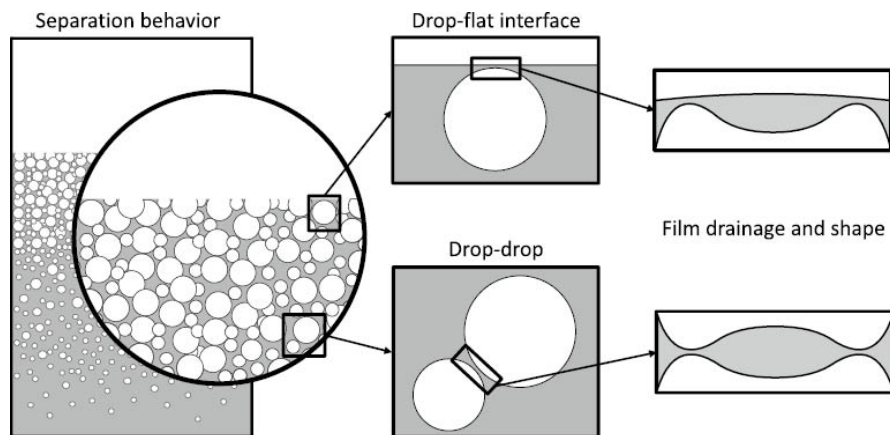


Figure 3: Schematic representation of the separator unit and other important length scales in the system. Reproduced from [9].

An emulsion is a dispersion of one immiscible phase into another. It is a multiphase flow problem, which refers to problems consisting of more than one immiscible phase. This is represented by white and grey colors in Figure 3.

A schematic representation of different length scales in an emulsion is shown in Figure 3. Emulsions involve hydrodynamic phenomena at the emulsion domain size, at the size of the droplet interactions, and interfacial phenomena at the droplet interface as schematically represented in Figures 3, 4 and 5, where the length scales range from nanometer to meter.

We need a better understanding of physical phenomena happening at all these scales simultaneously, to help develop better technologies for demulsification and separation. Despite the advancements in understanding emulsions in the last few decades, we lack technology (experimental techniques, numerical methods, and computational capacity) to study this phenomenon in full detail with high spatial and temporal resolution [8].

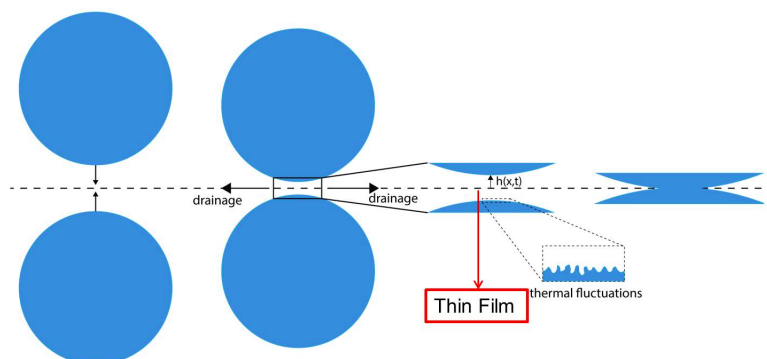


Figure 4: Schematic diagram of the different stages of a coalescence. Reproduced from [10].

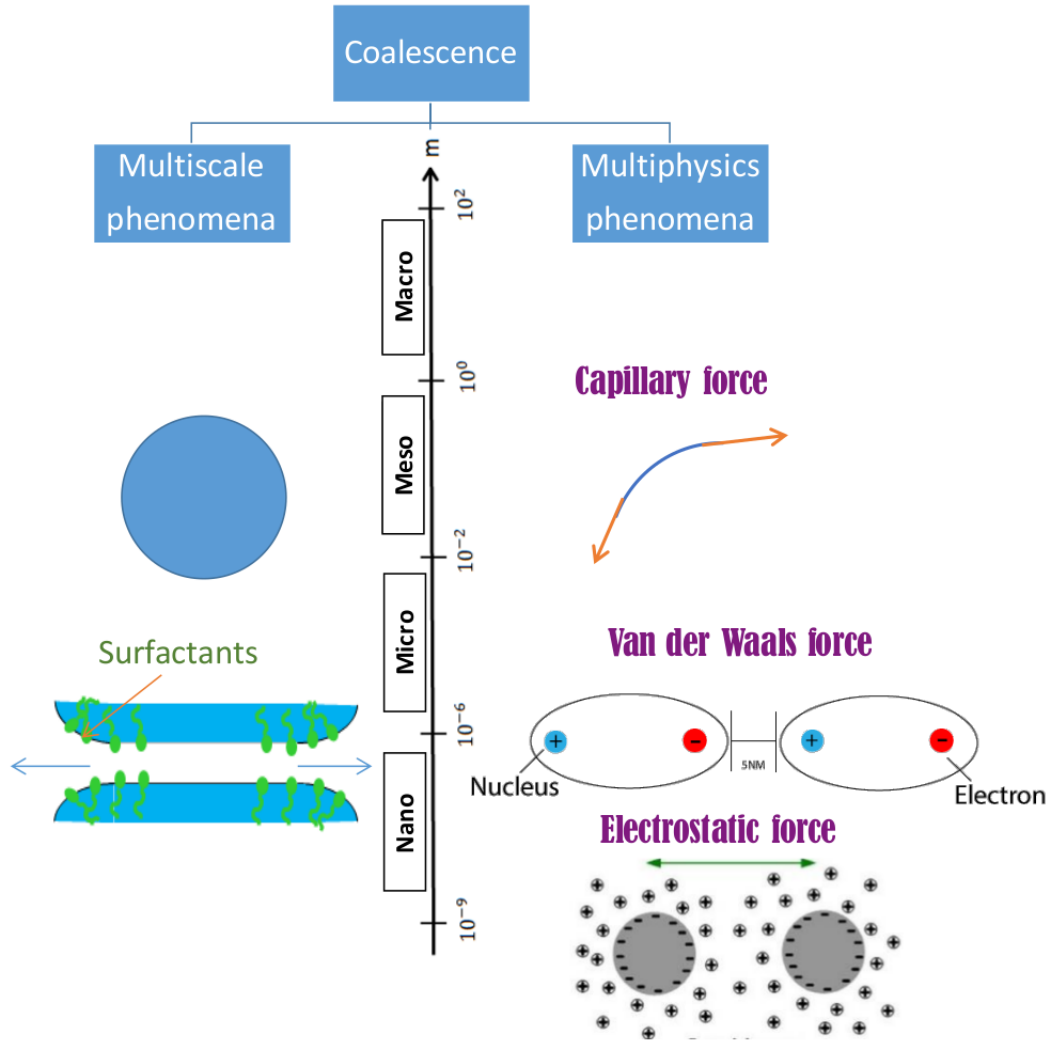


Figure 5: Schematic diagram of the multiscale and multiphysics nature of an emulsion.

Emulsions involves the interaction of drops. When drops approach close to each other, the surrounding fluid of the continuous phase is entrapped between them as a film. This film drains and might lead to coalescence depending upon various factors. The different stages in coalescence are schematically presented in Figure 4.

Coalescence is a complex phenomenon due to the multiscale/multiphysics nature of the problem. A multiscale problem involves multiple length scales at different orders of magnitude that need to be resolved to capture the physics happening at all these scales to represent the whole system accurately. The various length scales and corresponding physics are schematically presented in Figure 5. When drops are approaching each other (but not in contact), the characteristic length scale is the drop diameter, and the dominant forces acting at this length scale are the hydrodynamic and capillary forces. When drops are in contact (as the film gets drained), short-range forces such as the Van der Waals forces become dominant, and hence must be taken into account.

Given all the properties and parameters of the system, no unified model exists to

predict coalescence characteristics. Answers to some of the fundamental questions: how much time does it take for the thin film between drops to drain before coalescence? What are the parameters that control it? are still not known. The effect of surfactants on coalescence and film drainage is still under investigation [8]. There is a greater need for different approaches for understanding emulsions better.

Multiscale approach of a multiphase simulation

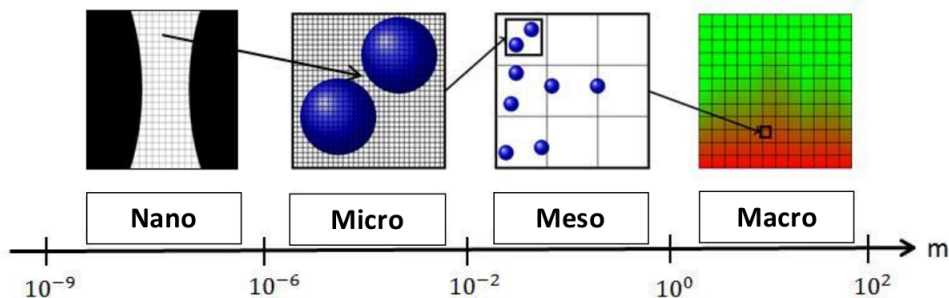


Figure 6: Schematic diagram of the multiscale nature of an emulsion.

Numerical simulations allow us to perform controlled experiments which then lead to a better understanding of physical phenomena. An emulsion is a multiphase problem. The numerical methods for multiphase flows have been developed tremendously in the last few decades. Numerical simulations allow one to get a good picture of phenomena that are hard to visualize experimentally. It is challenging to tune the control parameters for emulsion experiments, whereas it can be easier to do this through numerical simulations.

The main difficulties in simulating emulsions arise due to the resolution of various scales involved in the flow and the different physics interacting at these scales (from the colloidal forces acting at the molecular level to the hydrodynamic forces acting at the flow scale). The scale involved in the industry is the macroscopic scale, which is the scale involved in designing the separator. However, the physical interactions at the smaller scales will influence the behavior at macroscopic scales.

The fluid flow system under the continuum assumption can be modeled using the Navier-Stokes equations. However, in multiphase flows, multiple interfaces may approach very close (length scales of the order of nanometers), which is too small for the continuum assumption to be valid, hence an additional model is necessary to represent the physics at these small scales.

The Objective of this PhD

The main objective of this study is to simulate water/oil emulsions accurately through a multiscale approach. The Basilisk open-source code [11] consists of accurate solvers to simulate multiphase flows, where interfaces are represented with the Volume of Fluid methods (VOF). The coalescence caused by VOF is numerical

and occurs at the order of the computational mesh cell size. A general framework to control coalescence can be developed, if one can avoid this numerical coalescence while using VOF methods and control when they can coalesce.

Modeling of an emulsion is complex due to the multiscale/multiphysics nature of the problem. There is no unique model that accurately represents the physics of the processes involved in an emulsion. Nevertheless, in the process of framing and improving models, given a model representing the physics of the coalescence, it can be used to control coalescence in VOF simulations (first avoid coalescence, then use this model to tell it when to coalesce).

This Ph.D. aims to develop numerical methods to provide a general framework to control coalescence using VOF interface advection.

Chapter 1

Physics of Emulsions

In this chapter, we explain the different processes occurring in emulsions with a specific focus on coalescence. The different stages leading to coalescence and its different influencing factors are summarized. The experimental state of the art of emulsions is summarized.

Emulsion

An emulsion is a dispersion of liquid droplets into another liquid, where these two liquids are immiscible. Here dispersed phase refers to droplet matter and continuous phase to the fluid surrounding the droplet. If water is the dispersed phase, the emulsions are water-in-oil emulsions. Similarly, if the oil is the dispersed phase, it is an oil-in-water emulsion. A microscopic image of a water-in-oil emulsion is shown in Figure 1.1.

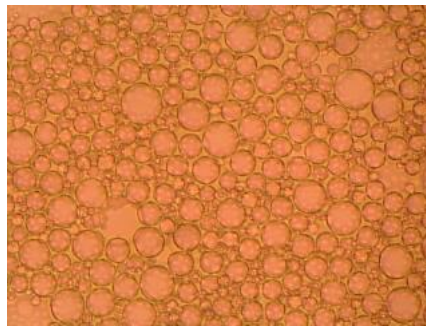


Figure 1.1: The microscale of a water/oil emulsion. Reproduced from [12].

Emulsions may involve various processes such as creaming or sedimentation, aggregation, coalescence, etc. as shown in Figure 1.2. Depending on its properties, an emulsion can stay stable or turns out to be unstable through various processes. True emulsions contain impurities that act as surfactants. Additional surfactants can be added to the emulsions to tune their behavior.

Coalescence

When the drops approach close to each other, the continuous phase between their interfaces can be considered as a thin film, which drains and may lead to rupture under the action of various forces, resulting in coalescence.

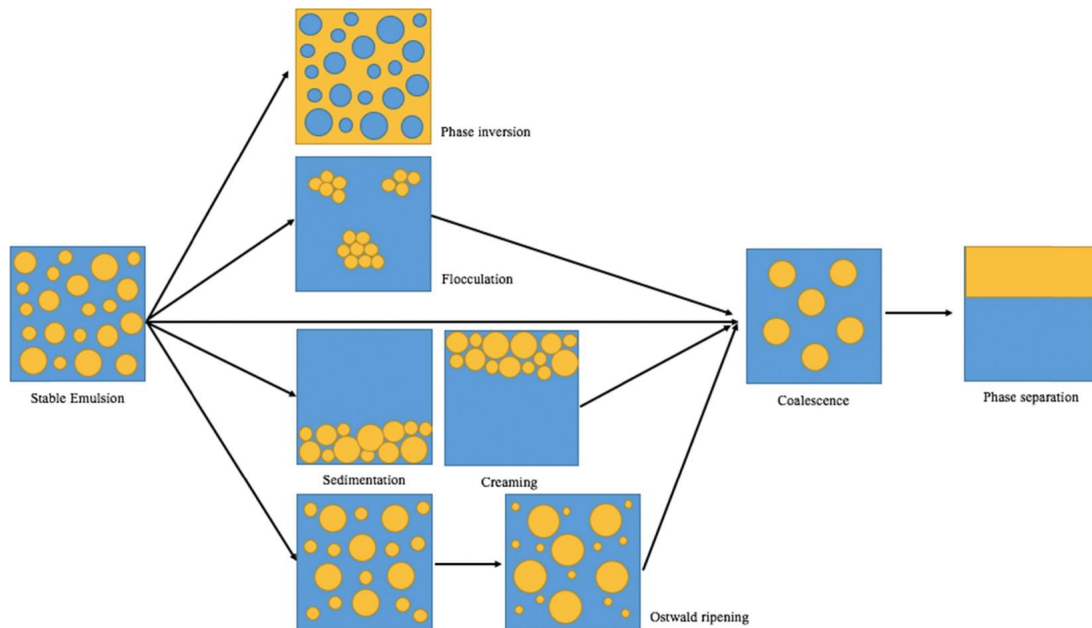


Figure 1.2: Schematic diagram of the emulsion breakdown process. Reproduced from [13].

Sedimentation and Creaming

Sedimentation is the settling of heavier droplets due to negative buoyancy. Larger drops settle faster than smaller droplets. If coalescence is allowed, these smaller droplets coalesce to become larger drops, settling faster. This process is illustrated on Figure 1.2.

Creaming is the opposite of sedimentation. Here the lighter droplets rise under buoyancy as shown in Figure 1.2.

Breakup

For the large droplets, deformation due to the viscous force is quicker than the surface tension response to minimize the deformation. This allows the interfaces to split, leading to the breakup of drops. Breakup of droplets can occur through various mechanisms as shown in Figure 1.3.

Phase inversion

As coalescence proceeds in an unstable emulsion, the continuous phase can get entrapped inside the dispersed phase after coalescence. Accumulation of these effects for many coalescence events will turn the dispersed phase into a continuous phase and the continuous phase into the dispersed phase, as seen in Figure 1.2.

Macro and micro emulsions

Emulsions can be classified according to the length scale of the dispersed droplets. For a macro-emulsion, the mean droplet diameter of the dispersed phase is between $0.3 - 50\mu m$. Micrometric-emulsions contain droplets of less than $0.3\mu m$ average

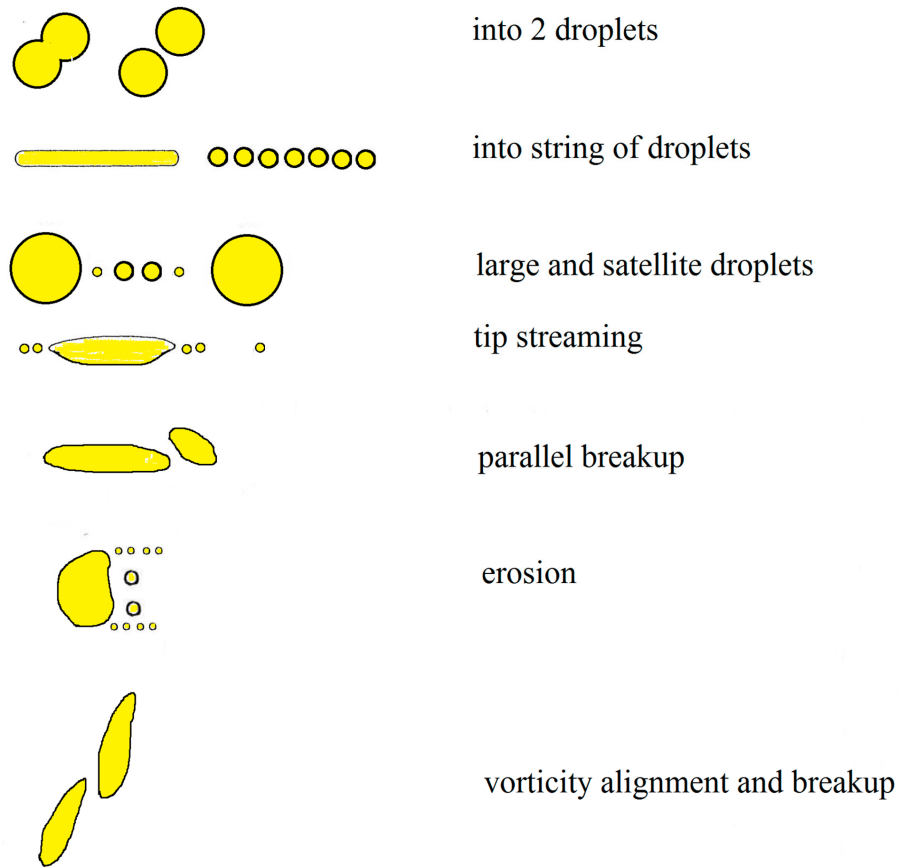


Figure 1.3: Various breakup mechanisms of a drop, reproduced from [14].

diameter, and they are much more stable than macro-emulsions. The droplet size distribution plays an important role in governing an emulsion's behavior by altering the coalescence and breakup [15]. Larger drops experience high shear compared to smaller ones and are more prone to breakup. Smaller drops are more likely to coalesce compared to larger ones (considering all other properties to be the same, larger drops deform more leading to thicker films to drain).

1.1 Coalescence

Coalescence is a crucial phenomenon of emulsions which regulates their stability. It is an irreversible process where two drops of miscible phases collide to become one part. It has been widely studied theoretically, numerically, and experimentally for the past five decades. Nevertheless, some of the fundamental questions are not answered. Coalescence is often described as the following sequence [16, 8, 9]:

1. Approach of drops
2. Contact and deformation
3. Film drainage of continuous phase between drops
4. Coalescence

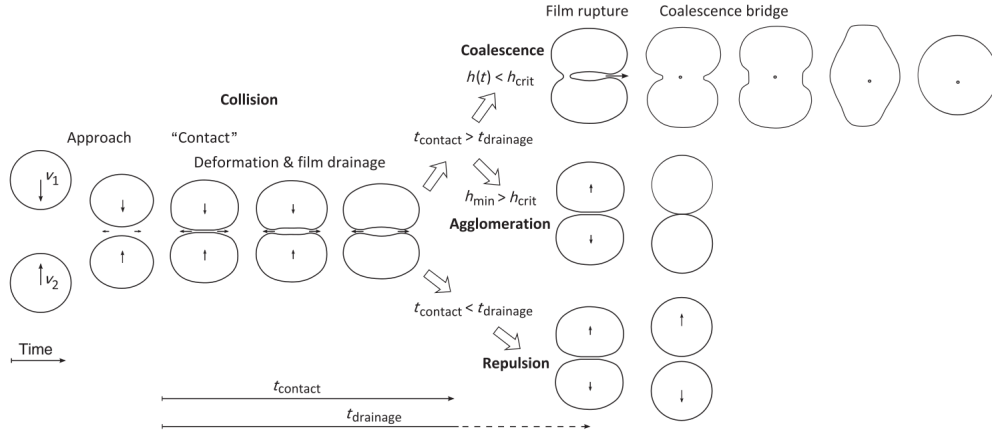


Figure 1.4: Schematic representing the different stages of a collision of a pair of approaching drops, leading to either coalescence, agglomeration or repulsion. Reproduced from [9].

These four stages are schematically illustrated in Figure 1.4 as well as other possibilities of non-coalescence.

Collision of two drops might result in coalescence, agglomeration or repulsion. This is schematically represented in Figure 1.4.

1.1.1 Approach of drops

Drops need to approach each other with some relative velocity as a first step towards coalescence. The relative velocity is determined by either the settling (or rising) velocity of the drops or flow pattern of the dispersed phase.

Emulsion systems may comprise of various flow regimes based on the type of application. In gravity separators, one can observe regions settling or rising drops and stagnant regions of drops closely packed. The settling velocity of the sedimenting drops can be found by balancing the buoyancy with the drag force. The drag coefficient for this balance is proposed by Wegener et al. for single drops, or another corrected coefficient based on volume fraction for aggregation of drops by Henschke et al. [9]. In the densely packed zone, the relative velocity between drops can be negligible despite of velocity fluctuations induced by the coalescence events. A summary of relative velocities in different flow regimes is listed in Figure 1.5.

Drops can interact with each other via head-on or eccentric collisions. When a pair of drops approach each other, the displacement of the continuous phase between them increases. Viscous forces, deceleration and deformation of the drops counteract this motion. This approach leading to a deformation, entraps the continuous phase fluid between drops as a thin film. Investigation of the collision of pairs of drops has shown that this interaction starts when the distance between centers of approaching pair of drops: $s_{interaction} = \frac{3}{4}d_1 + d_2$, where d_1 and d_2 are the drops diameters [9] as shown in Figure 1.6.

Flow Regime	Velocity
Dense-packed zone	$U_{\text{rel}} \approx 0$
Gravity settling	$U = \sqrt{\frac{4}{3} \frac{ \rho_d - \rho_c }{\rho_c} g \frac{1}{C_D}}$
Single droplet	$C_{D,S} = f(Re, \mu_c, \mu_d), Re = \frac{UD\rho_c}{\mu_c}$
Dispersion	$C_{D,\varphi} = f(Re_\varphi, \varphi, \mu_c, \mu_d),$ $Re_\varphi = \frac{UD\rho_c}{\mu_\varphi}, \mu_\varphi = f(\varphi, \mu_c, \mu_d)$
Viscous shear	$U_{\text{rel}} = \dot{\gamma}D$
Capture in larger turbulent eddy	$U_{\text{rel}} = \left(\frac{2\epsilon\rho_c}{15\mu_c}\right)^{1/3}D$
Locally isotropic and homogeneous turbulence	$U_{\text{rel}} = \sqrt{2}(\epsilon D)^{1/3}$

Figure 1.5: Summary of the relative velocities of a pair of drops in different flow regimes, reproduced from [9].

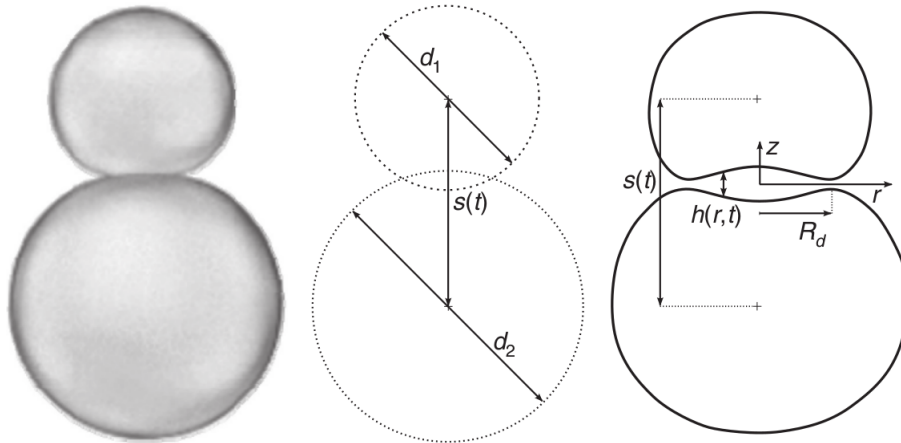


Figure 1.6: The approach and the film drainage of two different sized drops d_1 and d_2 , where $h(r, t)$ is the film thickness and $s(t)$ is the distance between the center of mass of two drops. Reproduced from [9].

1.1.2 Contact and deformation

The contact of drops is defined as the moment at which the distance between their center of mass: $s_{\text{contact}} = \frac{1}{2}d_1 + d_2$ [9]. This is the moment at which they would interact if they were not deformed. They start to deform due to the excess pressure in the thin film entrapped between them.

1.1.3 Film drainage

The entrapment of the continuous phase between dispersed phases is a thin region of fluid. The thin film keeps draining as the drops approach each other, due to the pressure difference over the film's span from the center to the periphery, induced by the change in curvature and the Van der Waals component of colloidal forces.

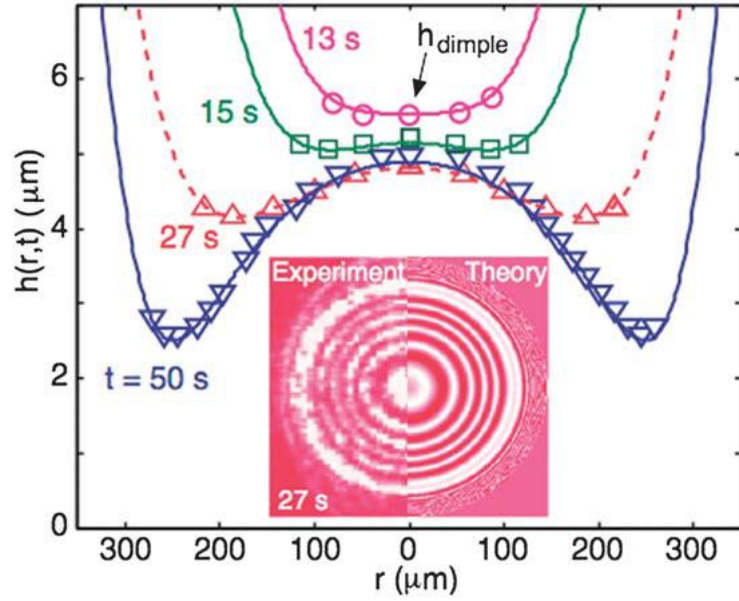


Figure 1.7: The film profile evolution for the glycerol drops dispersed in a silicon oil. The fringe patterns obtained through optical inference of experiments and theoretical results are compared at 27s. Reproduced from [16].

The characteristic length scale of the thin film can be defined as the length between the center of the film until the rim, but Frostad et al. [17] proposed a new length scale based on the length scale associated to the rim region (Ex: The small radius region of the dimpled shape film), which has improved their models corresponding to a thin film.

The evolution of the thin film over time is shown in Figure 1.7. We can see the thickness is lowest not at the center but at the edges, for this kind of dimple deformation.

The viscous force, capillary force, and colloidal forces (Van der Waals forces, electrostatic forces, and steric forces) govern the film drainage. Competition between them decides the shape of the interface of the drop and the thin-film rupture. The shape of the interface can be any of the flat, pimple, dimple or wimple as shown in Figure 1.8. This is decided by the balance between different force acting on the thin film [16].

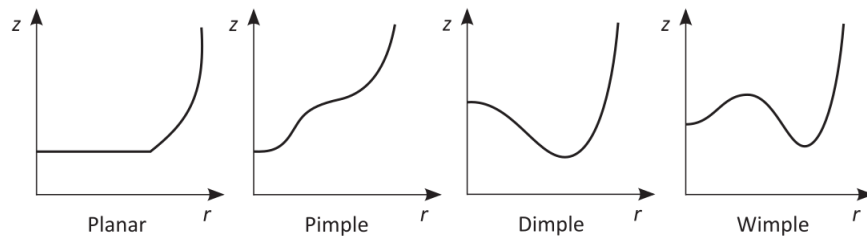


Figure 1.8: Schematic representation of the various possible thin film shapes. Reproduced from [9].

The thin film starts to drain symmetrically but eventually becomes asymmetric, because of the presence of surfactants, which will alter the interfacial tension. The effect of surfactants or some other entities on the asymmetry of the film is still an open research area.

When the drops stop moving, the kinetic energy of the two droplets becomes zero when the deformation reaches a maximum. Surface tension modifies the shape of the drop to minimize the interfacial area. In this process, the drops tend to move away from each other. Despite this motion, film drainage continues for some time t_{drainage} , the time from the contact of the drops until the rupture of the rim. If $t_{\text{contact}} > t_{\text{drainage}}$ (decided by the configuration and competition between various forces acting on it), the film ruptures and the interfaces merge and eventually combine to form a single entity.

1.1.4 Coalescence

Kamp et al. [9] summarize the existing understanding of the reason for film rupture. Usually, it is assumed that the Van der Waals force destabilizes the film leading to rupture. Charles and Mason (1960a) [18] and some other authors have proposed that the interface's surface waves might destabilize the thin film, which is experimentally measured by Aarts et al. (2004) [19]. Aarts and Lekkerkerker (2008) [20] have found that the rupture of the film can be due to thermal capillary waves in a system where Van der Waals forces are weak [9]. Zdravkov et al. (2006) [21] have explained the film rupture due to the Marangoni effect and surface waves. When the dispersed phase molecules are diffused into a continuous phase, these molecules may combine to destabilize the system [9].

From the existing explanations of film rupture, it can be understood that the local small-scale interactions dominate the flow. This subject is still an open area of research. Series of experiments are the way to determine the point and time at which the film ruptures and cannot be explicitly described with the current state of the art [9].

The order of magnitude of the critical film thickness is system-specific. In some cases, thick films destabilize triggering coalescence, but in many cases, the film drains down to order of nanometers before it ruptures. The theoretical analysis predicts the order for film thickness to rupture to a few nanometers, whereas the experimental literature mentions the order ranging from tens to hundreds of nanometers [9].

When the film ruptures, the interfaces meet at some points (over the perimeter of the rim). This linkage is enlarged and expanded by surface tension and expels the remaining film. If the joining and linkage of interfaces are faster than the expulsion of the entrapped continuous phase, part of the film is entrapped as a drop inside the coalescing drops. Figure 1.9 shows high speed images of film rupture between two drops, where we can observe the expansion of the rim radius.

After coalescence, the drop oscillates due to capillary action until it gets stabilized, where the viscous effects dampen the oscillations.

Coalescence time is usually defined as $t_{\text{coalescence}} = t_{\text{drainage}} + t_{\text{rupture}}$, which is the time from the contact until the fusion of interfaces. In general, $t_{\text{drainage}} \gg t_{\text{rupture}}$.

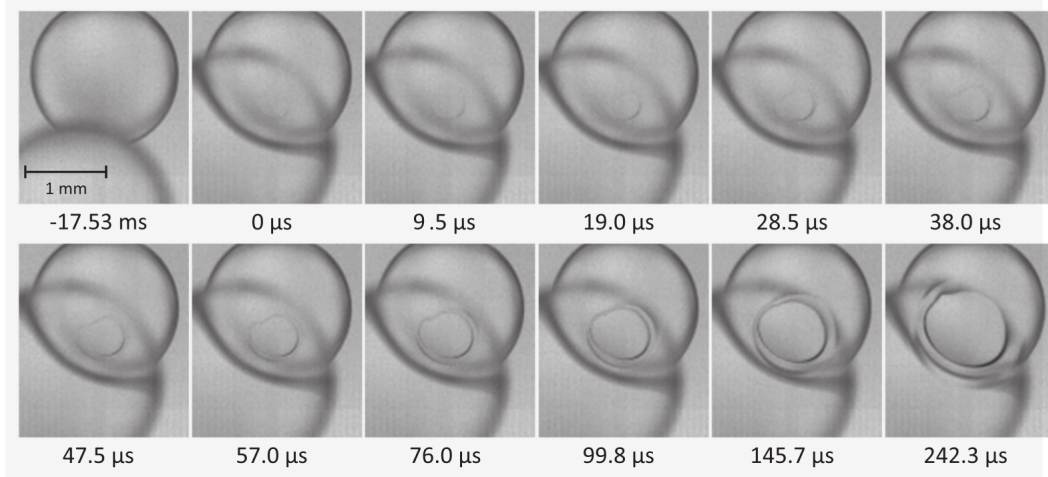


Figure 1.9: The experimental images of the film rupture evolution of toluene drops in water. Reproduced from [9].

1.1.5 Effect of surfactants

Real emulsions always contain impurities known as surfactants. Several types of surfactants can be added to regulate the stability of an emulsion. They adsorb on the interface, trying to alter the surface tension despite being present in very small quantities. Various intermolecular and surface forces are responsible for these effects.

Upon the addition of surfactants, the interfacial tension may vary. As we increase the concentration of surfactants, the interfacial tension keeps decreasing until a limit of concentration is reached. This limit is known as the critical micellar concentration. From this limit, the adsorption of surfactants on the interface will become saturated. Further addition of surfactants does not adsorb at the interface leading to the formation of the aggregates called micelles [22]. The details briefed above are presented in Figure 1.10.

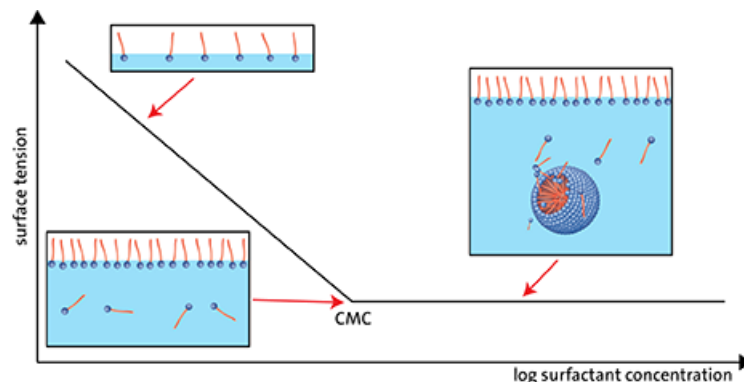


Figure 1.10: Representation of the surface tension variation with surfactant concentration, reproduced from [22].

Two reasons can explain how surfactants can prevent coalescence:

1. As they adsorb at the interface on both of the interacting drops, they approach very close due to steric forces (electrostatic forces). A surfactant repels from other surfactants, thereby preventing the coalescence [23].
2. The distribution of surfactant molecules on the interface of drops is not uniform. This creates a surface tension gradient developing Marangoni stresses, which will start redistributing the fluid back to a thin film. The film thickness starts increasing until the Marangoni stresses balance the hydrodynamic forces and eventually prevents the film drainage, thereby preventing coalescence [23].

Janssen et al. [23] perform boundary integral simulations with insoluble surfactant. Their results are shown in Figure 1.11. Here the minimum film thickness as a function of time is shown for different dimensionless surfactant amounts x . The surfactant amounts are scaled with a theoretical maximum. The increase in the surfactant concentration have developed thicker films which does not favour coalescence.

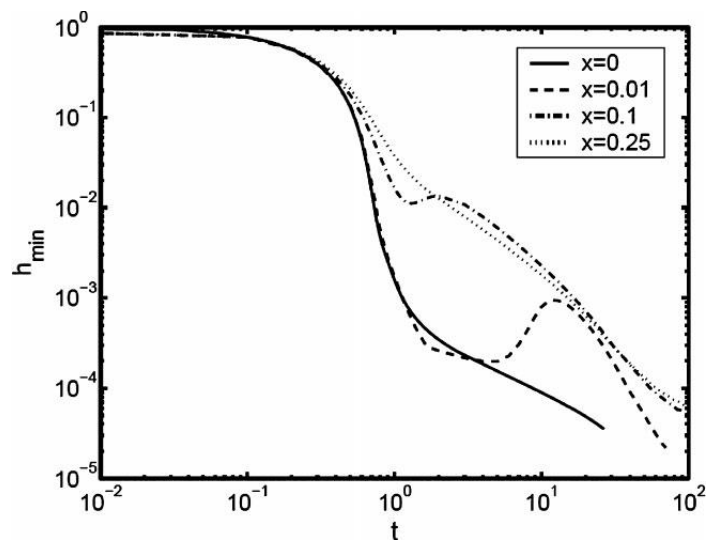


Figure 1.11: Minimal film thickness evolution between two drops in the presence of surfactants. x denotes the surfactant concentration scaled by the theoretical maximum. Reproduced from [23].

1.2 Governing parameters

Various dimensional parameters influence the coalescence process. Figure 1.12 schematically represents the various influencing factors of an emulsion, where the influencing parameters of each phase and interface are listed.

Dimensionless numbers play an important role in classifying and characterizing the system. They can be used to frame different regimes under which the concerned physical phenomena fall. In multiphase flow problems, there are well known dimensionless numbers which are often used. These are summarized in 1.1.

Continuous phase	Interface	Disperse phase
Viscosity	Interfacial tension	Viscosity
Density	Surface potential	Density
Energy input/velocity	Surface active components: surfactants, particles, ions	Drop diameter
Flow pattern/regime	Mass transfer	Ionic strength, pH (if aqueous)
Ionic strength, pH (if aqueous)		
Ambient and system conditions		
Temperature, pressure, geometry, surface wetting, electrostatic field, microwaves, ultrasound		

Figure 1.12: Different properties governing the coalescence process. Reproduced from [9].

	Dimensionless parameters	
Reynolds number = Re	$\frac{\rho_c U D}{\mu_c}$	
Archimedes number = Ar	$\frac{\rho_c \Delta \rho g D^3}{\mu_c^2}$	
Bond number = Bo	$\frac{\Delta \rho g D^2}{\sigma}$	
Capillary number = Ca	$\frac{U \mu_c}{\sigma}$	
Ohnesorge number = Oh	$\frac{\mu_c}{\sqrt{\rho_c \sigma D}}$	(1.1)
Weber number = We	$\frac{\rho_c D U^2}{\sigma}$	
Morton number = Mo	$\frac{\Delta \rho g \mu_c^4}{\rho_c^2 \sigma^3}$	
Marangoni number = Ma	$\frac{d\sigma}{dx} \frac{\Delta x}{\mu_c U}$	
Density ratio = ρ_r	$\frac{\rho_d}{\rho_c}$	
Viscosity ratio = μ_r	$\frac{\mu_d}{\mu_c}$	
Dimensionless Van der Waals attraction = F_γ	$\frac{H}{6\pi\sigma D^2}$	

The coalescence process is a complex multiscale and multiphysics problem, which involves time scales and length scales of several orders of magnitude, making it difficult to have simple, functional relationships between dimensionless numbers.

The Reynolds number is defined as the ratio of the diffusion time scale to the inertial time scale. In buoyancy-driven flows, the equivalent of the Reynolds number is the Archimedes number, where the characteristic velocity scale is based on buoyancy. When $Re \gg 1$, inertia dominates the viscous forces, for $Re \ll 1$ diffusion dominates inertia. Leal and coworkers [17, 24, 25], have worked on low Reynolds

flows. For these regimes, they have found the influence of different parameters on the coalescence and tried to find co-relationships between them. The capillary number is defined as the ratio of the capillary time scale to the diffusion time scale. In the low Reynolds regime, they have found a critical capillary number beyond which drops are repelled [9].

The capillary number also characterizes the breakup process. If the deformation due to the viscous forces is quicker than the surface tension response to minimize the deformation, the interface eventually breaks up. Another dimensionless number that characterizes the breakup process is the Weber number, defined as the ratio of the capillary time scale to the inertial time scale.

An increase in viscosity of the continuous phase decreases the film drainage and may lead to repulsion. The viscosity of the drop phase influences the internal circulation of the drops, which will affect the amount of shear stress acting on the thin film from inside the drop and influence the film drainage process. The higher the internal circulation, the higher the delay of the film drainage [25].

The viscosity ratio is defined as the ratio of the diffusion time scale of the drop phase to the continuous phase. It has a significant effect on the film drainage process. A high viscosity ratio delays the drainage process. In diffusion dominated flows, there is a limit of viscosity ratio, beyond which the drops coalesce while they are being pulled apart by the continuous phase [9]. The density of the continuous phase influences the film drainage process. The larger the density, the slower the drainage process [9]. The density difference between the drop phase and the continuous phase becomes important in buoyancy-driven flows.

The Bond number is defined as the square of the ratio of the characteristic length scale (drop diameter, D) to the capillary length scale ($\lambda_c = \frac{\sigma}{\rho_d g}$). It characterizes the drop deformation due to gravity. Drops with $Bo > 1$ are deformable compared to $Bo < 1$, where drops are intact. When drops are highly deformable, the length span of the film drainage will increase, resulting in longer drainage time. For slightly deformable drops, the film is smaller, and the probability of coalescence is high.

When drops are too close (thin-film length scale of about nm), the Van der Waals forces start to outplay other forces. It is important to introduce a dimensionless number comparing the strength of Van der Waals force to other existing dominant forces. At small scales, the capillary force outweighs other hydrodynamic forces, hence the dimensionless Van der Waals force is defined as the ratio of the Van der Waals attraction to the capillary force.

The interfacial tension could vary across the interface due to various factors such as change in temperature, presence of surfactants etc. This will induce flow along the interface resulting in the Marangoni effect, characterized by the Marangoni number 1.1, where $\frac{d\sigma}{dx}$ is the interfacial tension gradient. Kavezpour et al. [8] have characterized coalescence with the Ohnesorge number, which is defined as the ratio of the diffusion time scale to the Rayleigh time scale (based on both inertia and surface tension). For $Oh \ll 1$, the coalescence process is dominated by capillary and inertial forces. In this case, the timescale is the inertial time scale known as the Rayleigh time scale, defined as $T_i = \sqrt{\frac{\rho_c D^3}{\sigma}}$. When $Oh > 1$, the timescale is the diffusion timescale, defined as $T_\mu = \frac{\mu_c D}{\sigma}$. When $0.2 < Oh < 1$, both inertial and diffusion time scales have the same value, both of them contribute to the resisting force in the coalescence process [8].

1.3 Experimental state of art

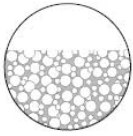
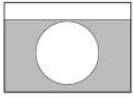

	Test system	Experimental set-up	Measurement technique	Quantity/ result
↑ Level of detail Level of complexity ↓		Settling test (batch or continuous)	Laser diffraction (High-speed) imaging Infrared Magnetic resonance imaging Ultrasound	Layer structure/composition/height Settling behavior/time Drop size distribution
		Static (resting drop) Dynamic (approaching drop)	High-speed imaging PIV Interferometry	Serial examinations Coalescence probability Relative velocity/flow field
		Static (opposing or adjacent drops) Dynamic (fixed drop – approaching drop or two moving drops)	High-speed imaging PIV Interferometry TFB SFA AFM	Detailed examinations Film shape/(critical) film thickness Coalescence time/contact time Drainage behavior/time Interacting forces

Figure 1.13: Different experimental techniques to characterise the evolution of a coalescing emulsion. Reproduced from [9].

Historically, emulsion and coalescence experiments are performed in a few configurations as listed in Figure 1.13, where the different experimental setups used along with measurement techniques and obtained results are summarized [9].

Three categories of tests are summarized: Settling, Drop-flat interface, and Drop-drop tests. One of the main difficulties in dealing with emulsions of drop-interface or drop-drop experiments is to control parameters. Experiments concerned with real scenarios involve surfactants whose effect is very sensitive to coalescence. Several experiments can be conducted for a given set of parameters to find a fitting parameter for coalescence. Nevertheless, it can not give a unique model representing coalescence for any given set of parameters due to the difficulty in reproducing the experiments [9].

The majority of experiments to understand coalescence are static drop interaction experiments. It is not easy to experiment with a controlled dynamic drop-drop interaction experiment. However, in real systems, both static and dynamic interactions occur. It is necessary to further investigate dynamic drop-drop interactions to better understand processes involving coalescence [9].

Another difficulty is to capture the film rupture and bridging processes before coalescence, because the film rupture timescales are very small (compared to the drainage time) [8]; there is room for improvement in the experimental state of the art to capture the film drainage process and the film rupture accurately.

1.4 Summary

An emulsion is a dispersion of one immiscible phase into another. It involves several processes which occur on very different space and time scales. Among all of these processes, coalescence is our subject of interest.

When a drop approaches a surface or another drop, the pressure between them starts increasing, thereby decelerating the drop. It builds up a maximum to the static Laplace pressure. Due to an increase in the pressure between the drops, the interface deforms locally into dimple, pimple, wimple, or flattened shapes. The shape depends on the non-dimensional numbers such as capillary number, Weber number, and dimensionless Van der Waals constant [23].

By this time, the drops are very close, and the entrained fluid between them acts as a thin film, whose length scale might be in the order of micrometers. This thin film keeps draining as the drops approach each other, where viscous forces dominate.

The interfaces are surrounded by surfactants, which can alter the surface tension along the interface, inducing a tangential surface tension gradient. There can be charged particles, inducing electrostatic forces. At molecular length scales, Van der Waals forces due to the interaction of molecules start to play a role.

As the film drains, competition between various forces on the thin film should decide its fate to rupture or repel of the drops, subsequently leading to coalescence or non-coalescence.

Dimensionless numbers such as Bond, Archimedes, Weber, capillary, Ohnesorge, Marangoni numbers, density ratio, viscosity ratio, and Van der Waals attraction, characterize various aspects of the coalescence process.

The experimental state of the art has advanced significantly over a few decades. Nevertheless, due to the nature of the problem and the existence of very small length and time scales, there is much more to explore and improve. Another difficulty is the sensitivity of the surface tension coefficient to the presence of surfactants, which creates difficulty in attaining consistent results through repetition of experiments.

In the coming chapter, we will model the multiphase flows (Navier-Stokes equations) and subsequently solve these models numerically.

Chapter 2

Modelling of multiphase flows

In this chapter the governing equations of an emulsion and the numerical methods used to solve them are summarized. The new functions to avoid and control the coalescence in emulsion simulations are explained.

2.1 Governing equations

Fluid flow problems can be modelled using the Navier-Stokes equations when considering that the characteristic length scales of the system are larger than the molecular length scale. An incompressible multiphase flow with constant temperature can be modelled as a single set of Navier-Stokes equations for the whole domain with variable density and viscosity as follows.

$$\rho \left(\frac{\partial \mathbf{u}}{\partial t} + \mathbf{u} \cdot \nabla \mathbf{u} \right) = -\nabla \cdot p + \nabla \cdot (2\mu \mathbf{D}) + \rho \mathbf{g} + \sigma \kappa \delta_s \mathbf{n} \quad (2.1)$$

$$\frac{\partial \rho}{\partial t} + \nabla \cdot (\rho \mathbf{u}) = 0 \quad (2.2)$$

$$\nabla \cdot \mathbf{u} = 0 \quad (2.3)$$

where ρ is the density and μ the viscosity, which depend explicitly on the interface location. This is also known as a one-fluid approach. Here we model the deformation rate tensor \mathbf{D} in the viscous term as follows:

$$\mathbf{D} = \frac{1}{2} [\nabla \mathbf{u} + (\nabla \mathbf{u})^T] \quad (2.4)$$

The gravitational force is introduced as a source term, where \mathbf{g} is the acceleration due to gravity. Surface tension is introduced as $\sigma \kappa \delta_s \mathbf{n}$ in the framework of the Continuum Surface Force method [26], where σ is the surface tension coefficient, κ and \mathbf{n} are the local curvature and local normal to the interface respectively. δ_s is a surface Dirac delta function which is non-zero on the interface and zero elsewhere.

2.2 Numerical discretization

2.2.1 Basilisk

[Basilisk](#) is an open-source code that solves the partial differential equations on Cartesian meshes. It is primarily developed by [Stéphane Popinet](#) and also contributed by other [authors](#).

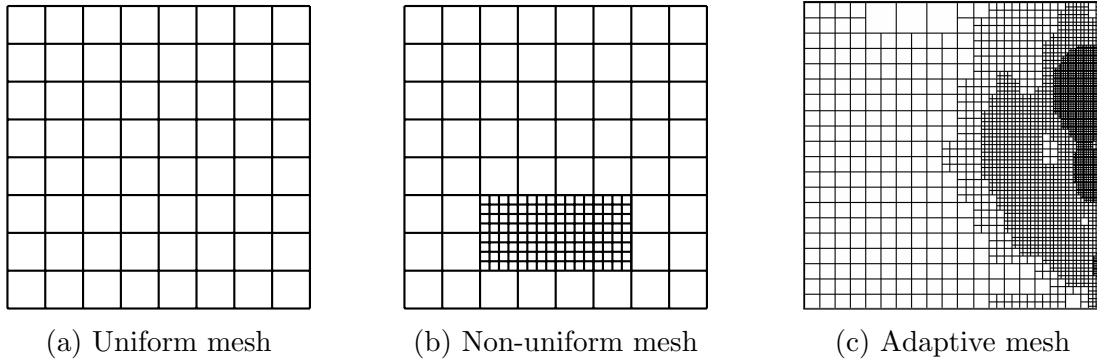


Figure 2.1: Different types of mesh available in Basilisk.

Mesh

Basilisk uses finite-volume based methods to solve the governing partial differential equations known as the Navier-Stokes equations. To convert the partial differential equations into algebraic equations using numerical methods, one needs to split the whole domain into multiple finite-volume elements known as cells, by choosing an appropriate shape and size distribution across the domain. This decomposition of the domain is known as a mesh. Basilisk uses Cartesian meshes, which are composed of squares in two dimensions and cubes in three dimensions. The simplest possible mesh is the uniform Cartesian mesh, where all the volume elements in the domain are of the same size, as shown in figure 2.1a. This allows one to compute the solutions of differential equations at points (associated with volume elements) distributed uniformly across the domain. Basilisk also allows users to use variable-resolution meshes through two strategies.

Non-uniform Cartesian mesh

In this kind of meshes the volume elements spanning the domain will be of different sizes as shown in figure 2.1b.

Adaptive Cartesian mesh

This is also kind of non-uniform mesh, but it dynamically evolves based on the solution of the problem. Many fluid problems span a wide range of length scales, which also evolve over time. To resolve these scales, one would need to use a fine uniform Cartesian mesh, which can be prohibitively expensive. This problem can be solved by introducing a variable mesh resolution, where the small length scale regions of the domain are finely resolved compared to the large length scale regions, as shown in figure 2.1c. There are multiple ways to achieve this. Basilisk uses Quad/Octree grids which provide variable resolution as shown in figures 2.1c and 2.2.

Field

Basilisk uses the notion of a field in relation to the concept of fields in physics. Here a field A , represents the values of A associated with all the volume elements in which the differential equations are solved. Basilisk provides scalar, vector, and

tensor fields defined at the center of the cells. Where a vector field is a collection of n scalar fields, similarly a tensor field is a collection of n vector fields, where n is the number of dimensions. It also defines face and vertex field options, which can be useful for non-centred staggering.

Quad/Octree Grids

The idea of adaptive mesh refinement using Quadtrees (in two dimensions) is to refine the existing cell into four equal square cells when some criteria are met, similarly Octree for three dimensions, where the existing cell is refined into eight equal cubic cells. The entire domain is a single volume element or single cell located

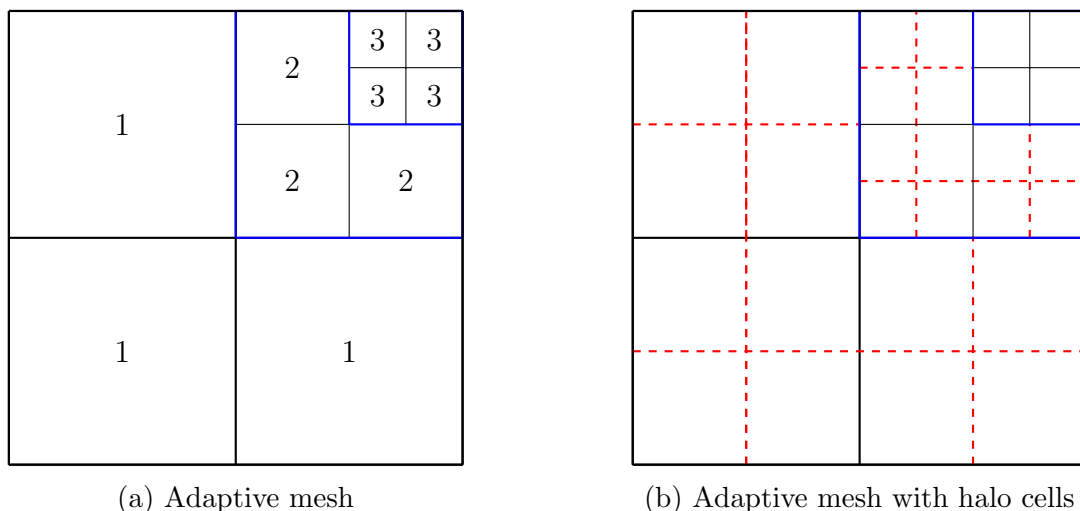


Figure 2.2: Quadtree adaptive grid.

at level 0 and is denoted as the *root cell*. This whole domain is then split into four equal square cells, these newly split cells are located at level 1. When any of these four cells located at level 1 is split further into four equal square cells, these new cells are located at level 2. Further repeating this will lead to higher levels. Basilisk associates each cell in its domain to a level as shown in figure 2.2a. This process can be directly extended to octree, where a cell located at level l gives 8 cells at level $l+1$. In general a cell at any level l will have 2^D children at level $l+1$, where D is the number of dimensions. Cells at level $l+1$ obtained from refinement of cell at level l are denoted as *children* at $l+1$ obtained from a parent at level l , which are easily accessible in Basilisk as shown in figure 2.3 by using `coarse(t,i,j)` and `fine(t,i,j)` to find parent and children respectively. The finest possible cells are called *leaf cells*, for example in figure 2.1c all of the cells are leaf cells with their respective levels labelled on them.

In *Quad/Octree* mesh there can be cells neighbouring other cells at different levels, these boundaries are known as *resolution boundaries* as shown by the blue coloured lines in figure 2.2. We might need to use the children of leaf cells at resolution boundaries in order to maintain the consistency of the stencil operations. Children of leaf cells are denoted as *halo cells*, which are shown by cells bounded by red dotted lines in the figure 2.2b. One special case of *Quad/Octree* grid is a *Multigrid*. This associate grids at all levels until the finest level where there are no

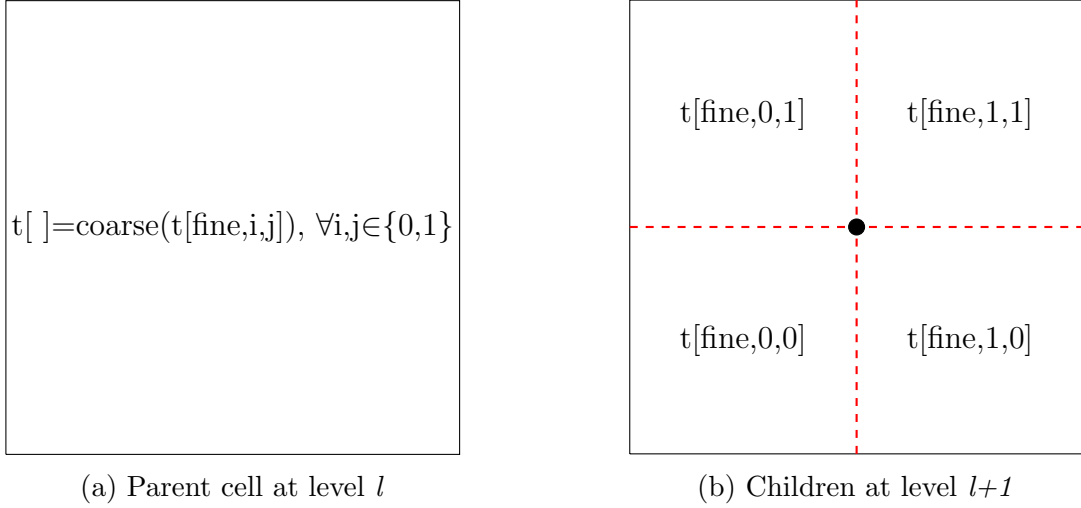


Figure 2.3: Children of a coarse cell.

resolution boundaries. A multigrid at level l at the maximum resolution will have $2^{l \cdot D}$ number of cells, where D is the number of dimensions.

Basilisk provides grid iterators to loop through all the cells of the mesh. `foreach()` iterator loops through all of the leaf cells, whereas `foreach_level(l)` iterates through all of the cells located at level l . It also provides stencil iterators such as `foreach_neighbor()`. At a given cell this iterator allows to loop through 3x3 or 5x5 stencils centred on that cell in 2D. This is also functional in 3D. `foreach_child()` iterates through all the children of each parent cell. While using any of these iterators, for any scalar f , using `f[]` we can access and modify the f value at the current cell in the iteration.

2.2.2 Navier-Stokes solver

A staggered in time and collocated in space discretization of the incompressible variable density Navier-Stokes equations implemented in Basilisk are second-order accurate in space and time. The detailed explanation of the different steps and methods in this solver can be referred at [27, 28, 29], hence they are briefly touched upon here:

The staggered in time discretization of the momentum equation 2.1, incompressible condition 2.3 are as follows:

$$\rho_{n+\frac{1}{2}} \left(\frac{\mathbf{u}_{n+1} - \mathbf{u}_n}{\Delta t} + (\mathbf{u} \cdot \nabla \mathbf{u})_{n+\frac{1}{2}} \right) = -\nabla p_{n+\frac{1}{2}} + \nabla \cdot [\mu_{n+\frac{1}{2}} (\mathbf{D}_n + \mathbf{D}_{n+1})] + \mathbf{a}_{n+\frac{1}{2}} \quad (2.5)$$

$$\nabla \cdot \mathbf{u}_n = 0 \quad (2.6)$$

Where \mathbf{a} refers to source terms such as gravity etc.

The approximate projection method of the discretized Navier-Stokes equations results in the following steps to solve the velocity field:

$$\frac{\mathbf{u}_* - \mathbf{u}_n}{\Delta t} + (\mathbf{u} \cdot \nabla \mathbf{u})_{n+\frac{1}{2}} = \alpha_{n+\frac{1}{2}} \nabla \cdot [\mu_{n+\frac{1}{2}} (\mathbf{D}_*)] \quad (2.7)$$

$$\alpha = \frac{1}{\rho} \quad (2.8)$$

Here "★" corresponds to the auxiliary fields. Overline corresponds to the cell-center to cell-face (superscript f) averaging and vice versa.

Advection

The advection term $(u \cdot \nabla u)_{n+1/2}$ is discretized using the unsplit, upwind, second-order accurate scheme of Bell-Collela-Glaz [30]. This leads to a timestep restricted by the CFL condition.

Diffusion

The second order accurate in space implicit viscosity solver is used to discretize the diffusion term $\nabla \cdot (\mu \nabla D)_*$. It is unconditionally stable.

Acceleration

$$\mathbf{u}_*^f = \overline{\mathbf{u}_*} + \Delta t \mathbf{a}^f \quad (2.9)$$

Projection

$$\mathbf{u}_{n+1}^f = P(\mathbf{u}_*^f, p_{n+1}) \quad (2.10)$$

Poisson solver

The multigrid iterations are performed through "half" V-cycle in contrast to the classical implementation. Here instead of correcting the solution (pressure) at different levels, the residual of the pressure at the finest level is corrected at different levels [29].

$$\frac{\nabla \cdot \mathbf{u}_*}{\Delta t} = -\nabla \cdot \left(\frac{\nabla p_{n+\frac{1}{2}}}{\rho_{n+\frac{1}{2}}} \right) \quad (2.11)$$

Centred pressure gradient correction

$$\mathbf{g}_{n+1} = \overline{\mathbf{a}_f - \alpha_f \nabla p_{n+1}} \quad (2.12)$$

$$\mathbf{u}_{n+1} = \mathbf{u}_* + \Delta t \mathbf{g}_{n+1} \quad (2.13)$$

Here \mathbf{g} refers to a pressure gradient.

Surface tension

The surface tension source term in the Navier-Stokes equations is introduced as a volumetric force in the interfacial cells using the CSF method [31]. These formulations are based on a numerical approximation of the surface Dirac function which evaluates the volumetric force as follows:

$$\sigma \kappa \delta_s \mathbf{n} = \sigma \kappa \nabla f \quad (2.14)$$

where the curvature κ is estimated using height functions [26]. Then comes the discretization of ∇ on each side of the Laplace equation, which, when not balanced, may lead to spurious currents (i.e. an artificial velocity field).

The surface tension term is discretized explicitly in time. Hence the time step must be restricted for stability as follows to capture the fastest capillary wave:

$$T = \sqrt{\frac{\rho_m \Delta_{min}^3}{\pi \sigma}} \quad (2.15)$$

$$\rho_m = \frac{\rho_1 + \rho_2}{2} \quad (2.16)$$

Here Δ_{min} refers to the minimum cell size. For flows with low capillary number this timestep can become quite restrictive hindering the practicality of numerical experimentation. Hence there is a greater need for implicit discretization of the surface tension source term. A more detailed description of this issue can be found in [26].

The density is a variable dictated by the interface position. Tracking interface over time will give the density and viscosity fields.

Interface tracking methods

In a multiphase flow simulation, the interface position need to be tracked over time. There are in general two different class of methods to achieve this. In one class, often called as the Front tracking methods, the finite number of marker points are attached to the interface. By updating the position of the marker points using the local velocity field, the interface shape is updated. Despite of its conceptual simplicity, it has significant drawbacks. The advection of the marker points does not guarantee the proper discretization of the interface. Periodical redistribution of the marker points is necessary to maintain an appropriate description of the interface. It can not handle the topological changes such as coalescence and breakup automatically. There are some latest developments such as Local Front Reconstruction Method to circumvent many of the existing problems [32].

The other class of methods known as Front capturing methods uses a direct representation of the interface position to track its evolution. Two notable types in this class of methods are the Level set and the Volume-of-Fluid methods. The level set method introduced by Sethian et al. [33] uses an implicit function representing the interface. Unlike marker methods, this function can be directly discretized on the same mesh as that of the Navier-Stokes solver. By solving an advection equation of this function, we will be able to find the interface position over time. Due to the choice of using a smooth function to represent the interface, it comes in handy while computing the local curvature etc. Despite of its advantage it has a major drawback. It can not guarantee mass conservation due to the degradation of the estimation of the interface position. An additional routine for re-initializing the distance function is necessary.

The Volume-of-Fluid method first introduced by the Hirt and Nichols [34] uses a step function as a sharp discontinuous field to represent the interface. This method gives superior mass conservation compared to others. The coalescence and breakup events occur at the order of the computational cell size.

Some of the hybrid methods are developed to combine the advantages of the different methods. Sussman and Puckett [35] simulated an axisymmetric bubble using a coupling between the Level Set and VOF methods. The main idea behind this coupled method is to accurately represent the interface using the Level Set method and to reduce the error in mass conservation by using a VOF color function.

The description of the different methods can be referred at [36].

2.2.3 Volume of Fluid method

The numerical investigations in this thesis are performed using Volume-of-Fluid methods. In these methods we use the volume fraction (or color function “ f ”) which identifies each fluid and takes value 1 in one phase and 0 in the other phase and some value between 0 to 1 in the cells with an interface.

$$(2.17) \quad f = \begin{cases} 1 & \text{Drop phase} \\ 0 & \text{Continuous phase} \\ 0 < f < 1 & \text{Interface region} \end{cases}$$

The material properties can be expressed as

$$\rho = \rho_d f + \rho_c (1 - f) \quad (2.18)$$

$$\mu = \mu_d f + \mu_c (1 - f) \quad (2.19)$$

For an incompressible flow the mass conservation equation 2.2 turns out to be

$$\frac{\partial \rho}{\partial t} + \mathbf{u} \cdot \nabla \rho = 0 \quad (2.20)$$

Combining equation 2.18 and 2.20 gives an advection equation for the color function

$$\frac{\partial f}{\partial t} + \mathbf{u} \cdot \nabla f = 0 \quad (2.21)$$

The evolution of the interface is tracked by solving this equation. The advection of the color function poses significant numerical challenges despite its apparent simplicity. In some flow configurations it is better to use weighted harmonic mean of the variable dynamic viscosity rather than the weighted arithmetic mean [36]. We use the conservative, non-diffusive geometrical VOF method described in [28]. It follows two steps:

Interface reconstruction

The interface is explicitly reconstructed defragmentedly from the volume fraction field information using the Piecewise Linear Interface Calculation (PLIC) method. The interface segment in each cell is a straight line constructed using the interface normal (\mathbf{n}) and the intercept of the line (α).

$$\mathbf{n} \cdot \mathbf{x} = \alpha \quad (2.22)$$

\mathbf{x} is a position vector measured with respect to the center of the cell. The interface normal \mathbf{n} is computed using Mixed-Youngs-Centered scheme [37]. The α is computed using the volume fraction field and the normal vector. This interface is then advected.

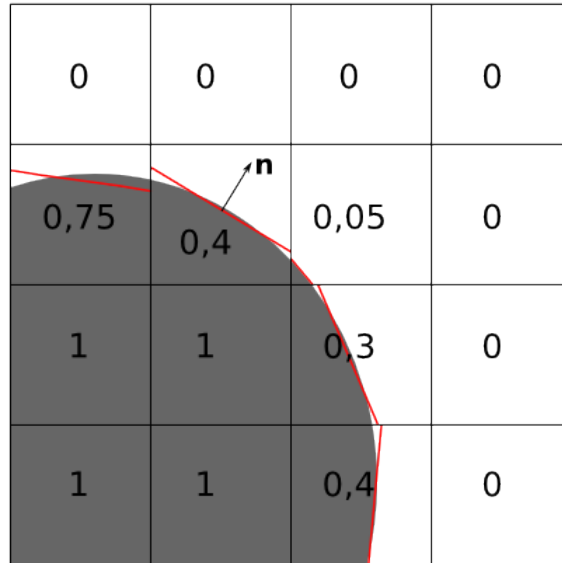


Figure 2.4: The grey colored continuous interface is reconstructed by defragmented red colored lines using PLIC. Reproduced from [38].

Interface advection

The reconstructed interfaces are advected by solving equation 2.21. Where multi-dimensional interface can be advected along each dimension. To update the volume fraction field, fluxes across the cells must be computed. This can be achieved by a geometric flux estimation. The grey area in this simple representative figure 2.5 represents the geometric flux.

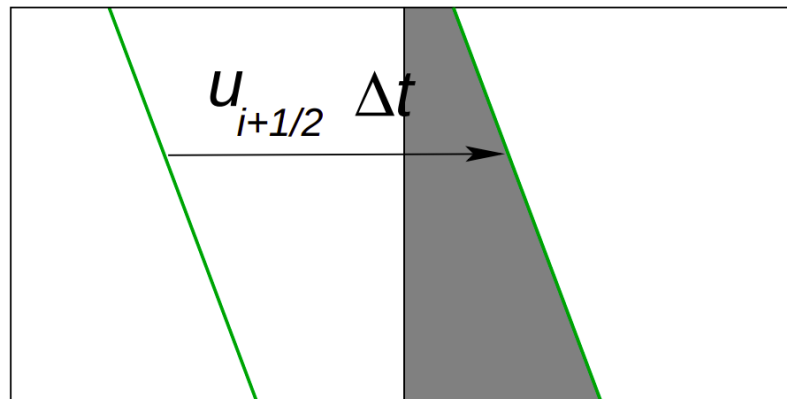


Figure 2.5: The one dimensional advection of the 2D interface. The gray area represents the flux. Reproduced from [39].

The exact mass conservative VOF advection scheme by Weymouth et al. [40] is used to advect the interfaces (This is true when the advection velocity field is divergent free). The stability of the VOF scheme is ensured by setting the CFL to be 0.5.

2.3 Unique identification of the drops

Introduction

Many multiphase flows involve phenomena like breaking and/or coalescence of drops leading to generation of new droplets and/or reduction in the number of existing droplets. Not only the number of droplets has evolved but also their physical features (breakup results in a reduction in volume and coalescence results in an increase in volume). CFD simulations of these multiphase flows may require information about the number of drops and the identity of each drop. This will allow one to maintain the statistics of the number of droplets (also the features of each droplet as we will identify each droplet with a unique index) as simulations evolve. This will also allow one to perform operations on drops, like removing unresolved drops and processing the drops to avoid or delay coalescence, etc.

We use the Volume of Fluid method coupled with a Navier-Stokes solver to resolve and advect the interfaces between multiple phases. Here we do not have any information on the number of droplets as well as a unique way to identify each droplet. This is not trivial to compute. To address this problem we use a tag function $tag()$. This will tag the connected regions with non-zero f (f is the volume fraction field) and associate a unique tag value for each connected region ranging from 1 to n for n connected regions.

2.3.1 Principle

The tag function implementation is described in 2.1. The overall strategy is composed of two steps: first multigrid iterations are used to assign unique tag values to each connected neighborhood (each droplet). These unique values are sorted and stored in an array, where the range of values goes from 1 to the number of leaf cells. In a second step, this range is then reduced to 1 to a number of connected neighborhoods by replacing the unique neighborhood values with their array index.

2.3.2 Implementation

The [tag function](#) takes a scalar field as an input which holds the initial and final tag values. It returns the total number of connected neighborhoods corresponding to the input tag values. Here its implementation is described for a 2D problem, but it can be directly extended to 3D.

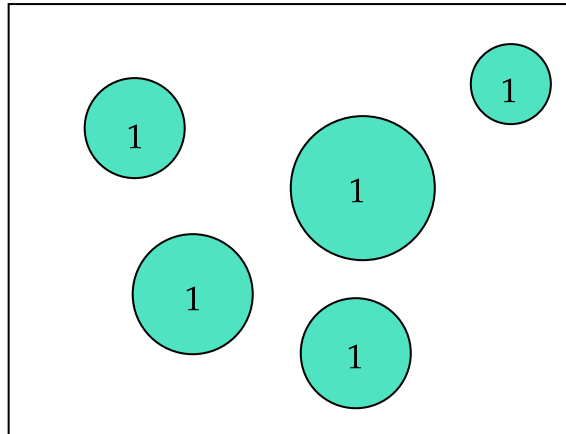


Figure 2.6: Connected regions (i.e. droplets) to which will be assigned unique values.

Initially one should assign some positive value (let us say 1) to the cells corresponding to non-zero f (the cells that we want to evaluate) and zero for the rest of the cells as shown in Figure 2.6. This scalar field is passed to the $tag()$ function initially.

Listing 2.1: $tag()$

```

int tag (scalar t)
{
  /* Initial guess as a Z- (or Morton -) index value */
  long i = 1;
  foreach_leaf()
    t [] = (t [] != 0)*i++;
  boundary (t);
  /* Multigrid iterations */
  multigrid_tag (t);
  /* Sorted array that stores the neighborhood index */
  int * a = neighborhood_indices (t);
  /* Reduction of the range of indices */
  foreach ()
    if (t [] > 0)
      t [] = lookup_tag (a, t []) + 1;
  boundary (t);
  /* Number of connected neighborhoods */
  int n = length_of_array (a);
  free (a);
  return n;
}

```

The first step of the tag function is to assign a guess value to the input tag field. These values are chosen to be the z-index values. Basilisk iterators follow the Z-order for looping, hence using the $foreach()$ iterator and assigning a number increasing by one unit for each traversal will automatically assign z-index values.

After having an initial guess for the tag field, we need to perform multigrid iterations until we assign a unique value to each connected neighborhood. Multigrid

iterations use the grid at multiple levels to evaluate and change the tag field at the finest level. For this, we need restriction and prolongation operators (for trees), which are defined in 2.3.2. In this case, restriction of a cell at level l is simply a minimum over all children (located at level $l+1$) of this cell. Whereas, prolongation of a cell at level l is a direct injection of its parent value located at level $l-1$.

In multigrid iterations for the tag field, for the first iteration, we restrict the initially guessed Z-index values at the finest level ($depth()$ in 2.3.2 denote the finest level) to all of the coarser levels. Where for each cell at the coarser level l we choose the minimum of its children located at the finer level $l+1$.

We then iterate through cells at each level from level 1 until the finest level. As a first step we check the cells with a parent whose tag value is non zero, for these cells we directly inject the parent value. Then in the second step we go to each cell and iterate through a 3×3 stencil as shown by the red grid in Figure 2.12 and assign the minimum tag value of all of these neighbors to this cell.

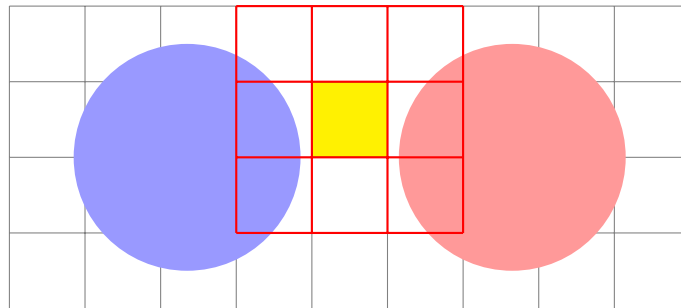


Figure 2.7: Two drops with different colors. Here each color indicates an unique identity.

This whole process of restriction to all coarser levels, prolongation and iterating through a 3×3 stencil for all finer levels from level 1 is repeated until the convergence of tag values for each connected neighborhood to a unique value. This whole process of multigrid iterations in principle can be summarized as: Go to any cell in the domain, iterate through its immediate neighbors for a non zero field value and assign it to the current cell.

: Function 2

```

void restriction (scalar t)
{
    double min = HUGE;
    foreach_child ()
        if (t [] < min)
            min = t [];
    t [] = min;
}

void prolongation (scalar t)
{
    double val = t [];
    foreach_child ()

```

```

}
    t [] = val;
}

```

For tree grids, we need to take into account the minimum tag value of neighboring fine cells. For this at every coarse cell with resolution boundaries, we will iterate through fine cells which are immediately neighboring resolution boundaries and choose the minimum of these fine cells tag value. This is essential for a coarse cell-centered with a blue point, iterating through all of the fine cells centered with black points neighboring the blue lines which are resolution boundaries as shown in figure 2.8 and choose a minimum of these black point cell values.

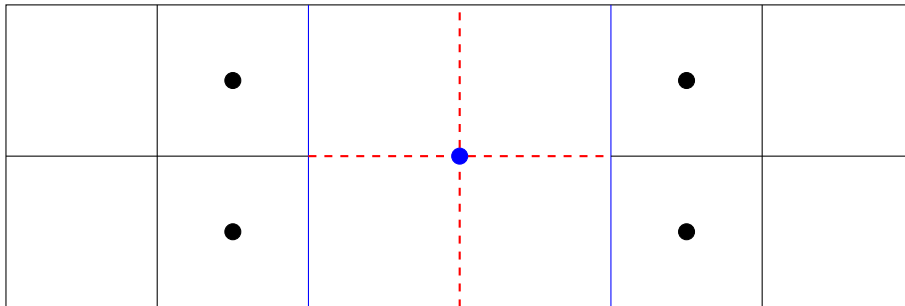


Figure 2.8: Relaxation at resolution boundaries.

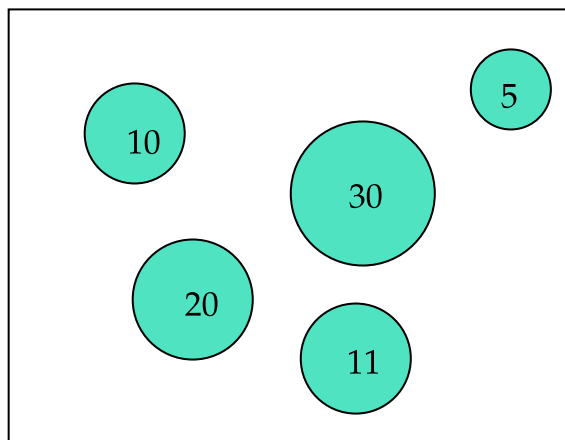


Figure 2.9: Initially drops are assigned unique random numbers. It is then necessary to reduce this range to the maximum number of drops.

After multigrid iterations, we have connected neighborhoods each with a unique index, whose values range anywhere between 1 to the number of leaf cells as shown in 2.9. These values are stored in an array in ascending order by the *neighborhood_indices* function.

: Function 3

```

void multigrid_tag (scalar t)
{
bool changed;

```

```

do {
  /* Restrict tag values to all coarser levels*/
  for (int l = depth () - 1; l <= 0; l --)
    foreach_level (l)
      restriction (t);
  changed = false;
  for (int l = 1; l <= depth (); l++) {
    foreach_level(l)
      /*Prolongation for non-zero parent */
      if (coarse(t) != 0)
        t [] = coarse(t);
        boundary_level(t, l);

    foreach_level (l)
      if (t [] > 0) {
        double min = t [];
        /* Iterating through 3x3 stencil to choose
        the minimum tag value */
        foreach_neighbor(1)
          if (t [] && t [] < min)
            min = t [];
      }
  }
  #if TREE
    foreach_dimension()
      for (int i = -1; i <= 2; i += 3)
        if (is_refined (neighbor((2*i - 1)/3)))
          for (int j = 0; j <= 1; j++)
            if (fine(t,i,j) && fine(t,i,j) < min)
              min = fine(t,i,j);
  #endif
  if (t [] != min) {
    changed = true;
    t [] = min;
  }
}
  boundary_level (t, l);
}
} while (changed);
}

```

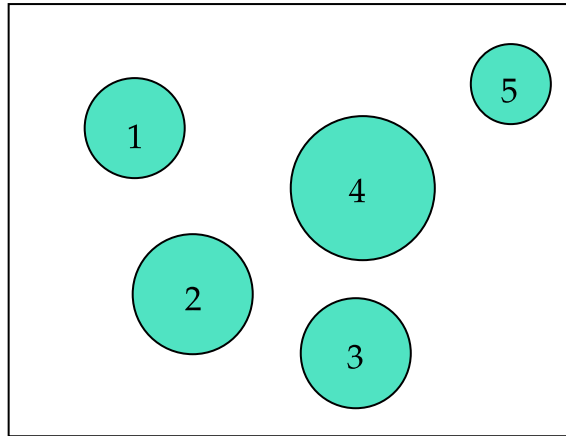



Figure 2.10: Drops with each uniquely assigned numbers, where these numbers range from 1 to the number of drops.

It is more appropriate to have the tag values ranging from 1 to the number of connecting neighborhoods rather than any other higher number. For this, we go to each cell and check its tag value and the corresponding index in the array that stores tag values through a binary search. This task is performed by *lookup_tag* function. The tag values are replaced by its corresponding array index, doing this for all of the cells in the domain will result in tag values ranging from 1 to the number of connecting neighborhoods as shown in Figure 2.10.

2.3.3 Algorithm

The algorithm of the tag function can be summarized as follows:

1. Make an initial guess for the tag field, which is the Z-index value for each leaf cell.
2. Multigrid iterations as mentioned in the following bullet points are performed until convergence of connected neighborhood values is reached.
 - Restrict the tag field from finer to all coarser levels (using the minimum value of children).
 - Prolongate from level 1 until the finest level (using the parent value if it is non-zero).
 - While prolongation through each level l , iterate through all cells of that level, where for each cell we iterate over the 3×3 stencil and assign the minimum non-zero value of all the cells in this 3×3 stencil.
3. Create a sorted array that stores the converged values of each connected neighborhood.
4. Reduce the range of indices in the sorted array.

2.3.4 Some limitations of the tag function

The tag function will not be able to detect multiple droplets whose approaching interfaces exist in a configuration as shown in figure 2.11. This is due to the fact that we iterate through a 3×3 stencil to assign a unique value to each connected neighborhood. In figure 2.11 and figure 2.12 the blue and red color filled inside the droplets represent the tag number. For the purpose of demonstration, let us say that the yellow-filled cell is the one at which we perform operations on a tag value through the red-colored 3×3 stencil. In figure 2.11 we iterate through a 3×3 stencil around the yellow cell checking for the non-zero tag values to assign. We assign the tag number corresponding to the neighboring droplet. This will create the same tag values for the two droplets, when separated by only one cell boundary. Instead, if we have two cell boundaries or one entire cell between two droplets, we will have different tag values assigned to two droplets as shown in figure 2.12.

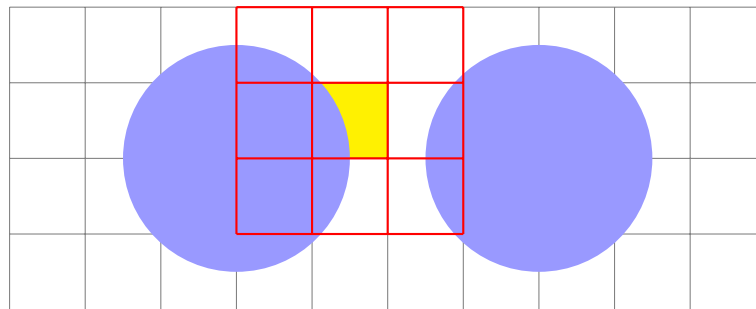


Figure 2.11: Droplets with the same tag value. Here the color of each droplet corresponds to different tag values. We can see the same tag value for two different droplets represented by the same blue color for two droplets.

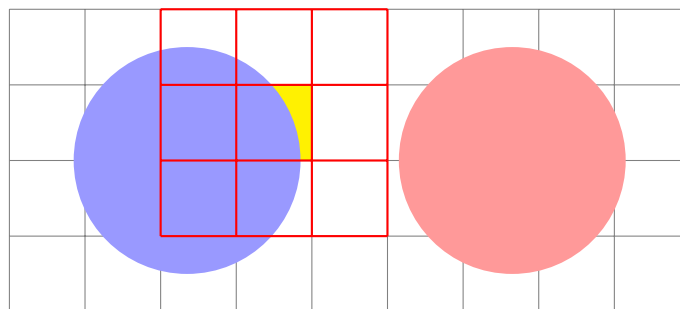


Figure 2.12: Droplets with different tag values.

2.4 Avoiding coalescence using VOF

2.4.1 Introduction

When two interfaces defined by the same VOF tracer are close enough (one cell distance), they automatically merge. This is one of the strengths and weaknesses of the VOF method. In some cases, it may be desirable to avoid coalescence entirely,

for example in the case of foams, emulsions, droplet clouds, etc. To avoid coalescence using a single VOF tracer while solving the Navier-Stokes equations alone without any subgrid model, we need to refine the mesh to an arbitrary level. Even in the case of using a subgrid model, a mesh refinement down to extremely small length scales may be required. This makes the problem computationally challenging for two droplets and impossible for an emulsion with multiple droplets.

A simple way to overcome this problem is to use different VOF tracers for each droplet, which completely prevents coalescence. Coyagee et al. [41] were amongst the first to introduce this method, for a CLSVOF technique. When one wants to simulate more than a few droplets, this technique will become very expensive (both in CPU and memory). Kwakkel et al. [42] proposed an improvement of their multiple marker function method in terms of storage and parallelisation. Rajkotwala et al. [43] used a Local Front Reconnection Method (LFRM) and avoided coalescence by using separate data structures to store each drops marker information.

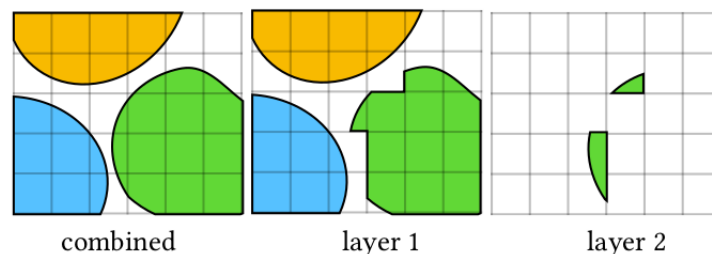


Figure 2.13: Color functions at multiple layers. Overlapping fields can be represented by combination of this fields. Each cell has a maximum of one interface. Reproduced from [44].

A very recent technique to avoid coalescence was proposed by Karanakov et al. [44] using a VOF method. Here the number of marker functions used to represent the drops are independent from the number of drops. They use a different color for different drops and store them in discrete fields and another field to store the corresponding volume fractions. These pairs of fields are called layers. Combination of these layers can store multiple interfaces in the same cell as shown in [44], thus avoiding coalescence.

The idea of avoiding coalescence by using different VOF tracers can be improved by noting that it would be sufficient to use different VOF tracers only for droplets which are “too close” to one another. Determining the minimum number of VOF tracers required, for a given arrangement of droplets, is a variant of the graph coloring problem.

Graph coloring problems

In the field of mathematics, a collection of objects connected by links is known as a graph. The objects are the *vertices* of the graph and the links its *edges*.

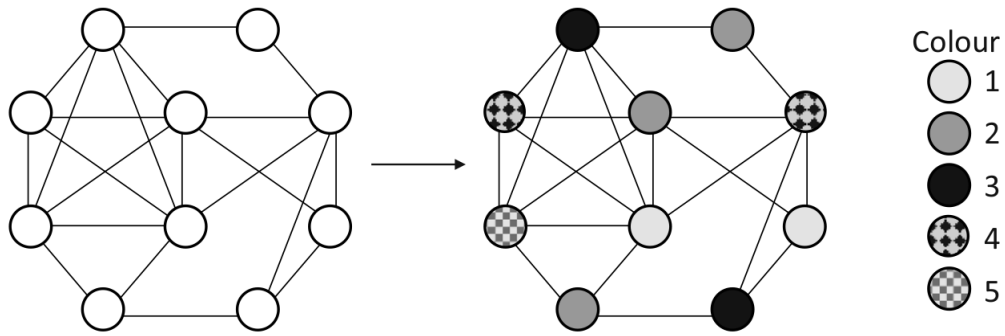


Figure 2.14: A graph and its proper colouring where the vertices are colored with the minimum number of colors so that any two vertices connected by an edge do not have the same color. Reproduced from [45].

The graph colouring problem is to assign colors to its vertices in such a way that no connected vertices have the same colour and using a minimum number of different colors. A sample graph along with its optimal coloring is represented in Figure 2.14.

Np-complete

Graph coloring problems are a group of problems known as Np-complete. These problems have a complexity (i.e. a computational cost) which grows with the number of unknowns N following a function which is non-polynomial (typically exponential). For these class of problems it is thus very difficult to find an optimal solution.

Planar graphs

Planar graphs refers to the family of graphs where the edges do not cross each other. Figure 2.15 shows some types of planar graphs. Closed packing of circles can be represented as a planar graph as shown in Figure 2.16. These types of graphs are relatively easy to colour optimally.

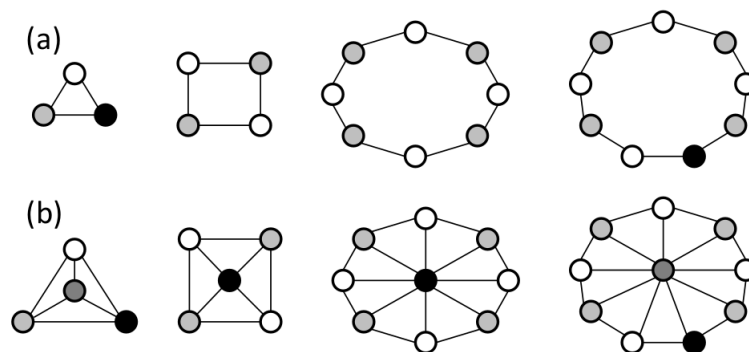


Figure 2.15: Different types of planar graphs Reproduced from [45].

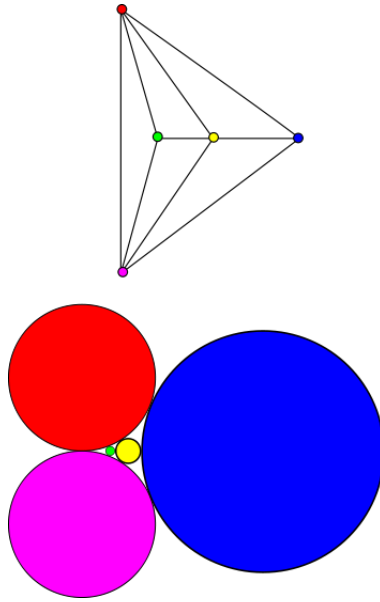


Figure 2.16: A planar graph representing packed circles. Reproduced from [46].

Four-color theorem

The problem of coloring the regions in a map so that no adjacent regions across the boundary shares the same color is a planar graph problem. The four-color theorem states that four colors are sufficient to achieve this optimal coloring for any map. This is shown in Figure 2.17, where different regions of the USA are colored in such a way that no adjacent regions across the boundary shares same color.

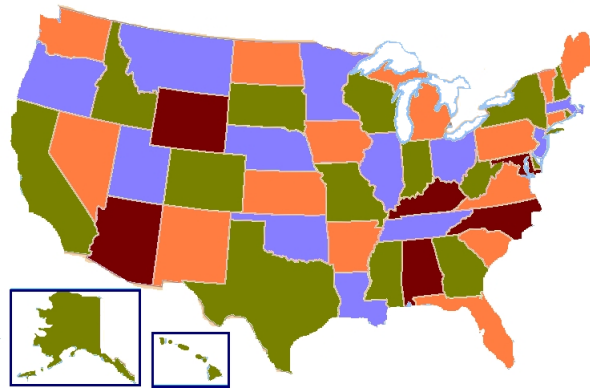


Figure 2.17: USA map coloring all of its states so that no adjacent states at each boundary have same color. Reproduced from [47].

Nevertheless due to being an Np-complete problem, it is very difficult to find this optimal coloring. The important point here is that one can expect that even a non-optimal number of VOF tracers will be much smaller than the number of droplets. For example, figure 2.18 shows red and blue colored droplets. Where different colors represent different VOF tracers. For these sets of droplets arrangement, two VOF tracers are sufficient to avoid coalescence.

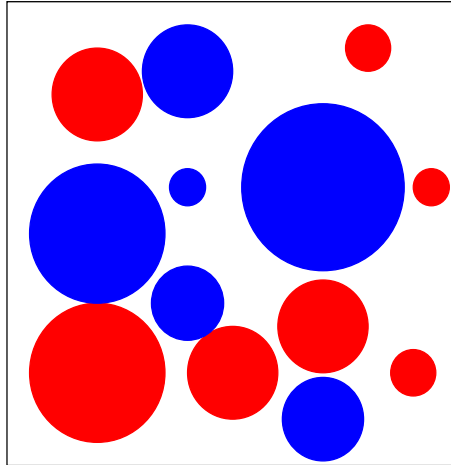
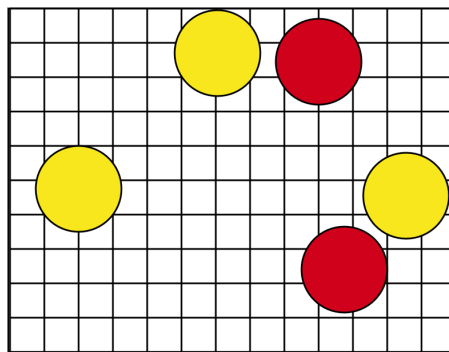


Figure 2.18: Non coalescing droplets.

Time-varying graph coloring problem

In case of maps the optimal coloring is applied to a constant graph. In our case droplets may move around over time changing the graph (pairs of vertices and edges) over time. Our problem is thus a time-varying graph coloring problem where the optimal coloring must be recomputed at each time step.

2.4.2 Principle



$f1 = \text{Yellow color}$

$f2 = \text{Red color}$

Figure 2.19: The drops associated to two different VOF tracers ($f1$ and $f2$).

The idea behind the non-coalescence algorithm is to use as small a number of VOF tracers as possible to color the drops. To achieve this, at first the closely associated drops are listed in a data structure with the help of the tag function (unique identity of the drops) 2.3. Let us take the setup described in Figure 2.19, where five drops are associated to the two VOF tracers ($f1$ and $f2$). The whole process of the non-coalescence algorithm is performed for drops associated to each VOF tracer in a loop. In Figure 2.19 the yellow drops will be processed.

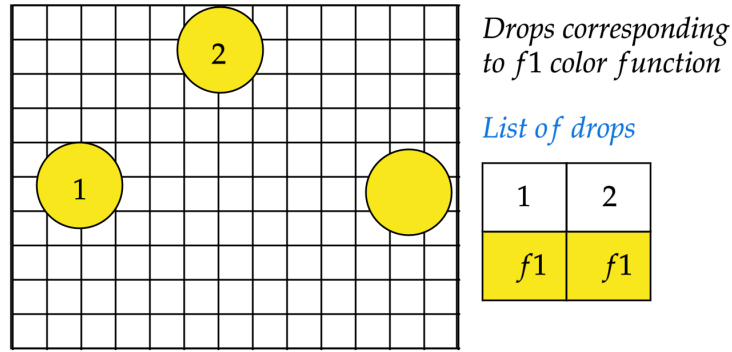


Figure 2.20: Listing the drops that are two cell (or less) distance away from each other. The numbers on the drops represents their unique identity (tag values).

In Figure 2.20 the closely located yellow pairs of drops are listed along with their VOF tracers. We define the drops that are two-cells distance away (or less) as a closely located pair (this criteria helps to overcome the limitations of the tag function). This is achieved through a 5×5 stencil iteration centred at a continuous phase cell to detect if there are any interfaces with the same VOF tracers but a different tag number.

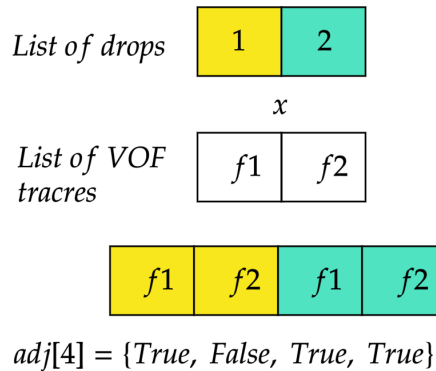


Figure 2.21: An array storing the closely located drops neighboring tracers information.

An array is created which stores the information of the neighboring VOF tracers of each drop in the closely located pairs list (List of drops in Figure 2.20) as shown in Figure 2.21. For each pair in the list, the drop surrounded by the least number of neighboring VOF tracers is chosen (this allows us to reduce the total number of VOF tracers), this is drop number 1 in Figure 2.20. Thanks to the array that stores the information of the neighboring VOF tracers, we can find the VOF tracer (different from that of the drop) in the list that is not neighboring this drop 1. In Figure 2.21 the second element in the array adj is false. This means that drop 1 does not have any neighboring drops associated to VOF tracer $f2$.

If we do not find any, a new VOF tracer will be created. This process is repeated for all of the pairs in the list (In the illustrating example we have only one pair.) This non-neighboring VOF tracer or a new VOF tracer is listed corresponding to each drop as presented by the table in Figure 2.22.

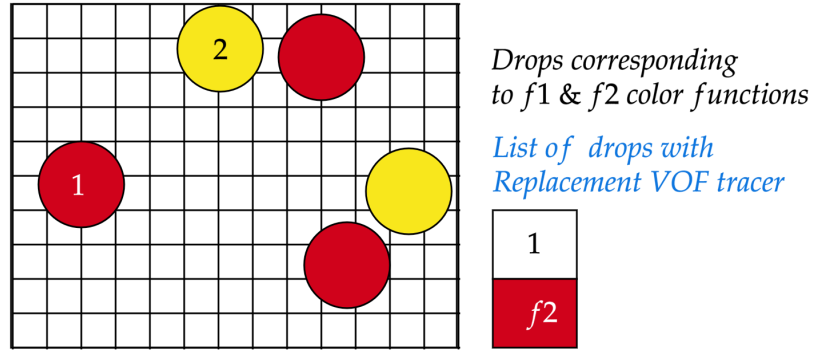


Figure 2.22: Replacing the VOF tracer (f_1) of drop 1 with the other tracer (f_2) corresponding to a non neighboring drop.

The replacement VOF tracers in the list are associated to their corresponding drops as shown in Figure 2.22.

2.4.3 Summary of algorithm and implementation

The *no_coalescence()* function is developed to use a small set of VOF tracers for a large number of droplets, where the droplets which are very close will be advected by different VOF tracers. This will completely avoid coalescence for all of the droplets. The *no_coalescence()* function is summarized as follows:

1. Find the VOF tracers corresponding to droplets, whose interfaces are separated by two cells and store them in a list *maybe_close*.
2. For each VOF tracer in the list *maybe_close*:
 - (a) Find the corresponding droplet pairs which are one to two cell distance away and add them to an array *too_close*.
 - (b) Find which VOF tracers are surrounding each droplet in an array *too_close* and add that information in an array *adjoin*.
 - (c) Iterate through each pair of droplets in an array *too_close*. Find which droplet in each pair have the smallest number of different neighboring VOF tracers using *adjoin* array and replace the other droplet in the pair with this droplet number.
 - (d) Find the replacement VOF tracer for each droplet number in an updated array *too_close* and add them to an array *replace*:
 - i. For the first droplet replacement, create a new VOF tracer and add it to the *interfaces* and remove the existing single VOF tracer $f[i]$.
 - ii. Otherwise, using *adjoin* array, find non-neighboring different VOF tracer for each replacement droplet in updated *too_close* and add it to the corresponding element in *replace*.
 - iii. If there are no non-neighboring different VOF tracer for replacement, create a new VOF tracer and add it to the list of *interfaces*.
 - (e) Go through each droplet number in updated *too_close* and corresponding replacement VOF tracer in *replace* to replace the VOF tracers and update the list of *interfaces*.

3. Field at each cell

$$f[\] = \sum_{i=0}^{i=n} f_i[\]$$

is updated, where f_0, f_1, f_2 , etc. are different VOF tracers in *interfaces* list.

2.5 Controlled coalescence

The real emulsions lie between the two limiting cases: Numerically coalescing and non-coalescing emulsions. Existing solutions to achieve this intermediate stage are of two types: one way is to couple an additional model to a single VOF advection [48], the other way is to use multiple marker functions (multiple VOF tracers) coupled with an additional model (tested only for binary coalescence) [49]. In the first case (single VOF), an additional subgrid model decides the thickness of the film. This may require a very fine mesh. While in the other case as many VOF tracers as drops are needed. These two solutions are thus very computationally expensive for large emulsions.

An extension of the non-coalescence algorithms is proposed, which allows to control the duration during which droplets can interact before coalescing. This opens the door to controlling the coalescence timescale through additional subgrid-scale modelling.

2.5.1 Principle

In a non-coalescing emulsion as shown in Figure 2.23, if we can track each pair of interacting drops over time and count the amount of time they are in contact. We can then use a model of coalescence/drainage time and allow them to coalesce only when this drainage time is reached.

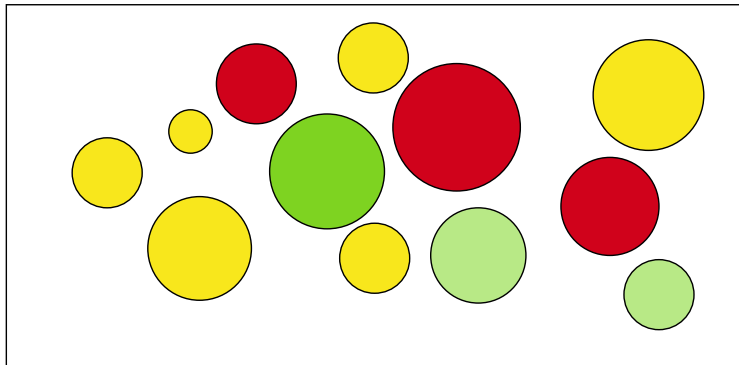


Figure 2.23: Drops colored differently such that no two interacting drops have the same color. These are essentially non-coalescing drops.

We use the tag function 2.3 to identify each pair of non-coalescing drops (drops with multiple VOF tracers) uniquely at each instance of the simulation. The same pair can have different identity values at different instances. A pair of drops are tracked over time by tracking their centroids. Usually the stability conditions while

solving the Navier-Stokes equations along with the surface tension ensures that the motion of the flow does not travel more than two computational cells. Therefore the same pair of drops can be tracked over time by computing the differences in their centroids. For instance if there exists \mathbf{X}_t at t and \mathbf{X}_{t-dt} at $t - dt$, such that $|\mathbf{X}_t - \mathbf{X}_{t-dt}| < 2 * \Delta$, where Δ is the computational cell size. Using this process pairs of drops are tracked over time and then allowed to coalesce (based on an input time or time computed by a coupled model) by merging their VOF tracers.

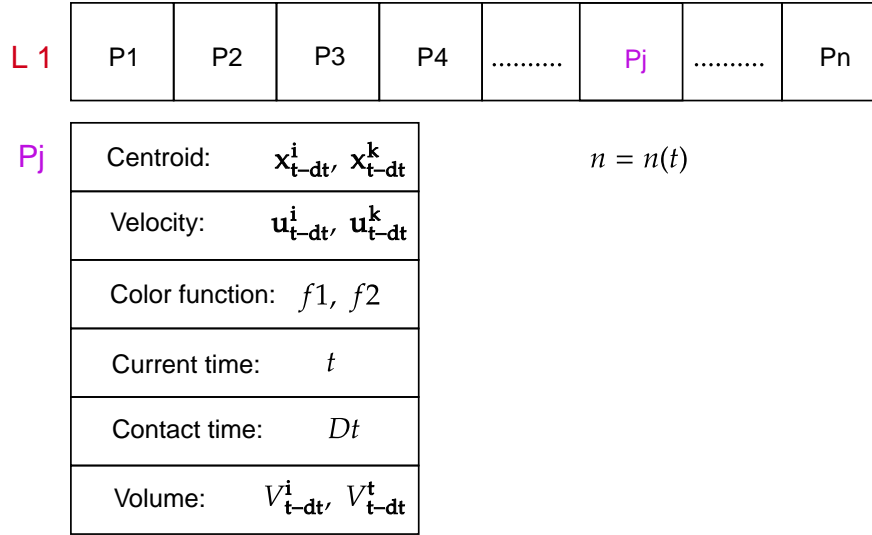


Figure 2.24: Data structure representation that stores the information of pairs of drops being tracked.

A data structure, let's say List 1, is maintained from the beginning till the end of the simulation. The details of the pairs of drops being tracked such as their centroid, velocity, current time, contact time and color functions (VOF tracers) is stored in this list. The representation of this data structure is shown in Figure 2.24, where the P1, P2 etc. corresponds to the pairs of drops. Each j^{th} element in the List 1 stores information of the pair of drops (i^{th} and k^{th}) such as centroid, centroids velocity, volume, color function, current time of the simulation and contact time (amount of the time the drops are in contact). Here the number of elements in $L1$ may vary at each instance of the simulation.

There are four stages in the *control coalescence()*:

- Detecting the closely located pairs of drops
- Tracking these pairs over time and update their information
- Listing the pairs whose contact time $>$ prescribed time
- Merging the pairs whose contact time $>$ prescribed time

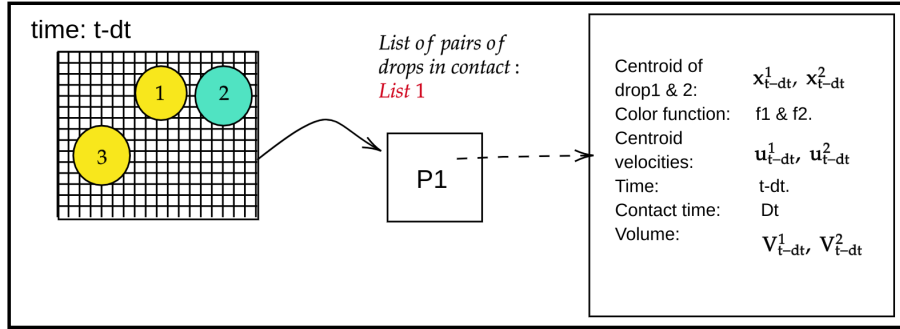


Figure 2.25: The drops and control coalescence data structure List 1 with one pair P1 at time $t - dt$.

Before passing through these stages, the non-coalescence function is passed. In Figure 2.25, the three drops at time $t - dt$ after passing through the control coalescence function is shown. The numbers written on drops corresponds to their unique identifier at each time instance. Whereas the different colors represents color functions. At this time $t - dt$ there is only one pair (Drop 1 and 2) in the list and corresponding drops are between one to two cell distances away from each other. After advection of the interfaces, the non-coalescing function is passed and any new closer drops are assigned different VOF tracers as shown in Figure 2.26. Now the control coalescence function is passed and the drops undergo the different four stages of that function:

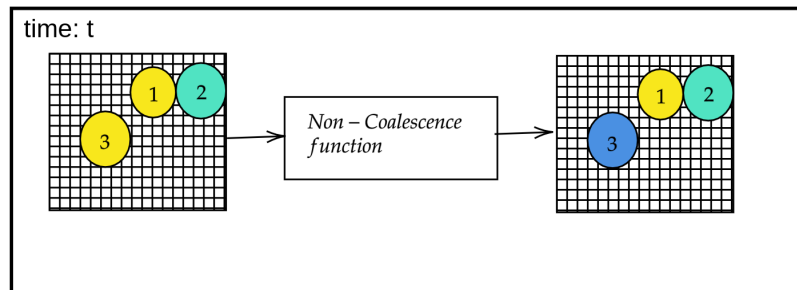


Figure 2.26: The non-coalescence function is passed at time t after interface advection changing the color function of the closely located drops.

Detection of the pair of drops in contact

In this stage, at first the color functions (VOF tracers) corresponding to the closer drops (less than two cell distance away) are found. We do this to reduce the computational cost of the process of uniquely identifying the drops (the tag function is computationally expensive, as it scales as the Poisson solver). To achieve this, we go through each interface cell corresponding to some VOF tracer and iterate through a 3×3 stencil with respect to this cell to check if there are any other non-zero VOF tracers in this stencil? if yes, this will be added to the list of VOF tracers corresponding to close drops. This detection can be illustrated from figure 2.27, the yellow-filled cell represents the cell at which we are conducting checks to detect

neighboring VOF tracers. The red-colored grid corresponds to a 3×3 stencil in which we check if there is any other interface. Here we find two drops in the grid with different colors, we will add these two VOF tracers to the list. In this case, we find a green interface corresponding to f_2 in 3×3 stencil. Hence this f_1 and f_2 will be added in the list. We repeat this for all pairs and store the VOF tracers information in a data structure (lets say list of tracers).

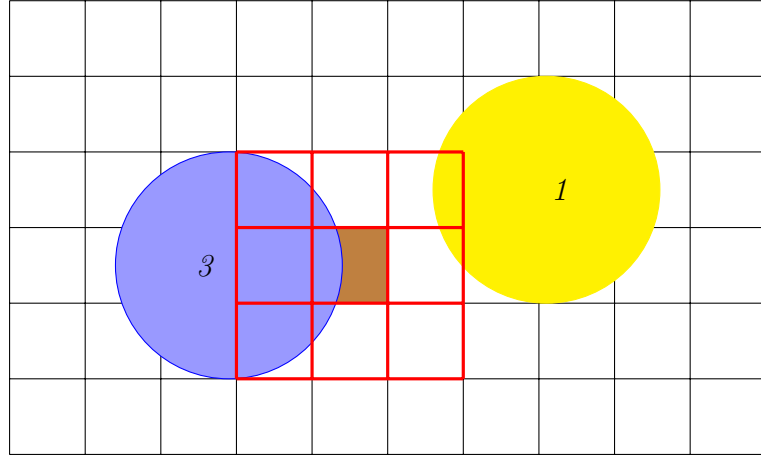


Figure 2.27: Droplets with different VOF tracers represented by different colors.

Each pair of drops (less than two-cell distance away and having different VOF tracer) associated to the VOF tracers in the list of tracers are uniquely identified using the tag function. For each of this pair.

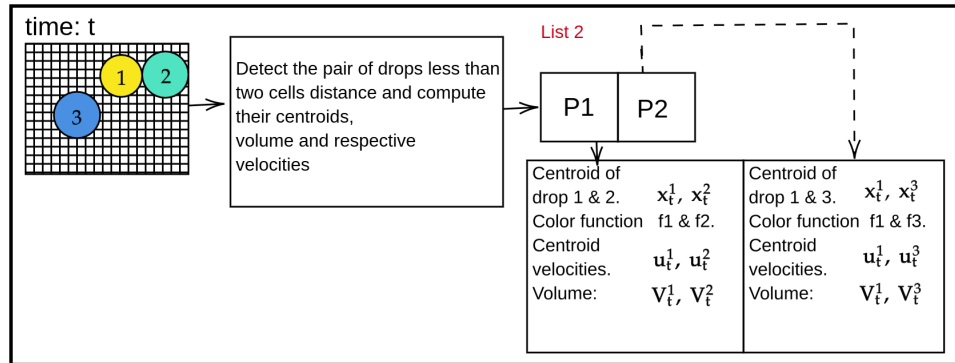


Figure 2.28: Listing the information of the pairs of drops that are in close contact at time t .

A new data structure, lets say List 2, stores the information of each uniquely identified pairs of drops along with their information such as centroid, color functions, velocity and volume.

$$\text{Centroid of the } j^{\text{th}} \text{ droplet} = \mathbf{X}^j = \frac{\sum_j \mathbf{x} f_i \Delta^2}{\sum_j f_i \Delta^2} \quad (2.23)$$

$$\text{Velocity of the } j^{\text{th}} \text{ droplet} = \mathbf{u}^j = \frac{\sum_j \mathbf{u} f_i \Delta^2}{\sum_j f_i \Delta^2} \quad (2.24)$$

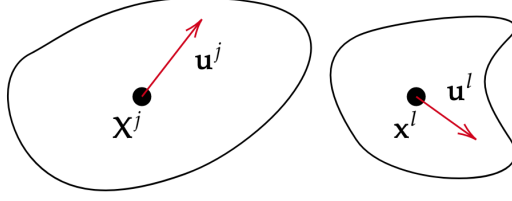


Figure 2.29: The centroid and the velocity of a pair of drops.

where f_i is the color function of the j^{th} droplet evaluated at each point inside this droplet at \mathbf{x} and \sum_j is summation in the computational cells of the j^{th} droplet. Here Figure 2.29 shows two drops with their centroid and velocities, which can be obtained by 2.23 and 2.24. This process can be observed from a schematic 2.28. Here at time t there are two pairs of drops (named P1 and P2 in List 2) that are less than two cell distance away and each pair associated to the different VOF tracers. The information of these two pairs is stored in List 2.

Tracking of the drop pairs over time

The unique identity of the same drop pair is different at the different instances. The stability conditions of the discretized governing equations ensures that the drops travel less than two cell distances. We check which pairs in List 2 already exist in List 1 by matching the centroids as follows:

$$\begin{aligned}
 & \text{for}(k = 0; k < \text{length}(\text{List 1}); k++) \\
 & \text{if} ((\mathbf{x}_t^j - \mathbf{x}_{t-dt}^i) \leq \mathbf{u}_{t-dt}^i * dt \parallel (\mathbf{x}_t^j - \mathbf{x}_{t-dt}^k) \leq \mathbf{u}_{t-dt}^k * dt) \\
 & \quad \text{update } i^{th} \text{ or } k^{th} \text{ drop element in List 1 with} \\
 & \quad \quad j^{th} \text{ drop element in List 2}
 \end{aligned}$$

\mathbf{x}_t^j : Centroid of the smallest drop corresponding to some element in the List 2 at t . $\mathbf{x}_{t-dt}^i, \mathbf{x}_{t-dt}^k$: Centroid of drops corresponding to some element in the List 1 at $t - dt$. $\mathbf{u}_{t-dt}^i, \mathbf{u}_{t-dt}^k$: Velocity of the centroid of drops corresponding to the $x_{t-dt}^i, \mathbf{x}_{t-dt}^k$.

If we find any pair in the List 2 that matches the pair in the List 1, this pair is updated in List 1 with the List 2 information. This process can be observed from the Figure 2.30, where P1 information is updated in the List 1. In Figure 2.31 a pair of drops over consecutive time instances are shown. If there are any unmatching pairs in List 2, these are added as the new pairs with all of their information in List 1. In Figure 2.30, the P2 is added as the new element in List 1.

The reason for choosing the smallest drops in each pair to compare is that at the previous time step there can be a mutual pairs lets say (1, 3) and (1, 2). Let us suppose that the drops 1 and 3 got coalesced then there will be a new pair 2 and 4, where 4 is a new drop made up of 1 and 3. But the film drainage continues between 2 and the part of the newly formed drop. To continue counting the drainage between this new pair this is useful, nevertheless further tests and improvements are envisaged.

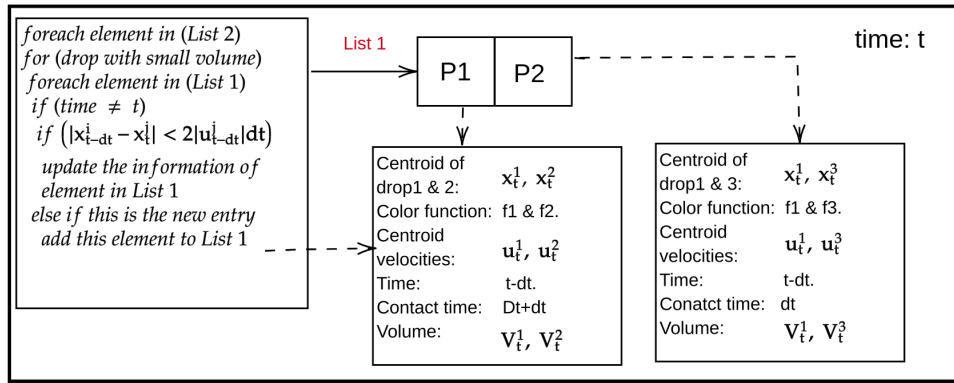


Figure 2.30: Matching the drops in List 1 at $t-dt$ to the List 2 at t . Information of drops in List 1 is update when matched to List 2. Unmatched elements in List 2 are added as new elements in List 1.

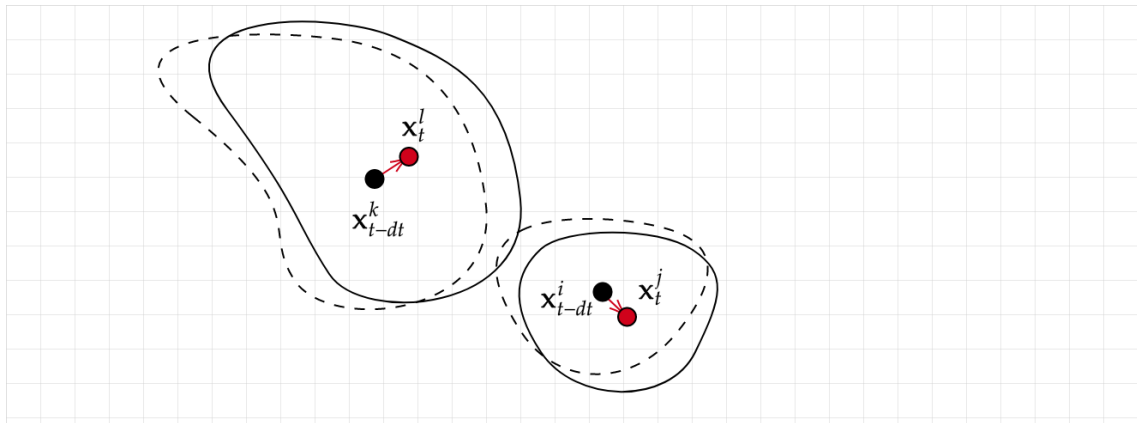


Figure 2.31: Detecting the pair of drops over time via motion of centroid. The dotted lined interface corresponds to the time $t-dt$ and continuous lined interface to the t .

Checking the contact time

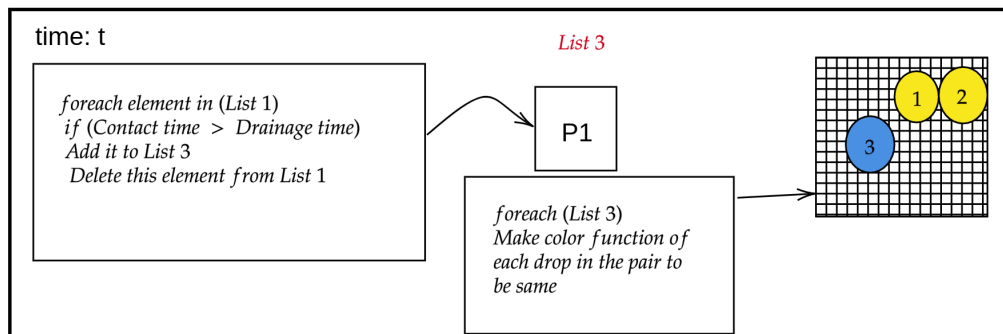


Figure 2.32: The contact time of the pairs of drops in List 1 is compared to the Drainage time (an input parameter suggesting coalescence). The pairs that meets the criteria are listed and allowed to coalesce.

Now we have a list of pairs of drops with their centroid and the drainage time along with the other information. We iterate through each pair of drops information in the List 1 and check if the contact time is greater than the prescribed drainage time. If yes, then we will add it to a data structure List 3. List 1 with the rest of the pairs is passed to the next time step to continue the process of tracking.

Merging of the VOF tracers

All of the elements in List 3 are supposed to be coalesced, hence each pair of VOF tracers are merged. In Figure 2.32 the contact time checking and the merging process are summarized.

All of these stages are summarized in Figure 2.33.

2.5.2 Summary of the algorithm

At each time step

1. Call the no-coalescence function, which will assign different VOF tracers to each drop of the approaching pair of drops.
2. Pass the list of pairs of drops not coalesced from the previous time step, let us say `coalescence_pair` (List 1). If it is the first time step, pass an empty list through the `control-coalescence()` function.
3. Find the VOF tracers corresponding to the drops that are less than two grid cell distance away and store in a list called `maybe_close`.
4. Tag the drops corresponding to VOF tracers in the list `maybe_close`.
5. List the pairs of drops in contact with each other (less than two grid cells distance) in, let us say `drop_pair` list (List 2), along with information such as their VOF tracers, centroid, volume, current time, and centroids velocity.
6. For each drops pair in the `drop_pair` list (List 2), choose the centroid of the smallest drop.
 - (a) Check if the absolute distance between this centroid and each drop centroid amongst all pairs in the `coalescence_pair` (List 1) list is less than or equal to that corresponding velocity multiplied by the time interval.
 - (b) If this is true, then update the corresponding drop pair information in the `coalescence_list` (List 1) with the one from the `drop_pair` (List 2) list and increase the contact time information.
 - (c) If not, add it as a new element in the `coalescence_list` (List 1).
7. Iterate through each pair of drops in the `coalescence_list` (List 1) and check which pair has exceeded the prescribed contact time. Save all the pairs that have exceeded the prescribed contact time in a new list, let us say `merge_list` (List 3). Remove the elements corresponding to the `merge_list` (List 3) from the `coalescence_list` (List 1).

8. Iterate through each drop pair in `coalescence_list` (List 3) and assign the same VOF tracer to both of the drops.
9. Delete all of the lists except `coalescence_pair` list (List 1), which will be passed through the `control-coalescence` function in the next time step.

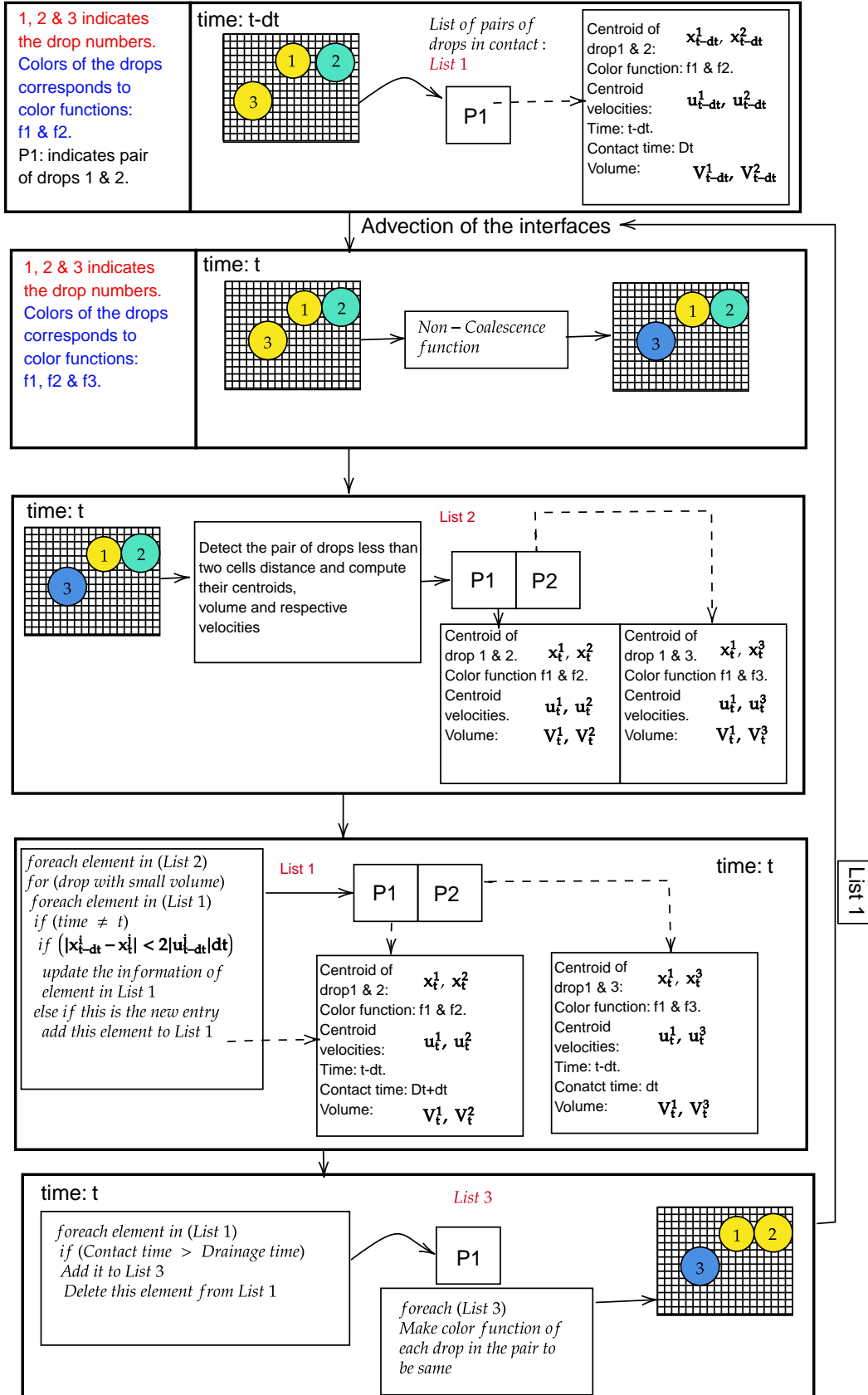


Figure 2.33: Control coalescence algorithm.

Chapter 3

Results and analysis

In this chapter two limiting cases of emulsions: numerically-coalescing and non-coalescing and an intermediate case: controlled-coalescing, emulsions are simulated. The non-coalescence and controlled-coalescence emulsions are demonstrated by using the new functions developed. All these cases are analyzed qualitatively and quantitatively. The analysis of the effect of the numerical resolution and the domain size on numerically-coalescing and non-coalescing emulsions is described. The effect of the control parameter on the controlled coalescing emulsion is demonstrated by measuring the total settling time and coalescence frequency. Finally, all three different cases are compared in terms of the phase front evolution.

3.1 Simulation setup

The simulation setup that we describe here is applicable to all the cases we present in this chapter. The main varying parameters will be the number of drops and the size of the domain.

Though the simulation setup is 2D, and so does not exactly represent real systems, it offers a good insight on various processes. It is easier to analyze and computationally cheaper and allows to simulate a larger number of drops which make statistical analysis feasible. The 2D emulsions are not explored much. For all these reasons simulations are performed in 2 dimensions.

The simulation setup is a L square domain as shown in Figure 3.1 where a mono-dispersed distribution of drops of diameter D with density ρ_d and viscosity μ_d is suspended in another liquid of density ρ_c and viscosity μ_c . The surface tension coefficient is σ . The minimum distance between the bottom boundary of the domain and the interface of the bottom layer of drops is denoted as H_i . The left and right boundaries are periodic. No-slip and no-penetration boundary conditions are imposed at the top and bottom of the domain. At the bottom boundary a non-wetting boundary condition is imposed. This helps to reduce the computational cost by avoiding the need to resolve thin films at the bottom boundary.

This emulsion is modelled using the incompressible Navier-Stokes equations with variable density and viscosity along with the surface tension and gravitational force as an additional source terms. The numerical resolution of the Navier-Stokes equations and interface advection is summarized in chapter 2.

In all the cases, the drops are initialized at rest at a constant H_i above the bottom wall. The gravity is imposed in the vertical direction as shown in Figure

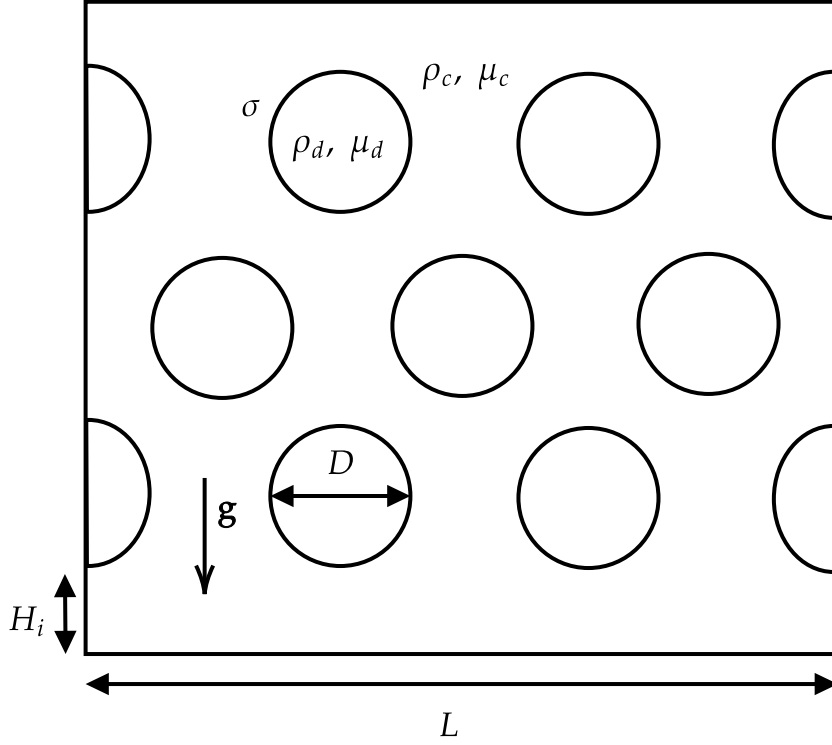


Figure 3.1: An L 2D square domain consisting of two phases, where drops are distributed in an hexagonal packing with a slight perturbation.

3.1. The drops are arranged as an hexagonal packing with a random perturbation of their locations in the range of 0 to $5\%(D)$. The distance between the centres of neighboring drops is assigned as $0.3 + D \pm (0 \text{ to } 5\%(D))$. The bottom most layer of drops are not perturbed, whereas the drops at periodic boundaries are perturbed only in the y direction.

Governing parameters

In our system there are nine dimensional parameters: $\rho_d, \rho_c, D, L, g, \sigma, \mu_d, \mu_c$ and ϕ , the volume fraction of drops. According to the Buckingham-Pi Theorem, 6 independent dimensionless parameters are sufficient to completely describe our system. The system incorporates two geometric length scales, the drop diameter D and the size of the domain L , whose ratio is a dimensionless number L/D . The system incorporates the physical phenomena driven by buoyancy, surface tension and viscous diffusion. Hence the Bond number Bo and the Archimedes number Ar can be added as governing dimensionless numbers. The density ratio ρ_r , viscosity ratio μ_r and number of drops n are chosen as the last 3 dimensionless numbers. Accordingly the characteristic velocity of the system is $U = \sqrt{l_c g}$ and the characteristic time scale of the system is $t_c = \sqrt{\frac{l_c}{g}}$, where l_c is the characteristic length scale of the system and g is the acceleration of gravity. Unless otherwise specified, t refers to

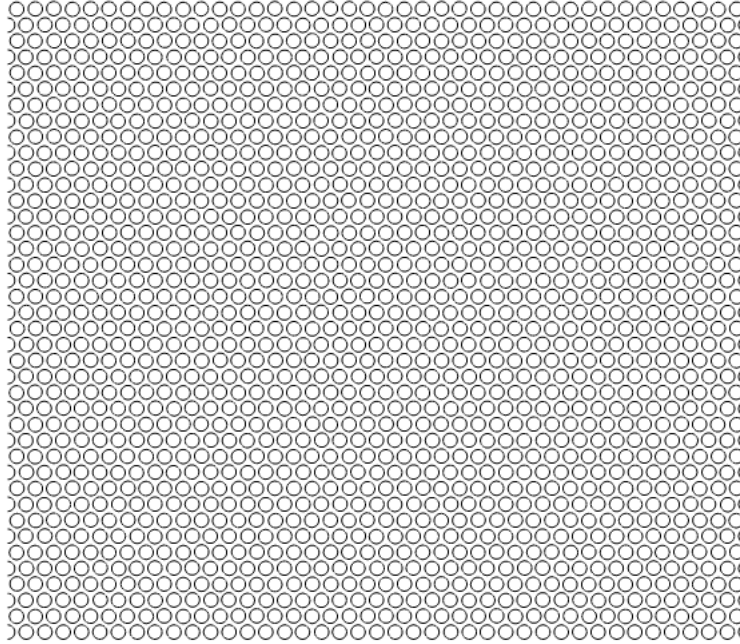


Figure 3.2: $\frac{L}{D} = 52$ initialized with the same parameters (except the number of drops) as described in Figure 3.1.

the dimensionless time scaled with $t_c = \sqrt{\frac{D}{g}}$ and $U = \sqrt{Dg}$.

When the characteristic size of the drops is less than $O(\mu m)$, corresponding to $Bo < O(10^{-3})$, the explicit resolution of the surface tension term imposes a very restrictive limitation on the timestep, given by:

$$T_\sigma = \sqrt{\frac{\rho_m \Delta^3 \min}{\pi \sigma}} \quad (3.1)$$

At very low Ca & Bo the timesteps of the simulation will be much smaller even for a mesh size corresponding to 20 points per drop. This will hinder the possibility of large scale experiments. When a drop corresponds to $Bo \ll 1$, it is non-deformable as its diameter is smaller than the capillary length scale. But the speed of film drainage still depends on the Bond number, the smaller the Bo , the faster the film drainage leading to faster and higher probability of coalescence. In our simulations however, the coalescence will be either numerical, completely avoided, or controlled based on a subgrid model (considering that the mesh size is much larger than the critical film thickness, which is usually the case).

High Reynolds flow regime lead to thin boundary layers at the interface, which requires high numerical resolution and thereby small timesteps. Our flow is buoyancy-driven starting at rest, hence we use the Archimedes number as a governing parameter. We will choose this number accordingly to avoid thin boundary layers. Due to all of the reasons stated above, to allow easy experimentation we choose the regimes where drops are slightly deformable and moderate Reynolds/Archimedes numbers. The dimensionless parameters and their corresponding values for all of the emulsion

Dimensionless parameters	Value
$\text{Bo} = \frac{\Delta\rho g D^2}{\sigma}$	2.5
$\text{Ar} = \frac{\rho_c \Delta\rho g D^3}{18\mu_c^2}$	1.388
$\rho_r = \frac{\rho_c}{\rho_d}$	0.8
$\mu_r = \frac{\mu_c}{\mu_d}$	2
$\frac{L}{D}$	156, 104, 52, 13
$\phi = \frac{\pi D^2 n}{L^2 4}$	0.4647
$n = n(D, L, \phi)$	100, 1600, 6400, 14400

Table 3.1: Simulation parameters.

simulations performed are chosen as indicated in Table 3.1. The numerical resolution of the simulations is represented by the number of points per drop diameter $\frac{D}{P}$ and ranges from 20 – 100 in our simulations.

The volume fraction of the drop phase $\phi = 0.4647$ is same for all of the simulations performed. The other notable parameter $n = n(D, L, \phi)$ is the number of drops present in the simulation, which is a dependent dimensional parameter, whose range is present in Table 3.1.

3.2 Evolution of coalescing emulsions

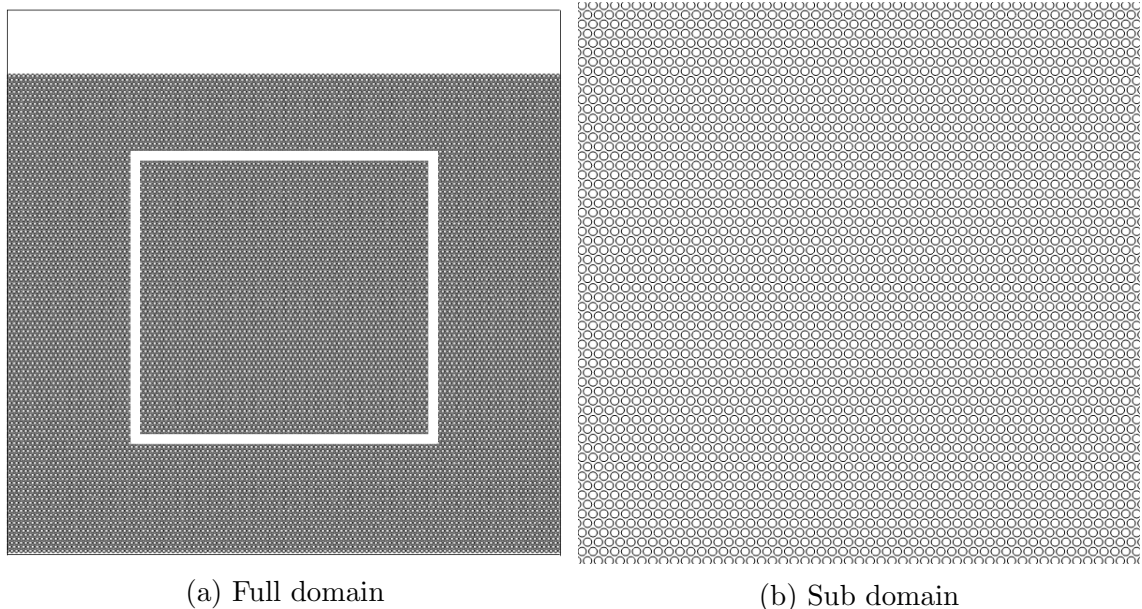


Figure 3.3: A 2D domain with $\frac{L}{D} = 156$ in hexagonal packing as shown in 3.3a. The area corresponding to the white colored box in 3.3a is zoomed by 2.3x and displayed in Figure 3.3b.

In this section the simulation of coalescing emulsions using a single color function for all of the drop phase is demonstrated with qualitative and quantitative analysis

through a test case with the simulation parameters as follows:

Bo	Ar	ρ_r	μ_r	$\frac{L}{D}$	n	$\frac{D}{P}$
2.5	1.388	0.8	2	156	14400	26

Table 3.2: Simulation parameters corresponding to the $\frac{L}{D} = 156$ test case.

The simulation setup is a 2D domain with $\frac{L}{D} = 156$ (14400 drops) in hexagonal packing with a perturbation between 0 to 5%(D) as shown in Figure 3.6. Here the characteristic length scale is $l_c = D$ and the characteristic time scale is $t_c = \sqrt{\frac{D}{g}}$.

This simulation took 150 CPU hours on 144 cores on the IFPEN Ener super-computer to run for $950t_c$ time.

The coalescence in this section 3.2 refers to numerical coalescence, which depends on the mesh size.

Visualization of the drops and the continuous phase y-velocity field images of the simulation output gives qualitative insight about its evolution. Therefore observation of these images and appropriate understanding of its behavior is detailed.

The visibility of drops is hindered in the $\frac{L}{D} = 156$ case due to the presence of a large number of drops. Hence along with the whole domain, different subdomains are zoomed and shown in Figure 3.4, 3.5, 3.6, 3.7 and 3.8.

3.2.1 Qualitative description

The evolution of the emulsion can be divided in the following stages:

- Settling stage: Settling under gravity.
- Intermediate stage: Appearance of vertical channels.
- Coalescence stage: Significant coalescence.
- Filaments stage: Formation of filaments and breakup along with coalescence.
- Separation stage: Separation in two continuous phases.

Settling stage

The droplets initialized at rest in the hexagonal packing arrangement start to settle under the influence of gravity. Initially the droplets settle down smoothly and reach a terminal velocity. This stage is shown in Figure 3.4, where the whole domain is displayed at $t = 40$. The visibility of the drops is hindered due to the presence of a large number of drops.

Therefore we choose a subdomain close to the bottom of the interface, middle of the domain and close to the top phase front as shown in Figure 3.4a represented by three different colored boxes. The region corresponding to this colored boxes is zoomed by 3x and presented with the corresponding color border in Figures 3.4b, 3.4c and 3.4d.

From these figures we can observe that the drops undergo settling similarly in all of the subdomains.

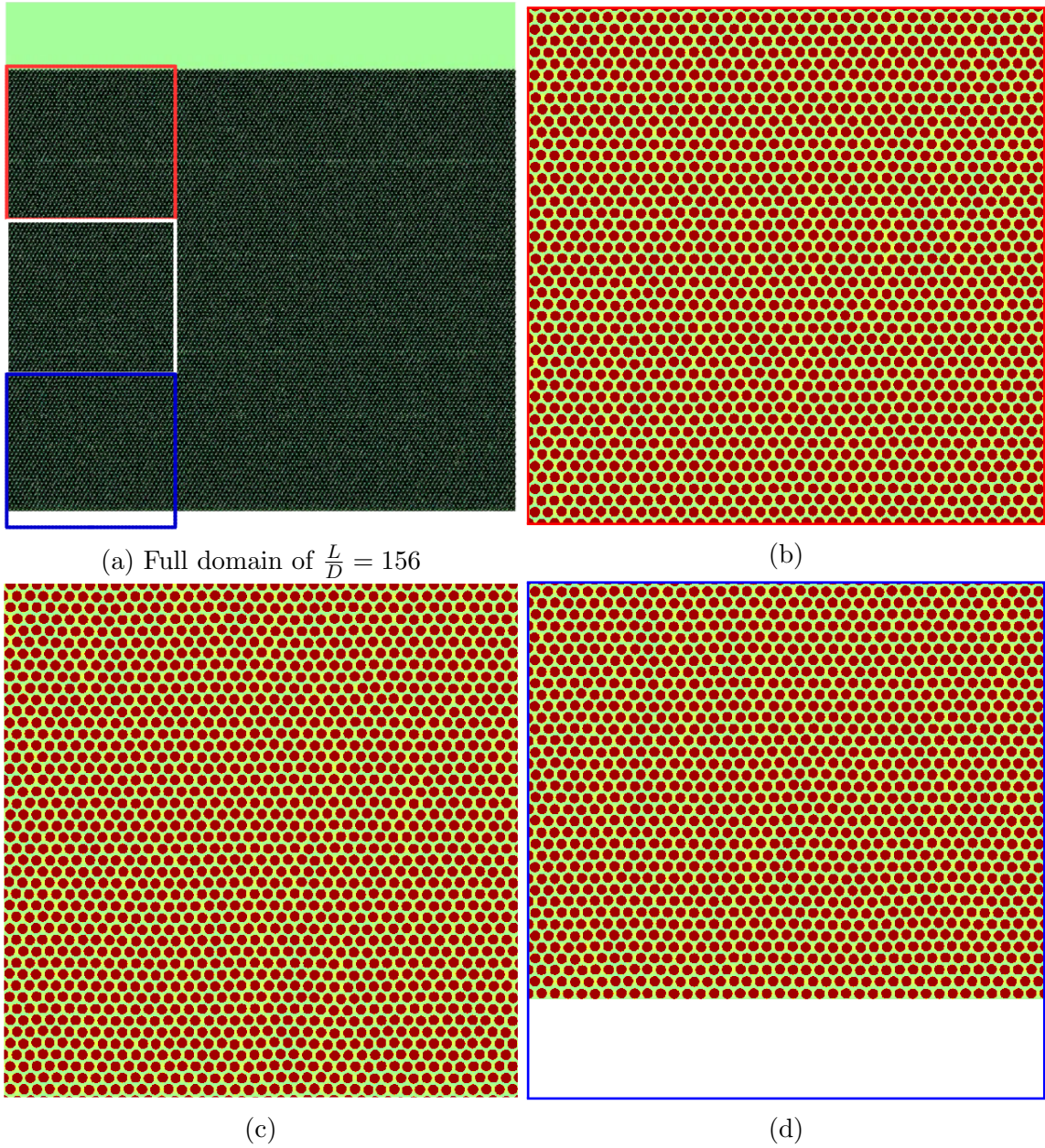


Figure 3.4: A 2D domain with $\frac{L}{D} = 156$ at settling stage corresponding to simulation time $t = 40$. The different subdomains are presented in Figures 3.4b, 3.4c and 3.4d with border colors corresponding to the regions of the same color in the whole domain shown in Figure 3.4a. In subdomains the drops are red and the surrounding phase is colored with the magnitude of the y-velocity ranging from $[-0.1 : 0.1]U$ (blue to red).

Intermediate stage

As drops settle down there appears to be an instability showing alternating vertical channels of the y -velocity field in the flow as shown in Figure 3.5 corresponding to the simulation time $t = 140$. We can observe alternating vertical channels in the 3 subdomains. The maximum wave length corresponding to these alternating vertical channels is between $4D$ to $8D$. In this stage there is no significant coalescence yet in all of the domain; only a few droplets starts to coalesce as shown in Figure 3.5d. The characteristic length scale corresponding to this phase is the droplet diameter D .

Coalescence stage

Here the coalescence frequency increases significantly leading to significant changes in the drop distribution as shown in Figure 3.6, which corresponds to simulation time $t = 200$. The zoomed colored box regions corresponding to Figure 3.6a are displayed in Figures 3.6b, 3.6c and 3.6d. The alternating vertical channels which appeared in the intermediate stage disappear as coalescence frequency increases.

It is important to note that the coalescence is numerical and controlled by the mesh size. Finer meshes might delay these transitions between different stages. The other length scale, given by the domain size, starts to play a role, giving rise to a transition from one scale to another. We can also observe that the coalescence frequency is higher close to the bottom boundary and starts to decrease a little as we move towards the top boundary. As a consequence, the drop size distribution along the vertical direction starts to change; larger droplets are observed at the bottom whereas the smaller droplets are at the top of the domain.

Filaments stage

Once drops start to significantly coalesce, the drop size distribution changes significantly. Bigger droplets settle with higher velocities. This causes larger velocity fluctuations than in the coalescence stage. In this process, drops experience large shear, which leads to filament formation and breakup, as evidenced in Figure 3.7. This figure corresponds to simulation time $t = 305$ where significant film formation starts to occur in all regions of the domain, as displayed in Figures 3.7b, 3.7c and 3.7d.

Separation stage

There is significant coalescence in the filament formation stage, which leads to separation of the two phases. In our simulation there are many tiny drops distributed in the two separated phases as shown in Figure 3.8. This figure corresponds to simulation time $t = 900$ where the two phases have been completely separated. The interface between the two phases is perturbed by the coalescence of the tiny droplets and waves are formed under the action of both gravity and surface tension. As the simulation corresponds to $Ar = O(1)$ these capillary and gravity waves are damped by the viscous dissipation over a finite time. The waves corresponding to the interface and small drops can be seen in the zoomed white box region in Figure 3.8a displayed in 3.8b.

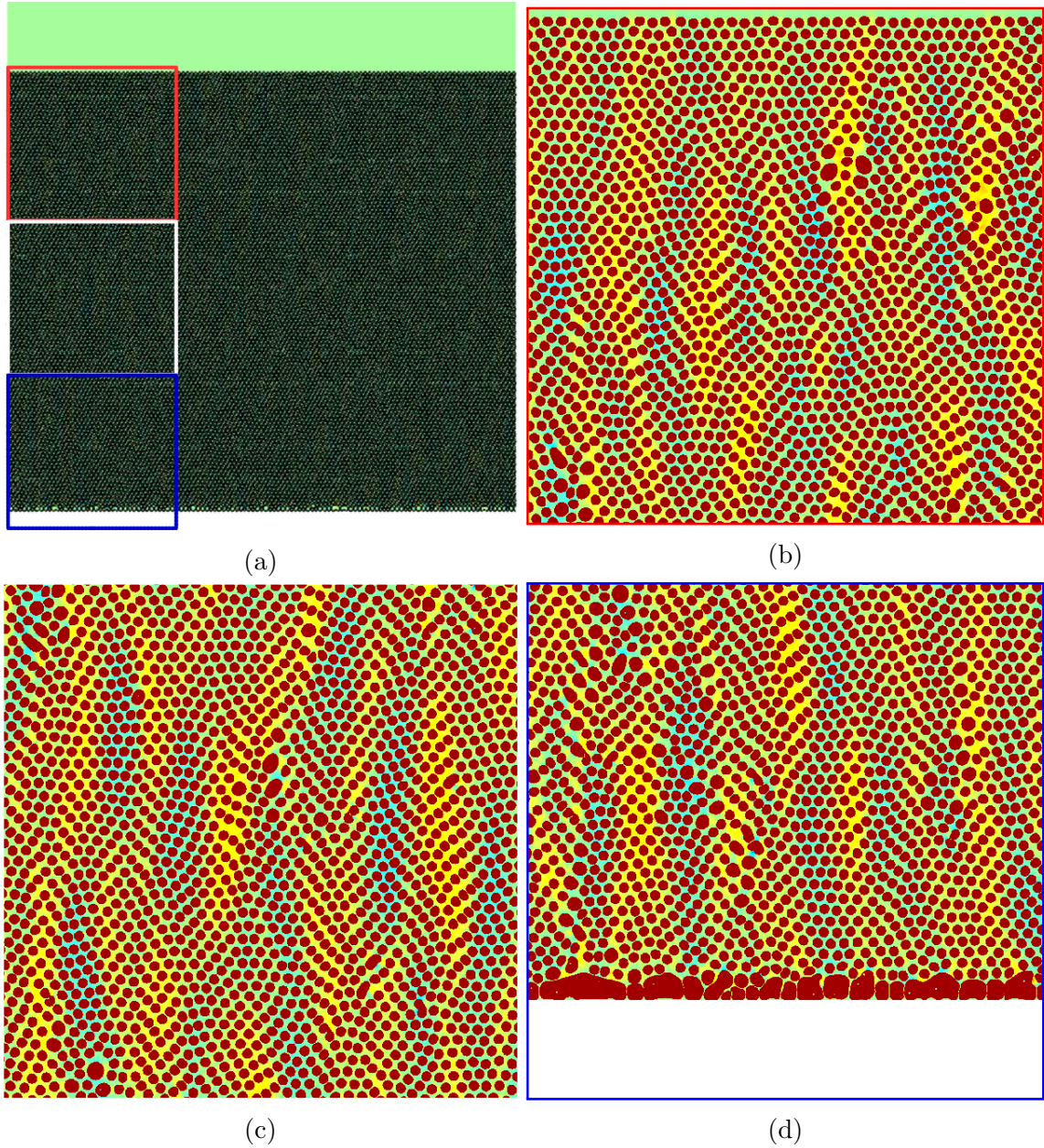


Figure 3.5: A 2D domain with $\frac{L}{D} = 156$ at intermediate stage corresponding to simulation time $t = 140$. Full domain in Figure 3.5a with 3 colored regions zoomed by 3x (partial domains) in Figures 3.5b, 3.5c and 3.5d. Vertical channels appear in this stage with limited numerical coalescence.

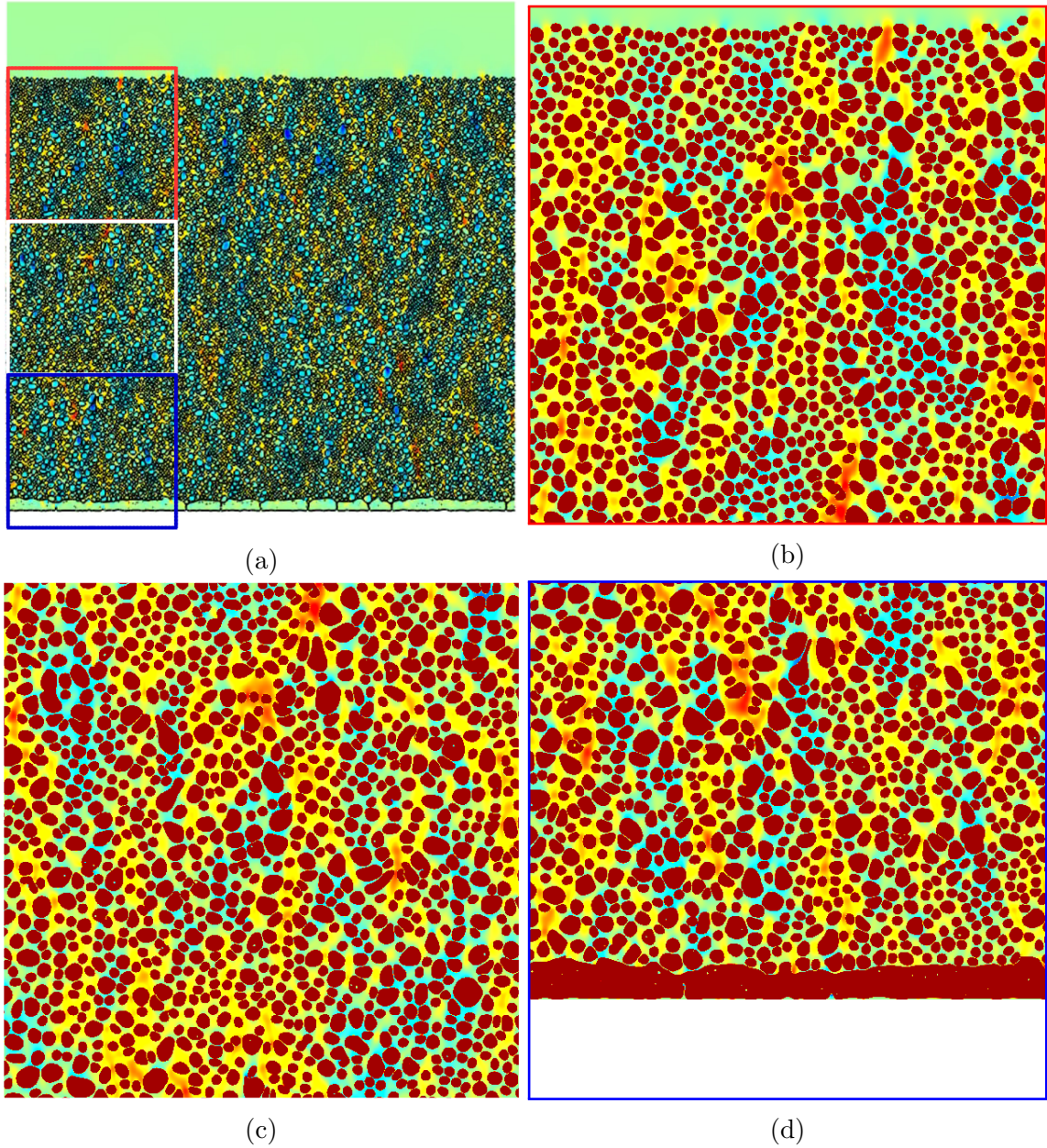


Figure 3.6: A 2D domain with $\frac{L}{D} = 156$ at coalescence stage corresponding to simulation time $t = 200$. Full domain in Figure 3.6a with the 3 colored box regions zoomed by 3x in Figures 3.6b, 3.6c and 3.6d. Significant (numerical) coalescence occurs in this stage with a significant effect on the droplet size distribution.

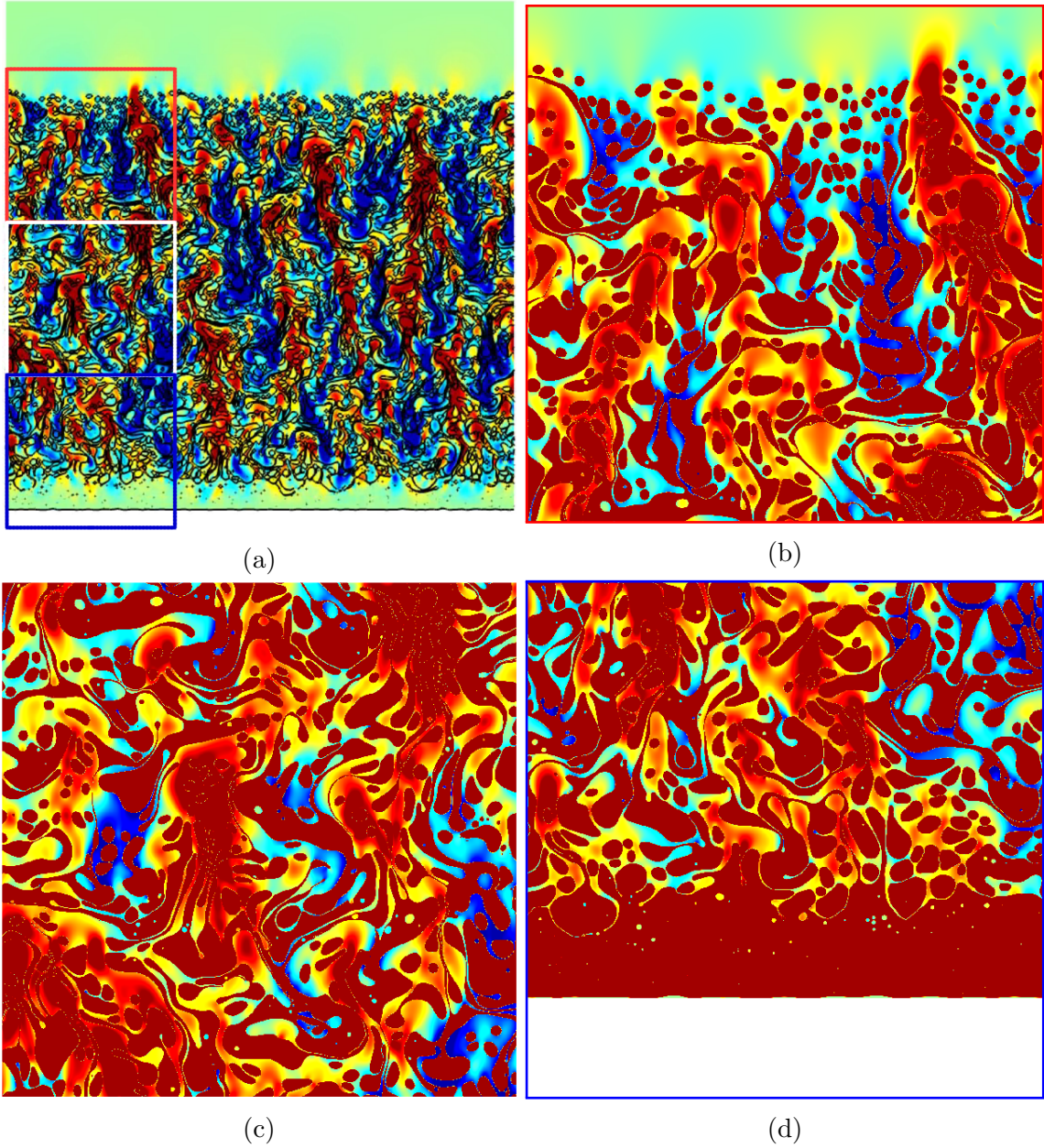
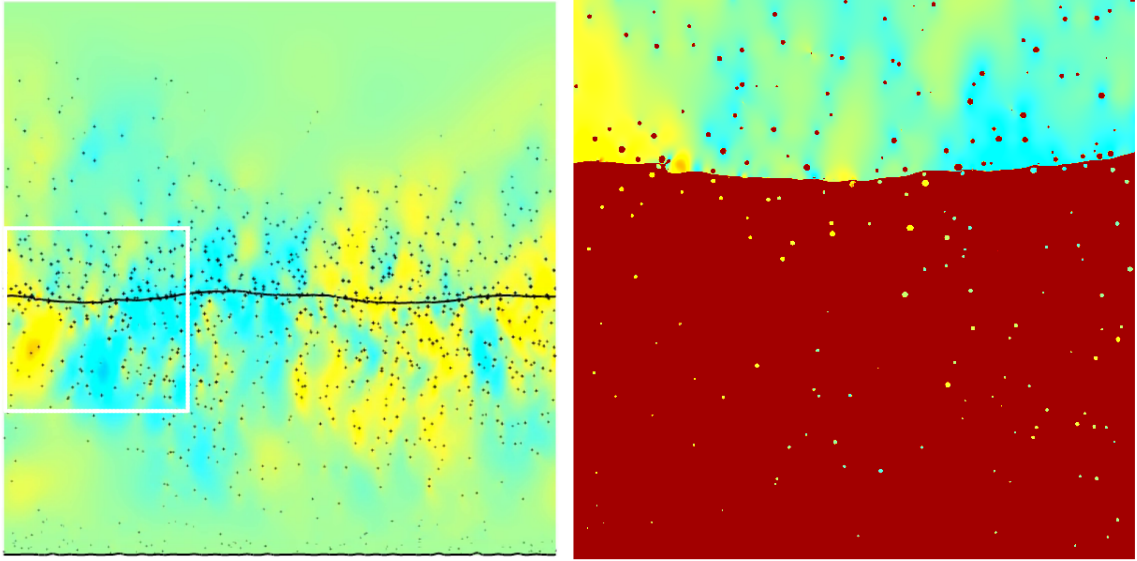


Figure 3.7: A 2D domain with $\frac{L}{D} = 156$ at the filaments stage corresponding to simulation time $t = 305$. Full domain in Figure 3.7a with 3 colored box regions zoomed by 3x in Figure 3.7b, 3.7c and 3.7d.



(a) Full domain with a white box region zoomed by 3x in Figure 3.8b. (b) Partial domain corresponding to the white box in Figure 3.8a.

Figure 3.8: A 2D domain with $\frac{L}{D} = 156$ at separated stage corresponding to simulation time $t = 900$. In this stage the two phases are completely separated except for the presence of tiny droplets.

3.2.2 Quantitative analysis

Profiling

The profiling is performed on some of the field variables to evaluate some macroscopic properties of the system.

The density and velocity profiles are evaluated. The density profiles are computed along the vertical direction. Each velocity component profile is computed along both horizontal and vertical directions.

TO generate a profile along the k^{th} direction, we divide the span L along x or y direction into the desired number of divisions, N . A field A_{ij} corresponding to the i^{th} row and the j^{th} column for a 2D finite volume grid is shown in Figure 3.9. To compute a vertical profile, we compute the average of field A in each red rectangle of Figure 3.9: $A_k = \frac{\sum_i A_{ik}}{\sum_i 1}$, where $k \in 1, 2, 3, \dots, N$. The set of A_1, A_2, \dots, A_N are the profile values.

Density profile

Following the procedure described above, the vertical density profile is calculated from the VOF field f of the simulation at the initial time, as shown in Figure 3.10, where dots represent the profile values. Here f represents the volume fraction of the drop phase in each bin (the bins are the red rectangles shown in Figure 3.9).

The initial density profile has a clear periodic structure close to a sine function. This is due to our initial distribution of drops. If our initial distribution of drops had been an exact hexagonal packing, the profile would have been perfectly periodic.

As the drops settle due to gravity, the corresponding density profiles will start to compress as shown in Figure 3.11.

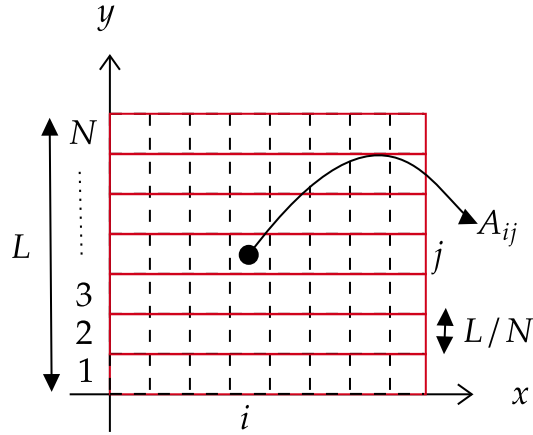


Figure 3.9: Profiling of field values along the vertical direction of a 2D L square domain in bins numbered 1, 2, 3,...,N, where each bin height is $\frac{L}{N}$.

The evaluation of the macroscopic parameters of the system, such as the evolution of the leading and trailing edge of the separation front, will be described in the next sections.

Separation front

The evolution of an emulsion can be described by a directly observable experimental parameter, which is the propagation of the phase fronts also called separation front. In our mono-dispersed two-phase emulsion, initially there are two separation fronts, one at the top and one at the bottom as shown in Figure 3.12a. These two fronts propagate downwards as drops settle under gravity. As shown in Figure 3.12b the bottom separation front disappears once the bottom layer of drops reaches the boundary.

As the simulation further evolves the drop phase starts to coalesce at the bottom, forming a film leading to another separation front as shown in Figure 3.12c. Now we have two separation fronts, one at the top propagating downwards and one at the bottom propagating upwards. We denote the top separation front which is travelling downwards as the trailing edge and the bottom separation front which is travelling upwards as the leading edge as shown in Figure 3.12d. The positions of the trailing edge and leading edge phase fronts can also be evaluated using the density profiles. We define the trailing edge as the maximum y -position corresponding to a density profile value greater than 0.25, whereas the leading edge front is defined as the maximum y -position corresponding to a density profile value greater than 0.95. Let us say f_k are the average values of the volume fraction computed in horizontal bins located at different vertical positions, as shown in Figure 3.9. Let us say that the corresponding vertical position of f_k are y_k . For the trailing edge:

$$\max_{j: y_j \in y(f_k > 0.25)} y_j \quad (3.2)$$

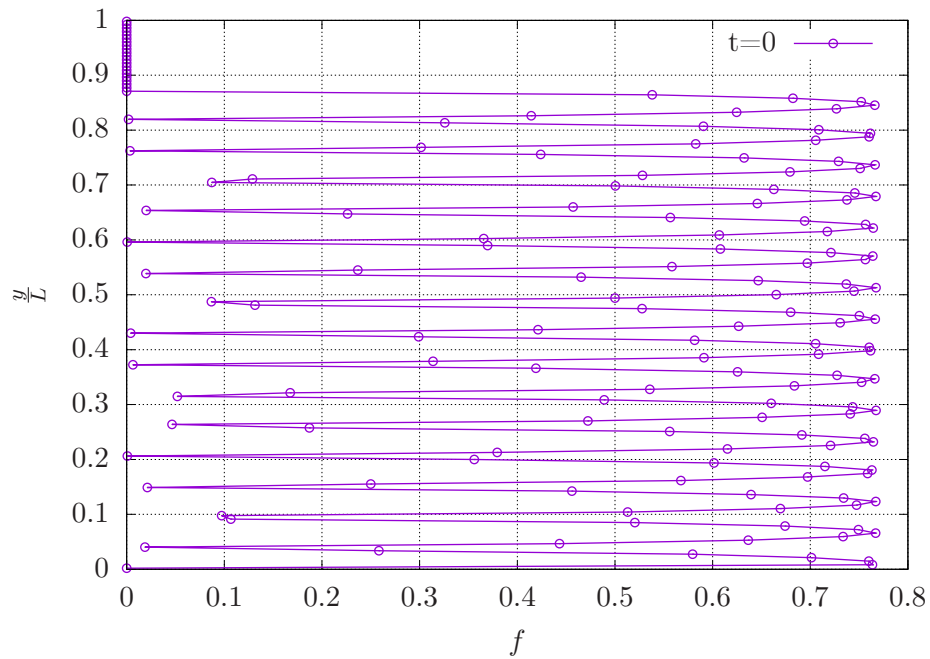


Figure 3.10: Density profile at the initial time of the simulation, where the vertical axis is the vertical position normalized with the domain size, $\frac{y}{L}$ and the horizontal axis corresponds to the average volume fraction.

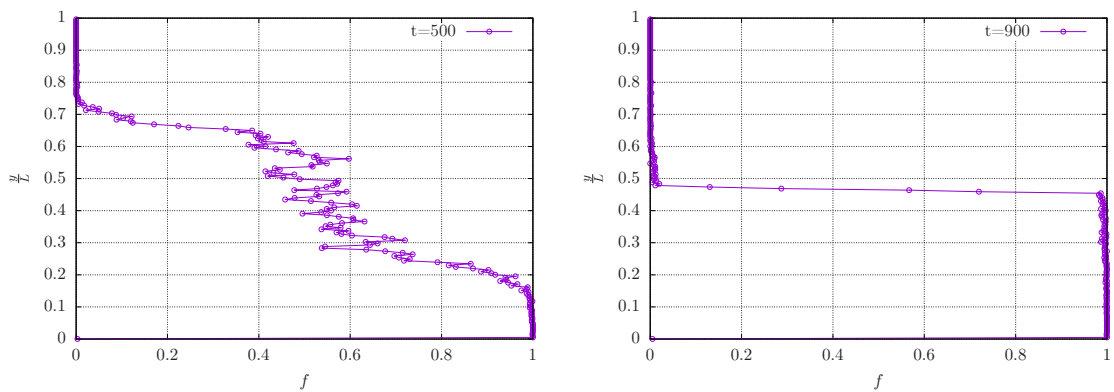
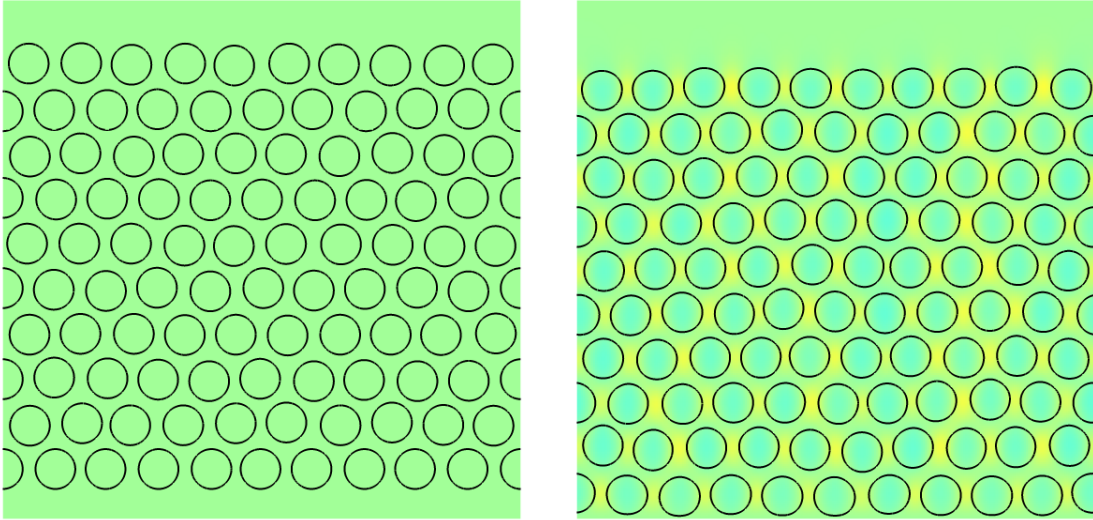
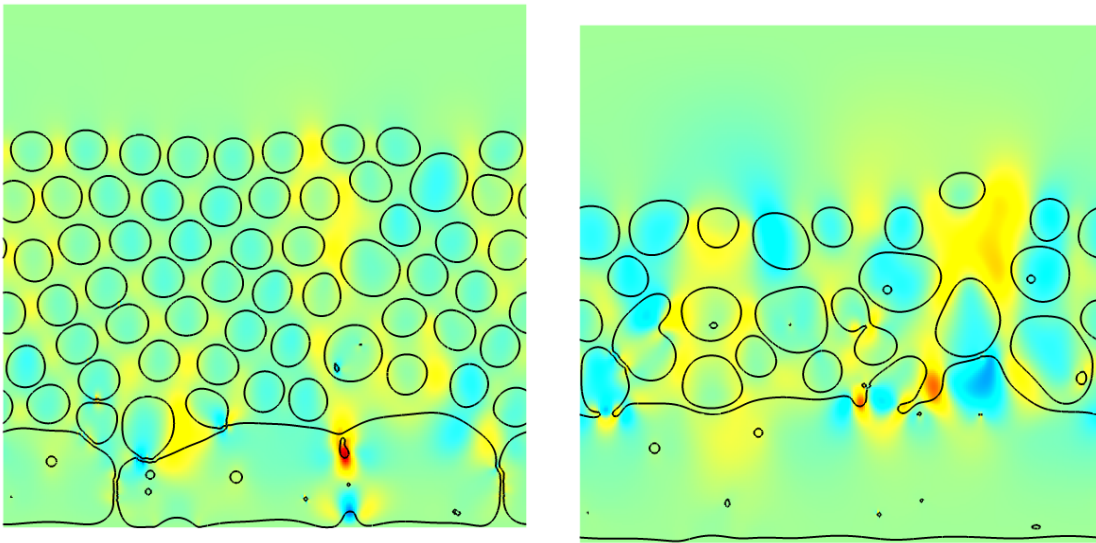


Figure 3.11: Density profiles at different simulation times $t = 500$ and $t = 900$, depicting the settling of drops.



(a) Two separation fronts located at the top and bottom, both propagating downwards. (b) One separation front located at the top propagating downwards.



(c) Two separation fronts located at the top and bottom. Where the top front is propagating downwards and the bottom front is just appearing. (d) Here the top front is propagating downwards and the bottom front is propagating upwards.

Figure 3.12: Leading and trailing edge evolution of an emulsion of $\frac{L}{D} = 13$ settling under gravity. Depiction of the phase fronts known as the trailing edge and the leading edge at different time intervals $t = 0$, $t = 40$, $t = 140$ and $t = 200$ corresponding to Figure 3.12a, 3.12b, 3.12c and 3.12d respectively.

Similarly for the leading edge:

$$\max_{j:y_j \in y(f_k > 0.95)} y_j \quad (3.3)$$

These values are chosen to ensure that in the presence of small isolated drops, their interface will not be detected as a separation front.

To evaluate the separation front evolution, the evolution of the density profiles with time must be computed. This is demonstrated in Figure 3.13, where three density profiles at three different times are presented as shown in Figure 3.13a, 3.13b and 3.13c, along with the propagation of the trailing and leading edge over time as shown in Figure 3.13d. Using equations 3.2 and 3.3 the trailing edge and leading edge are computed and represented by colored dots on the density profiles in Figures 3.13a, 3.13b and 3.13c. The y values corresponding to these colored dots are plotted as the separation front curve in Figure 3.13d.

Following the procedure explained above, the separation front evolution of $\frac{L}{D} = 156$ is computed, and displayed in Figure 3.14.

The (black) trailing edge in Figure 3.14 evolves in several distinct stages. An initial stage corresponds to the pure settling of the drops without any coalescence. Then, drops start to coalesce, where the first coalescence is denoted by a green dot in Figure 3.14. After this point the slope of the trailing edge curve starts to change, corresponding to more complex structures in the emulsion as shown in Figure 3.7. This curve evolves with the same slope until the two phases are completely separated. There is then a transition to a new stage. In this stage the trailing edge reaches the constant value. The curve is oscillatory in this stage due to the presence of gravity and capillary waves. Over time, these oscillations should be damped and a straight line be reached.

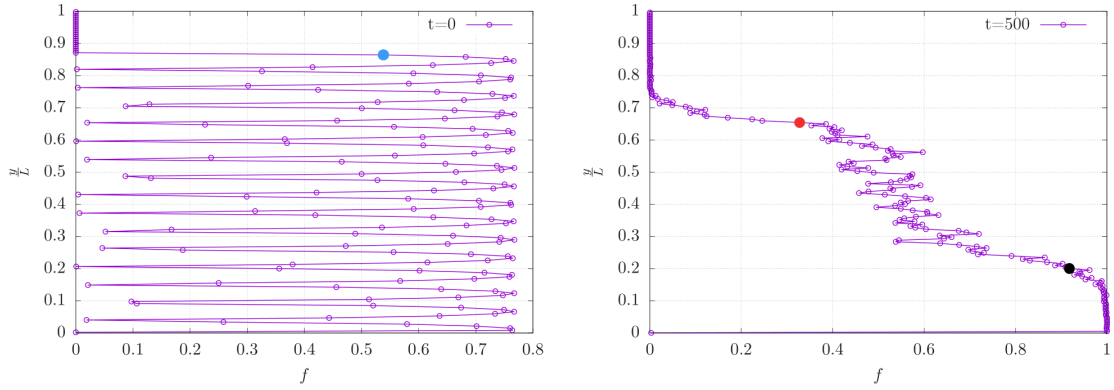
Another observable phase-front is the leading edge represented in purple in Figure 3.14. As drops settle down and start to coalesce, a pool of liquid is formed at the bottom boundary. As drops further settle down coalescing into this pool the phase front corresponding to this pool starts to propagate upwards. This phase front is known as the leading edge. The evolution of the leading edge in blue in Figure 3.14 looks qualitatively similar to that of the trailing edge. Trailing edge and leading edge merge as the two phase completely separate. The slight gap between the trailing edge and the leading edge curves in Figure 3.14 is due to the criteria that we have chosen to define those two curves.

Evaluating these curves might help engineers working in the industry to focus on specific stages of the settling emulsion, in order to accelerate the settling process. 2D vs 3D?

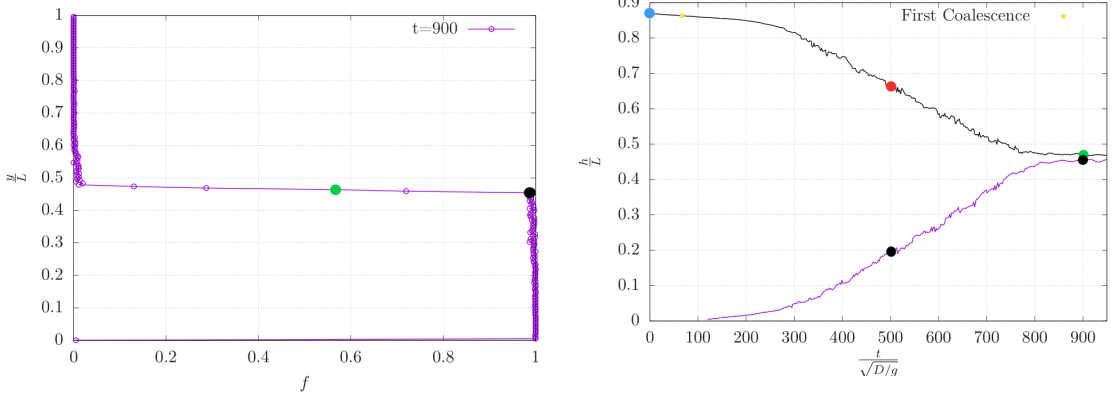
Coalescence frequency

Tracking the number of drops over time is possible due to the tag function 2.3. This evolution is plotted in Figure 3.15, where the number of drops are evaluated at time intervals of 1.

Four different stages of evolution of the number of drops can be observed in Figure 3.15 and 3.16. The number of drops does not change until a certain time, which corresponds to the pure settling of drops without any coalescence. The coalescence frequency, the change in number of drops per unit of time, obtained through computing $n_{t+1} - n_t$ is plotted with a frequency of sampling $\frac{1}{10}$ in Figure 3.16. As the



(a) Density profile at time $t = 0$, where there is only a trailing edge represented by the blue dot. (b) Density profile at time $t = 500$, where the trailing edge is represented by the red dot and the leading edge by the black dot.



(c) Density profile at time $t = 900$, where the trailing edge is represented by the green dot and the leading edge by the black dot. (d) Leading and trailing edge propagation evolution over time along with the coloured dots corresponding to different density profiles.

Figure 3.13: Leading and trailing edge evolution of the 14400-drops simulation computed with the help of density profiles. Three density profiles at time $t = 0, 500$ and 900 are shown along with their trailing and leading edge position on the separation front curve represented by coloured drops. The blue dot on the density profile at $t = 0$ corresponds to the trailing edge at $t = 0$, similarly the red dot on the density profile at $t = 500$ corresponds to the trailing edge at $t = 500$, similarly for the leading edge with the black dot. Repeating this at the desired time intervals result in the separation front curve evolution over time as shown in Figure 3.13d.

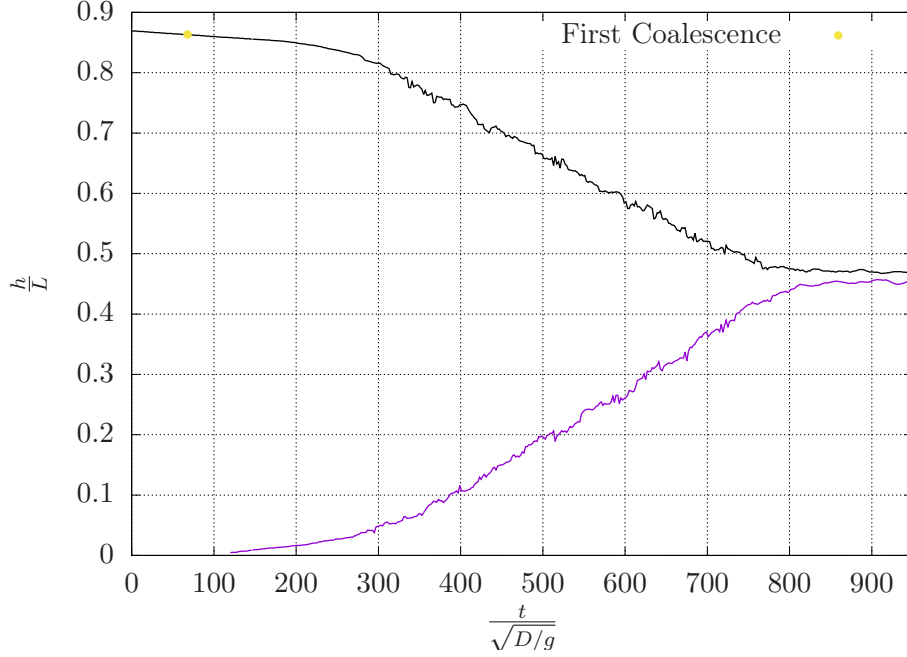


Figure 3.14: Trailing and leading edge propagation curve in a coalescing emulsion of $\frac{L}{D} = 156$.

drops start to coalesce the number of drops starts to decrease with an increasing coalescence frequency. This can be observed in Figure 3.16 and 3.15. There is a stage where this coalescence frequency is maximum, at around 190 drops per characteristic time, at around simulation time $t = 150$. The number of drops further decreases as coalescence proceeds but at a slower rate. This can be observed in Figure 3.15 and 3.16. This can be due to the fact that the larger the drops, the larger the Bo , therefore the longer they take to coalesce.

Another stage appears where the rate at which the drops coalesce is much less compared to before, this can be due to two reasons. First, because of the formation of large drops and the second, due to the formation of filaments breaking larger drop into a few smaller drops. This contributes to the generation of new drops.

In the qualitative analysis we have described several stages observed through simulation images representing the y-velocity field and the drops. We have observed filament formation at simulation time $t = 305$ as shown in Figure 3.7. During these stages the coalescence frequency is decreasing as observed from Figure 3.16.

In Figure 3.15 one can observe that along most of the curve there are no upper peaks. Some upper spikes of evolution of number of drops are observed after simulation time $t = 350$. This indicates that coalescence is the dominating process at all times in the evolution of the emulsion.

These small spikes which are observed after $t = 350$ indicate that there is a net production of drops. Due to the generation of many tiny drops along with filament breakup.

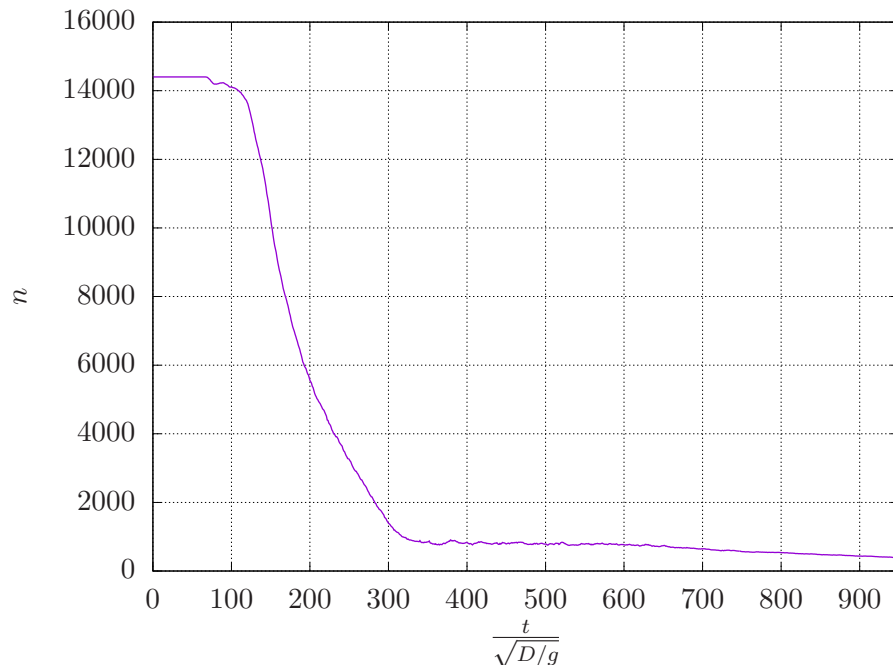


Figure 3.15: Evolution of the number of drops in a coalescing emulsion of $\frac{L}{D} = 156$.

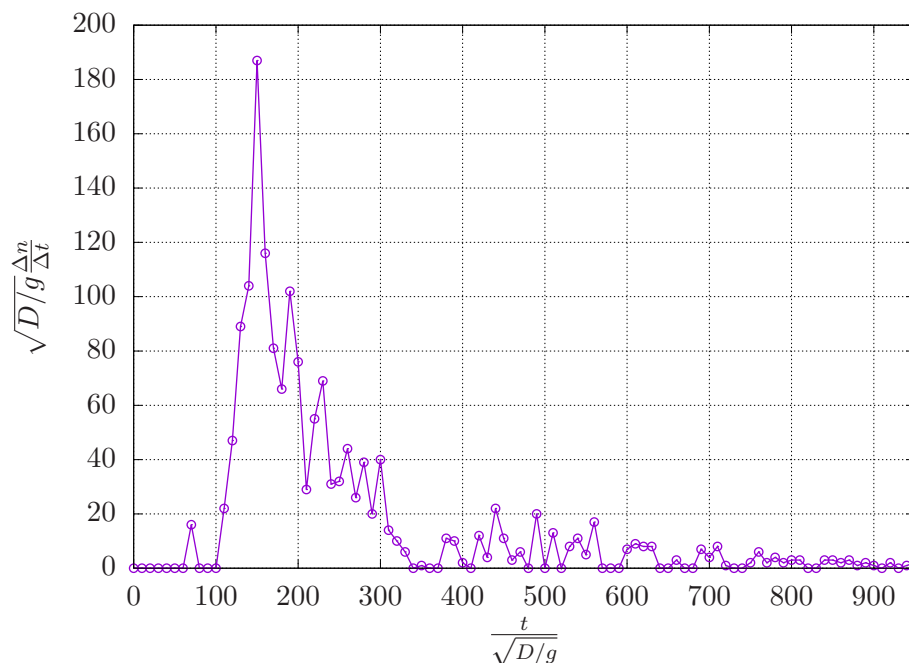


Figure 3.16: Coalescence frequency evolution over time for the case with $\frac{L}{D} = 156$. This is computed as the rate of change of number of drops over time from Figure 3.15.

3.2.3 Effect of resolution on numerical coalescence

In the simulation of emulsions where multiple drops are represented by a single color function, drops coalesce when they are closer than the mesh size. This numerical coalescence can be delayed using finer mesh.

Thus, a change in resolution while using a single color function could impact the whole emulsion characteristics. Variables such as the separation front position and coalescence frequency could be impacted. It could thus be interesting to observe the evolution of these parameters as the resolution is varied.

To observe these changes a test case of $\frac{L}{D} = 13$ in a 13×13 domain is simulated with three different resolutions: 20, 40 and 80 points per drop diameter. The evolution of the separation front and number of drops are evaluated and compared for these three cases.

Separation front

The trailing edge evolution has been computed for three different resolutions and plotted in Figure 3.17.

Three different stages can be observed. Before the first coalescence, represented by the circular points, the plots corresponding to these three resolutions almost coincide with each other. This indicates that there is no impact of resolution on the settling stage for this emulsion. As there is no coalescence in this stage we should not expect any impact due to the coalescence, but at the same time this also confirms that 20 points per drop diameter is sufficient to resolve the settling of drops.

When only a few drops coalesce, the impact of mesh resolution is not significant on the separation front evolution (until the red dot). But as soon as the coalescence process is increasing, the impact of the mesh resolution is greater and visible on the separation front. This can be clearly observed in 3.17, where the trailing edge corresponding to three different resolutions evolve with different slopes. Once full separation is reached, it is obvious that the resolution will not have any impact on the solution.

Coalescence frequency

Altering the coalescence by varying the mesh size should have a direct impact on the evolution of the number of drops and on the coalescence frequency.

Similar to the case of trailing edge evolution, we evaluate the number of drops over time for three different resolutions: 20, 40 and 80 points per drop diameter for a $\frac{L}{D} = 13$ test case. This is plotted in Figure 3.18, where we can observe different stages in the evolution.

The first stage corresponds to no-coalescence with pure settling, where all of the curves merge as expected. As coalescence begins the number of drops starts to decrease. The rate of decrease of the number of drops for these three different resolutions appear to be different, which is as expected. This is useful when we demonstrate the control of coalescence 3.4.

As we use a finer mesh, we should expect a delay in coalescence hence a reduction in the coalescence frequency. This is clearly observed in Figure 3.18.

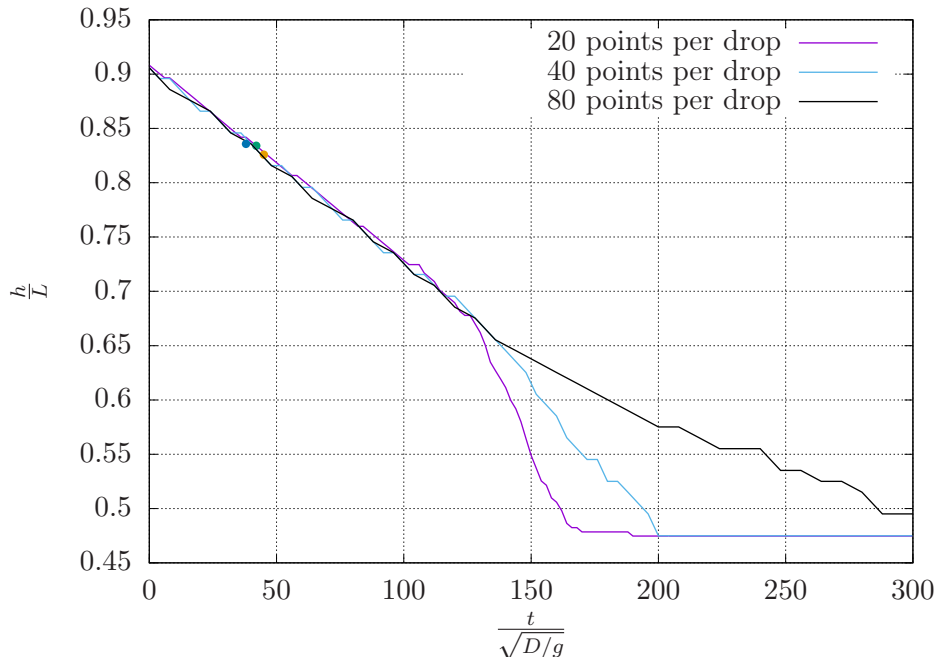


Figure 3.17: Evolution of the trailing edge corresponding to the emulsion simulation of $\frac{L}{D} = 13$ for three different resolutions: 20, 40 and 80 points per drop diameter. The first coalescence corresponding to these three test cases are represented by circular dots.

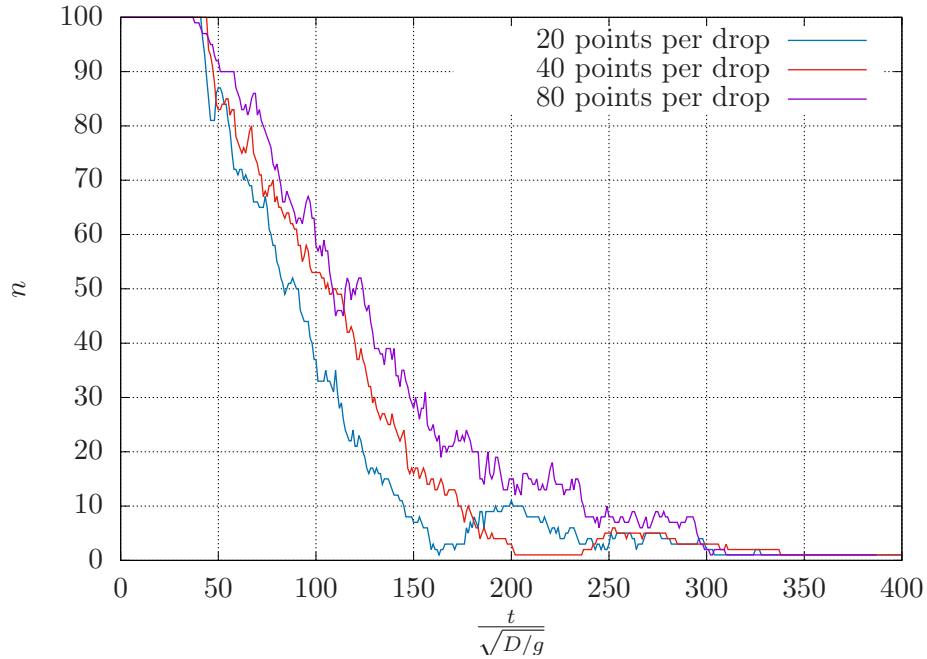


Figure 3.18: Evolution of the number of drops corresponding to the emulsion simulation of $\frac{L}{D} = 13$ for three different resolutions: 20, 40 and 80 points per drop diameter.

3.2.4 Effect of domain size in coalescing emulsions

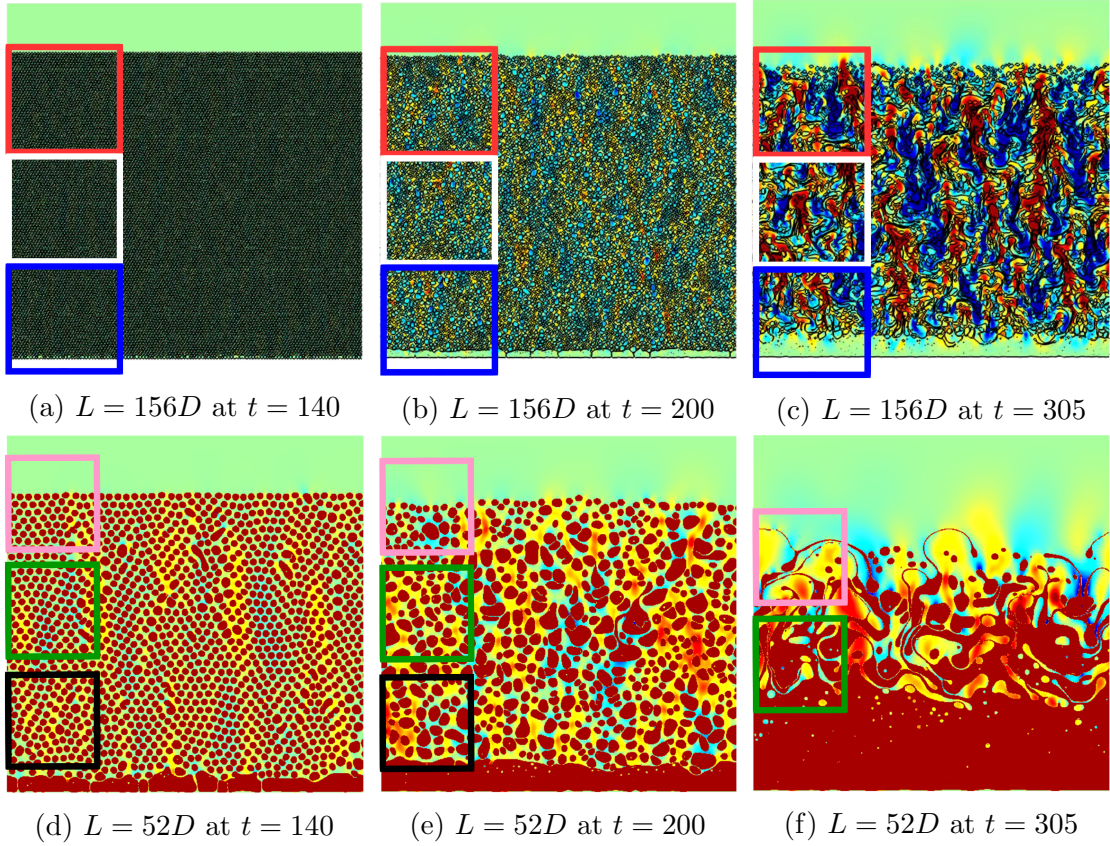


Figure 3.19: Simulation snapshots corresponding to $\frac{L}{D} = 52, 156$ at simulation times $t = 140, t = 200$ and $t = 305$. Drops are red colored in the $\frac{L}{D} = 52$ case. The surrounding phase in the $\frac{L}{D} = 52$ case and both phases in the $\frac{L}{D} = 156$ case are represented by the y-velocity field. The color scale for the y-velocity is between blue to red for a magnitude in $[-0.1 : 0.1]U$. The colored boxed regions of the $\frac{L}{D} = 156$ case in Figure 3.19a, 3.19b and 3.19c are subdomains corresponding to the $\frac{L}{D} = 52$ case. Similarly the colored boxed regions of the $\frac{L}{D} = 52$ case in Figure 3.19d, 3.19e and 3.19f are subdomains corresponding to the $\frac{L}{D} = 13$ case. The subdomains are presented in Figure 3.20, 3.21, 3.22, 3.21 and 3.24 with colored borders which exactly correspond to the same colored box in the full domain.

The effect of domain size in gravity-settling emulsions is discussed in this section. The figures corresponding to the three different domain sizes are compared with each other to find the existence and non-existence of the different stages and also to point out the similarities found between them.

Qualitative analysis

To compare different domain size test cases, the subdomains are chosen at the top, middle and bottom regions on the left side of the full domain as shown in Figure 3.19. The subdomain size of the $\frac{L}{D} = 52$ case is exactly the same as that of the full domain size for $\frac{L}{D} = 13$, similarly the subdomain size of the $\frac{L}{D} = 156$ case is exactly the same as that of the full domain for $\frac{L}{D} = 52$, as shown in Figure 3.19, 3.20, 3.21, 3.22, 3.21 and 3.24.

Bo	Ar	ρ_r	μ_r	$\frac{L}{D}$	n	$\frac{D}{P}$
2.5	1.388	0.8	2	13, 52, 156	100, 1600 and 14400	20-26

Table 3.3: Simulation parameters corresponding to $\frac{L}{D} = 13, 52, 156$ test cases.

Settling stage

In this stage drops simply settle down in a similar fashion in all of the three domains under the influence of gravity, without showing any instabilities. In this stage drops reach a terminal velocity.

Intermediate stage

As the emulsion evolves we can observe an instability manifesting itself as alternating vertical channels shown by the y-velocity field. The drops and the y-velocity of the surrounding phase, corresponding to the intermediate stage at simulation time $t = 140$, are shown in Figure 3.20 and 3.21. Similarities are observed between the full domain of $\frac{L}{D} = 13$ and the subdomain of $\frac{L}{D} = 52$, as well as between the full domain of $\frac{L}{D} = 52$ and the subdomain of $\frac{L}{D} = 156$.

At time $t = 140$ the formation of vertical channels is observed in domains corresponding to the $\frac{L}{D} = 52$ and $\frac{L}{D} = 156$ as observed in Figure 3.21. These channels are absent for the smaller domain size. The wavelengths corresponding to the observed channels is around four droplet diameters as observed in Figure 3.21.

The top subdomain of the $\frac{L}{D} = 52$ test case in Figure 3.20b is similar to the full domain of the $\frac{L}{D} = 13$ test case in Figure 3.20a. If we now consider the middle and bottom subdomains as shown in Figure 3.20c and 3.20d respectively, we see that the $\frac{L}{D} = 13$ case starts to differ slightly in terms of both the y-velocity field and of the wavelength of the alternating vertical channels.

Coalescence stage

The drops continue to settle down in the intermediate stage, where they get closer and closer leading to many drops getting coalesced. The alternating vertical channels starts to disappear showing a transition to a new stage as shown in Figure 3.22 and 3.23 at simulation time $t = 200$.

Comparison between the $\frac{L}{D} = 52$ test case and the $\frac{L}{D} = 156$ case in Figure 3.22 shows similarities between the top subdomain of $\frac{L}{D} = 52$ with the full domain of $\frac{L}{D} = 13$ as shown in Figure 3.22b and 3.22a. In all of the subdomains larger drops appear in the $\frac{L}{D} = 52$ case compared to the $\frac{L}{D} = 13$ case. The middle and bottom subdomains show higher magnitude of the y-velocity field compared to $\frac{L}{D} = 13$ as shown in Figure 3.22. This could be due to the formation of large drops, which settle with a larger velocity.

Filament stage

The formation of large drops in the coalescence stage intensifies upon further coalescence, where these large drops start to form thin filaments as shown in Figure 3.24 at simulation time $t = 305$. These filaments then start to breakup.

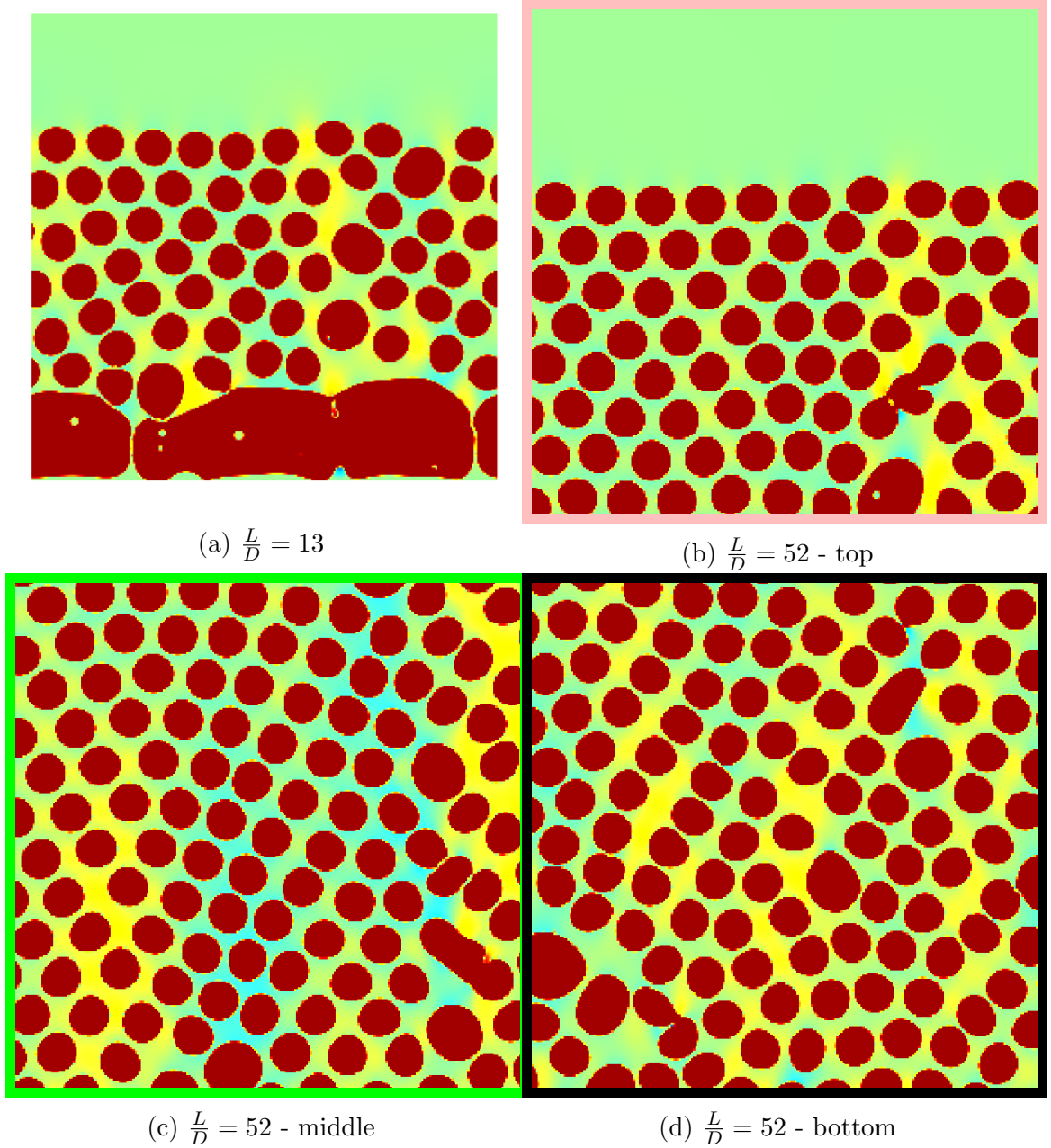


Figure 3.20: Comparison of a domain $\frac{L}{D} = 13$ to the subdomains of 52 case at $t = 140$ corresponding to an intermediate stage. The regions of subscaling corresponds to the colored boxes in Figure 3.19. Drops are red and the surrounding phase is colored with the magnitude of the y-velocity ranging from $[-0.1 : 0.1]U$ (blue to red).

Filament formation is not seen in the $\frac{L}{D} = 13$ case. But they start to appear in the $\frac{L}{D} = 52$ and $\frac{L}{D} = 156$ cases. This clearly shows the influence of the domain size.

As we decrease increase the domain size more drops are available for coalescence, leading to the formation of large drops. Large drops settle with higher velocity leading to a larger shear stress on the interface. As the drop size increases, the viscous shear forces start to dominate the capillary force. Due to these reasons the filaments are formed only in the large domain size cases.

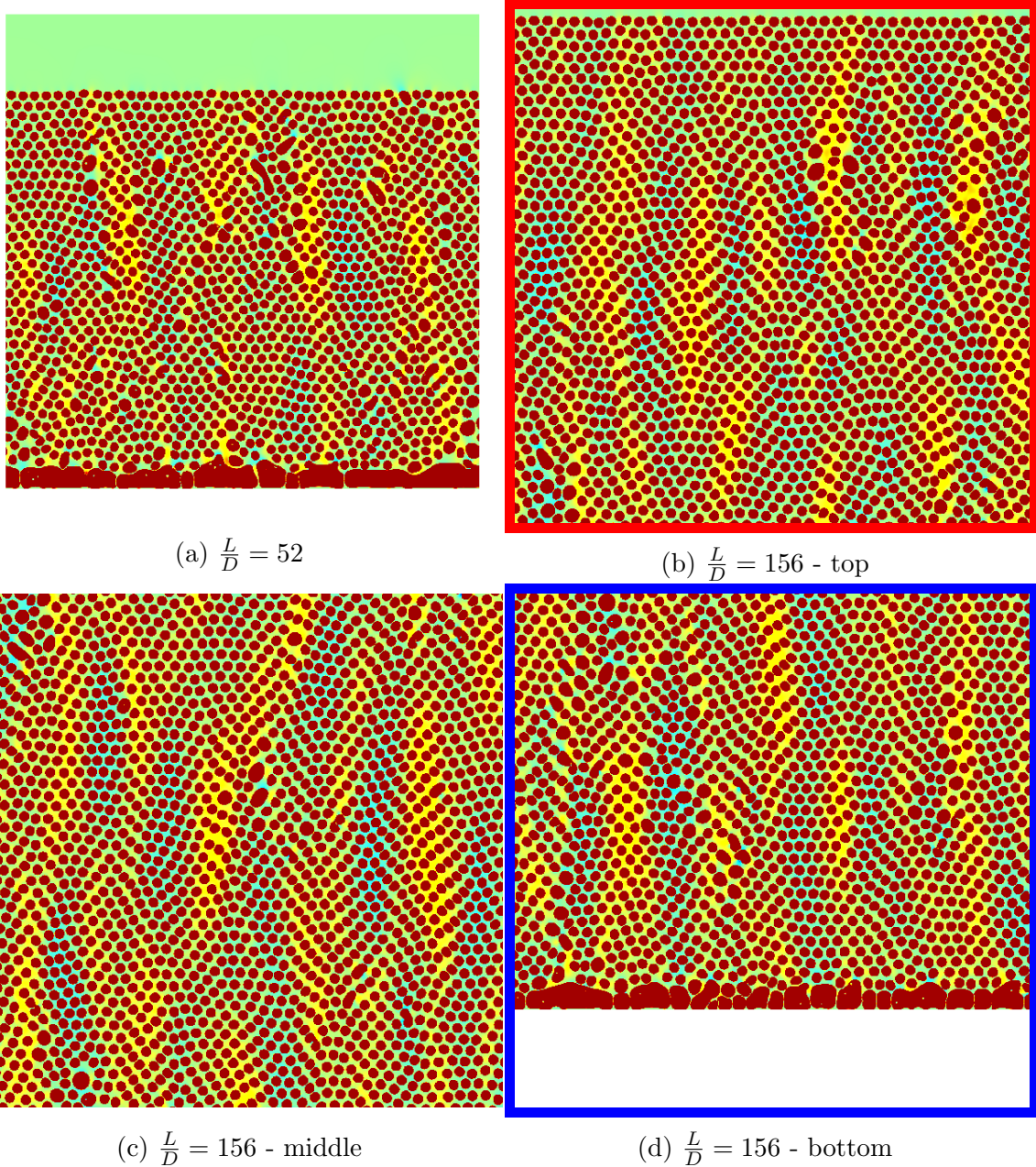


Figure 3.21: Comparison of a domain $\frac{L}{D} = 52$ to the subdomains of the 156 case at $t = 140$ corresponding to an intermediate stage. The regions of subscaling correspond to the colored boxes in Figure 3.19.

Separated stage

As drops breakup and coalesce in the filament stage, the two phases are eventually separated. This stage is seen in all of the cases irrespective of the domain size.

Qualitatively observing the differences in different domain sizes have shown a minimum size necessary to capture all of the effects, which is a 52×52 domain consisting of $\frac{L}{D} = 52$. The smaller domain ($\frac{L}{D} = 13$ case) did not display vertical channels and filament formation, which clearly shows the influence of the domain size.

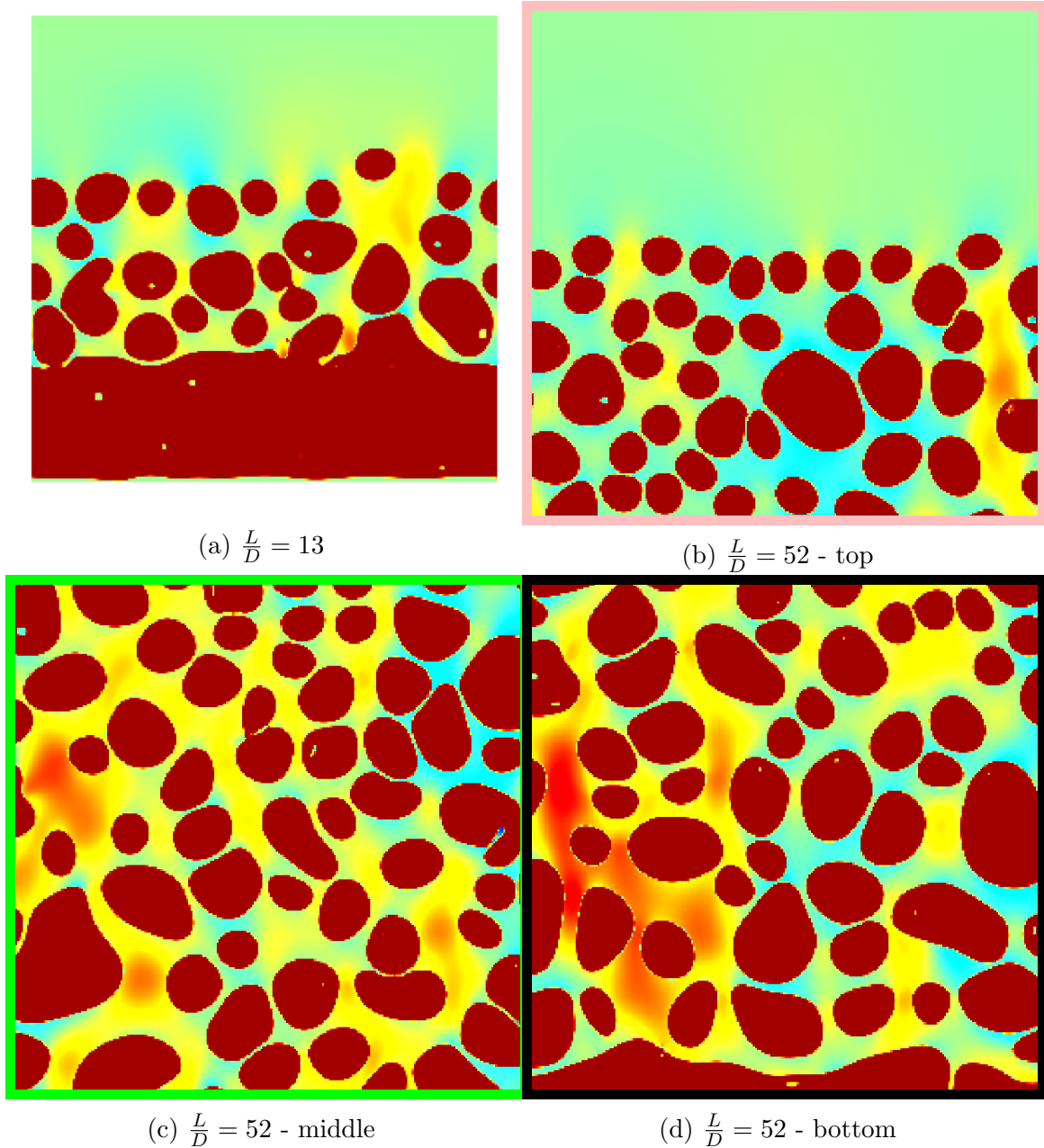
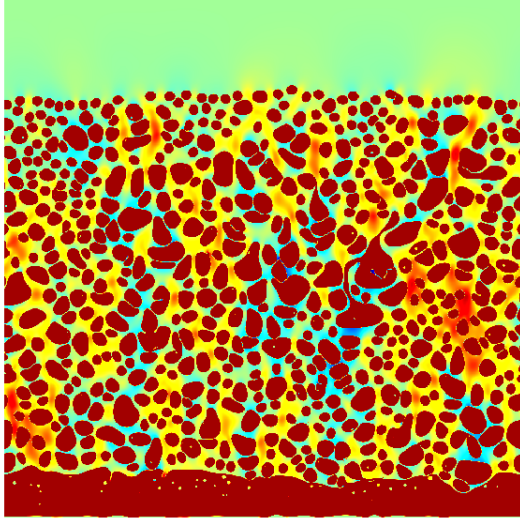


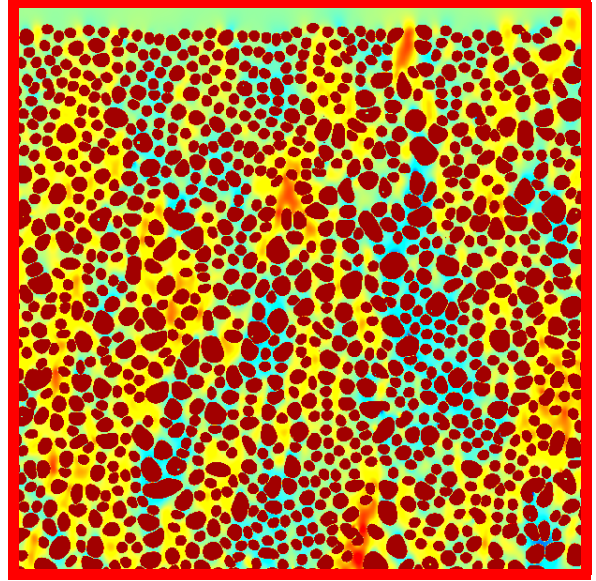
Figure 3.22: Comparison of a domain $\frac{L}{D} = 13$ to the subdomains of the 52 case at $t = 200$ corresponding to the coalescence stage. The regions of subscaling corresponds to the colored boxes in Figure 3.19.

Quantitative analysis

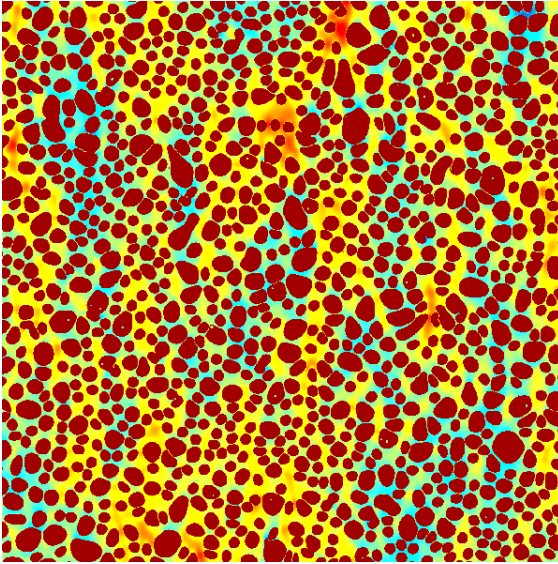
The effect of domain size has been studied through analyzing system parameters corresponding to different domain sizes. The trailing edge, number of drops and drift velocity curves are evaluated for three different sized domains $\frac{L}{D} = 13, 52, 156$ consisting of 100, 1600 and 14400 drops with a mesh resolution of 20 to 25 points per drop. The results are plotted in Figure 3.25, 3.26, 3.27, and 3.28.



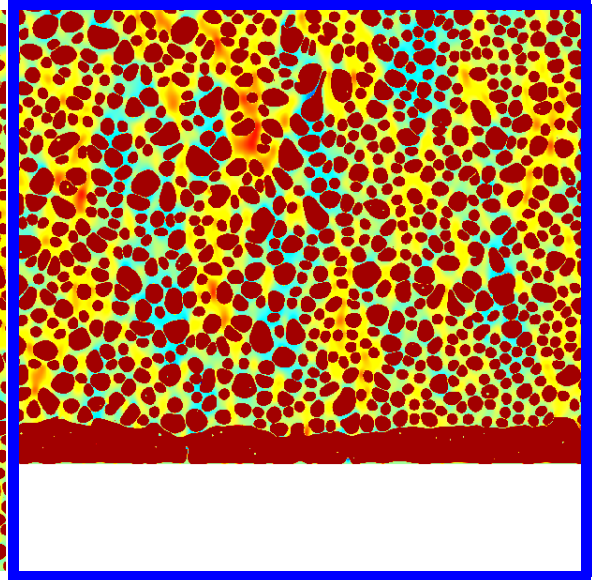
(a) $\frac{L}{D} = 52$



(b) $\frac{L}{D} = 156$ - top



(c) $\frac{L}{D} = 156$ - middle

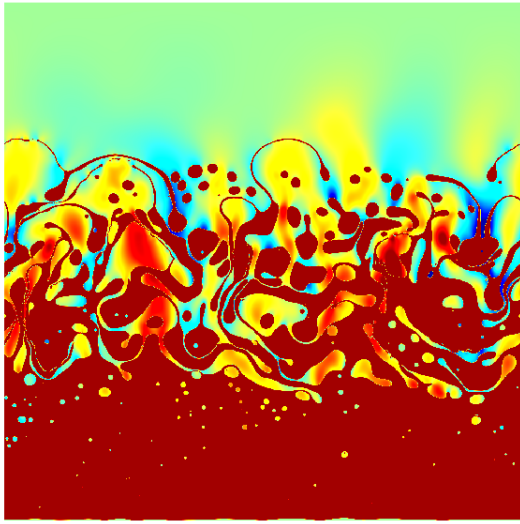


(d) $\frac{L}{D} = 156$ - bottom

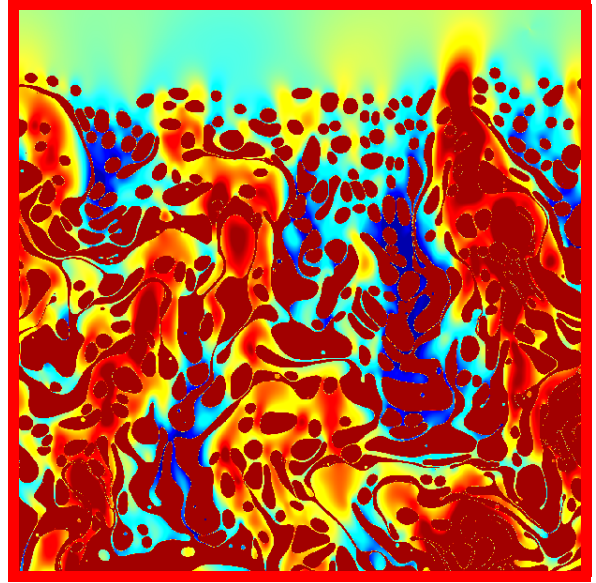
Figure 3.23: Comparison of a domain $\frac{L}{D} = 52$ to the subdomains of the 156 case at $t = 200$ corresponding to the coalescence stage. The regions of subscaling corresponds to the colored boxes in Figure 3.19.

Separation front

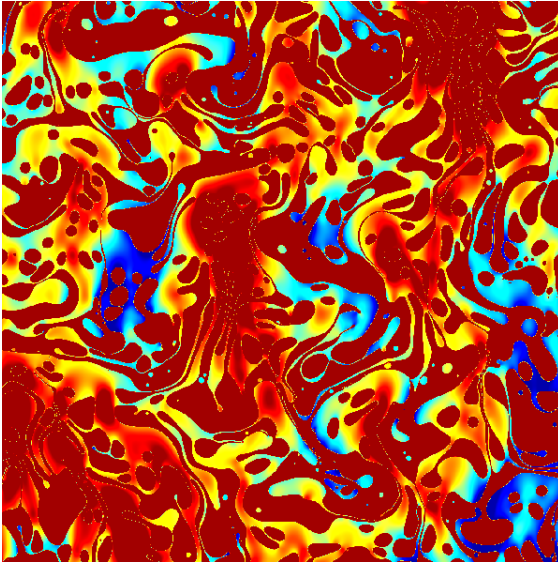
The evolution of the trailing edge corresponding to three different test cases $\frac{L}{D} = 13, 52, 104$ are plotted in Figure 3.25, where the time is scaled based on the characteristic length scale as droplet diameter D . Here we can observe that the black color plot corresponding to the $\frac{L}{D} = 13$ case is distinct from plots corresponding to $\frac{L}{D} = 52$ & 156. However curves corresponding to $\frac{L}{D} = 52$ & 156 cases almost coincide with each other. The $\frac{L}{D} = 52$ case is thus sufficient to capture the phase front evolution of a larger emulsion. This observation is consistent with the conclusion drawn in the qualitative section 3.2.4.



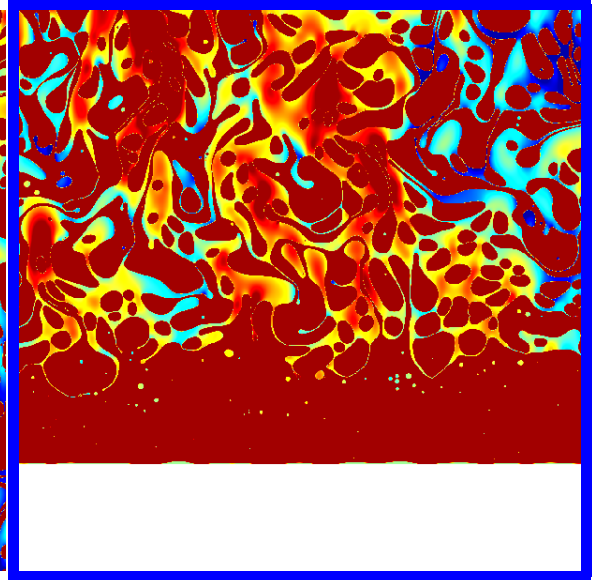
(a) $\frac{L}{D} = 52$



(b) $\frac{L}{D} = 156$ - top



(c) $\frac{L}{D} = 156$ - bottom



(d) $\frac{L}{D} = 156$ - bottom

Figure 3.24: Comparison of a domain $\frac{L}{D} = 52$ to the subdomains of the 156 case at $t = 305$ corresponding to the filament stage. The regions of subscaling correspond to the colored boxes in Figure 3.19.

Coalescence frequency

Figure 3.26 represents the time evolution of the dimensionless number of drops for 3 different domain sizes. The slope of these curves corresponds to the rate of coalescence, i.e. the coalescence frequency. We observe in Figure 3.26 three different stages; settling stage, coalescence stage and separated stage. First, the settling stage with a very low coalescence frequency, characterized by a low slope. This settling stage is very short for the $\frac{L}{D} = 13$ case and the transition between the settling stage to the coalescing stage is very abrupt. However, the transition is smoother for both the $\frac{L}{D} = 52$ & 156 cases. Then during the coalescence stage, the coalescence frequency is roughly the same for all of the cases, since the 3 curves are parallel.

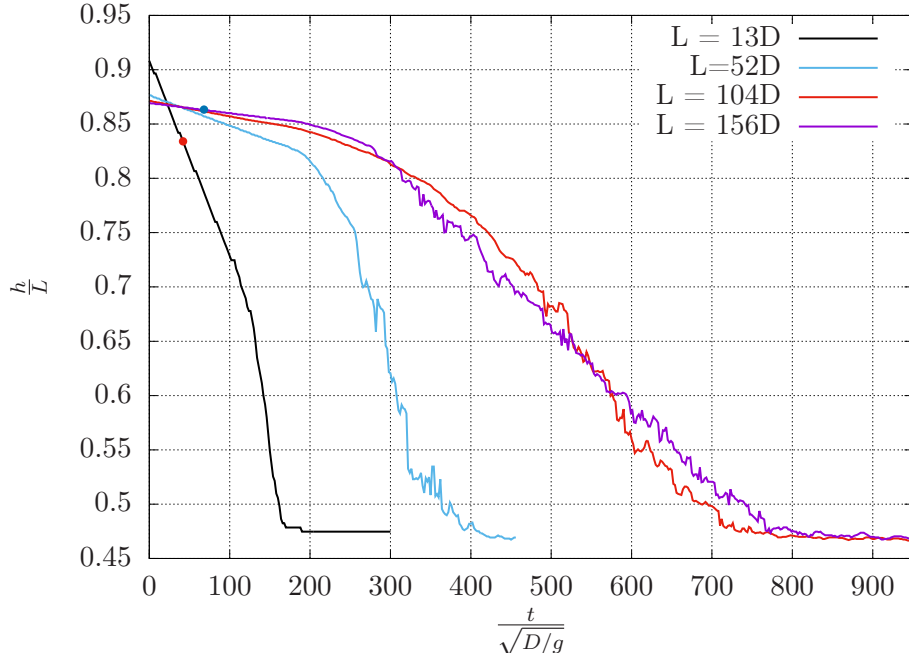


Figure 3.25: Trailing edge evolution for three different domains corresponding to $\frac{L}{D} = 13, 52, 156$. The numerical resolution is 20 to 25 points per drop.

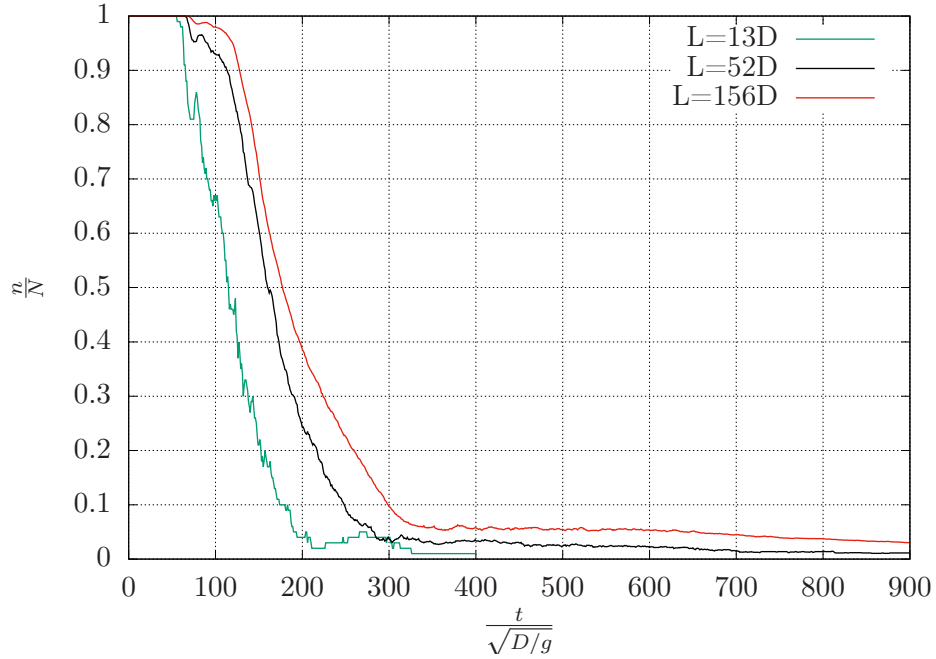


Figure 3.26: The number of drops evolution for three different domains $\frac{L}{D} = 13, 52, 156$. Numerical resolution is 20 to 25 points per drop.

So, the domain size seems not to have a huge impact on the coalescence frequency. Again, the transition between the coalescence stage and the separation stage is smoother for the large domain case than for the small domain case.

The coalescence frequency is observed to be not effected by the domain size. This is inline with the expectation that the coalescence frequency is not effected by the domain size due to: $\frac{l}{L} \ll 1$, where l denotes the distance between drops.

Drift y-velocity

As we increase the domain size we have observed the development of larger drops compared to the smaller domains. The presence of larger drops and filaments indicates that the drops settle with higher velocities and drops undergo large shear. Hence the relative average velocity between the two phases is expected to be higher as we increase the domain size. To confirm this guess, we look at the evolution of the drift y-velocity component (average relative y-velocity between two phases), defined as:

$$u_y^{drift} = \frac{\Sigma f u_y}{\Sigma f} - \frac{\Sigma(1-f)u_y}{\Sigma(1-f)} \quad (3.4)$$

Here we plot two curves showing the evolution of drift-y velocity corresponding to the two different length scales. One plot (Figure 3.27) with the drop diameter D , and corresponding velocity scale \sqrt{Dg} and the other plot (Figure 3.28) with the domain size L and corresponding velocity scale \sqrt{Lg} .

The drift y-velocity evolution for the three different domain sizes where the characteristic length scale is chosen to be the drop diameter D is shown in Figure 3.27. The mesh resolution for these test cases ranges between 20 to 25 points per drop diameter.

The positive direction of the co-ordinate y-axis in our simulation setup is upwards, whereas drops settle downwards, hence as drops settle down their phase velocity will be negative.

We can observe four different stages of evolution in Figure 3.27. Initially, the droplets are at rest and very quickly reach the terminal velocity during this settling stage. We can observe that the drift velocity remains constant (at about -0.03) for all the cases for about 150 time units.

Then a second stage starts where the curves decrease until they reach a maximum relative velocity between the two phases. We observe that the maximum drift velocity is different for each case; the larger the domain, the larger the drift velocity. In this stage, we observed in the qualitative section that coalescence is significant. This injects kinetic energy into the system due to the reduction of the surface energy, which in turn increases the relative velocity between these two phases. Eventually, the formation of very large drops will inject more kinetic energy into the system and so form filaments. Since larger domain promote the formation of larger drops and so larger kinetic energy, the drift velocity peak is larger for larger domains.

We then enter in the third stage corresponding to a deceleration of the drop phase with respect to the continuous phase. This eventually leads to the fourth stage where the phases are separated and the relative motion stops.

When we observe the graphs of the drift y-velocity plotted with two different scales as shown in Figure 3.27 and 3.28 we see that the curves using the characteristic length D appropriately scale the first stage whereas the last stages seem to be more

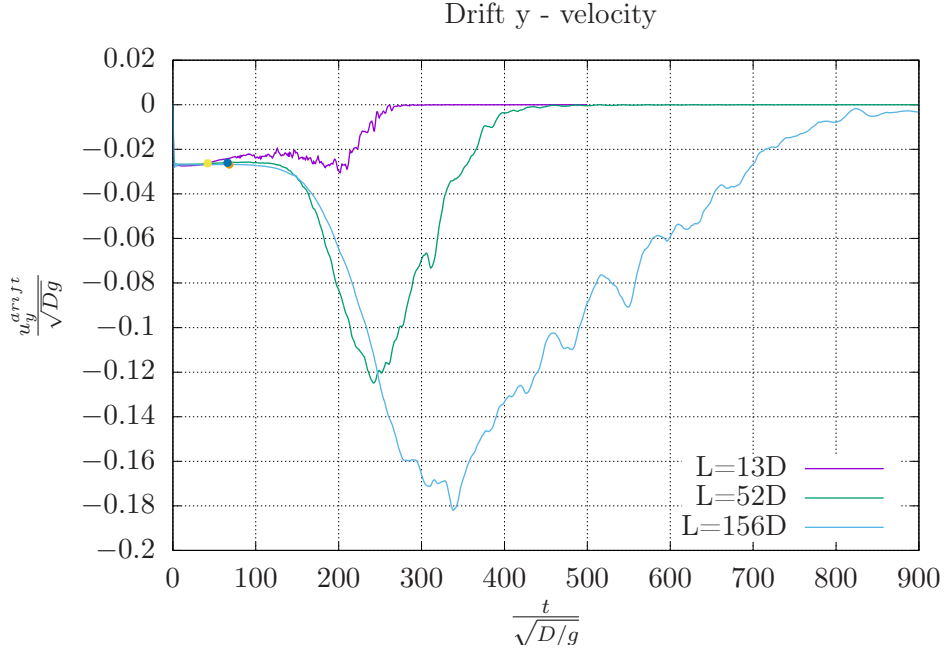


Figure 3.27: Drift y-velocity evolution of the three different domains $\frac{L}{D} = 13, 52, 156$. The characteristic length scale is chosen to be the droplet diameter D . Mesh resolution is 20 to 25 points per drop. The dots represents the first coalescence event.

consistently described when using the domain size L as a characteristic length. Hence we conclude that there exists a time where there is a transition between one length scale to the other.

3.3 Evolution of the non-coalescing emulsions

The non-coalescing emulsions using very few VOF tracers (thanks to the non-coalescence algorithm 2.4.3) is demonstrated in this section. Different stages have been distinguished in the evolution of a non-coalescing emulsions. They are analyzed both qualitatively and quantitatively.

The parameters corresponding to the simulations in this section are as follows:

Bo	Ar	ρ_r	μ_r	$\frac{L}{D}$	n	$\frac{D}{P}$
2.5	1.388	0.8	2	13, 52, 104	100, 1600 and 6400	20 - 40

Table 3.4: The simulation parameters corresponding to the non-coalescence simulations.

Qualitative analysis

At first a single case of $L = 52D$ (1600 drops) corresponding to Figure 3.29 and 3.30 has been analyzed qualitatively.

The evolution of the $\frac{L}{D} = 52$ non-coalescing emulsion has shown 4 distinct stages as shown in Figure 3.30:

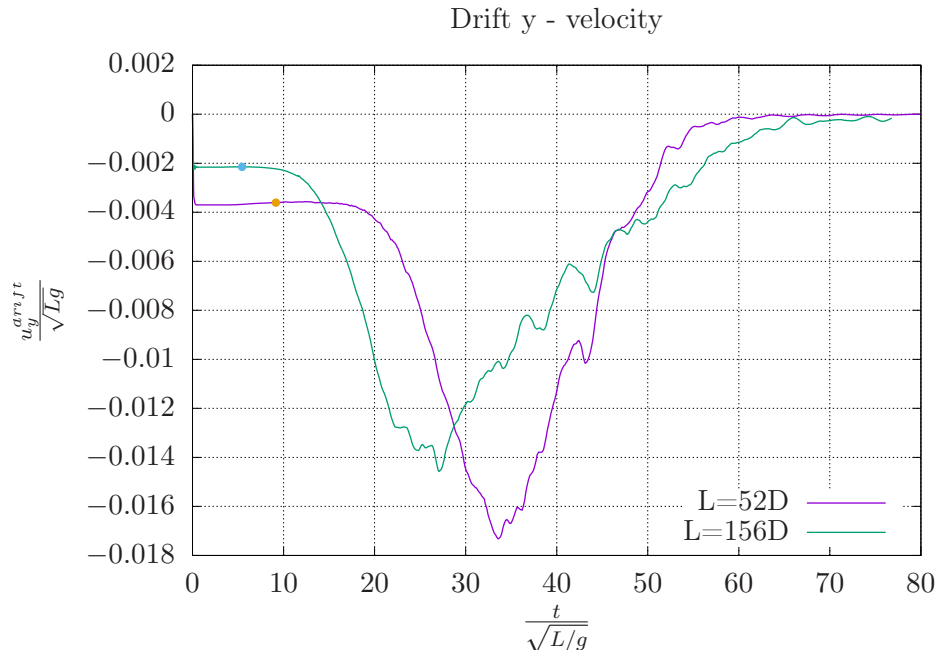


Figure 3.28: Drift y-velocity evolution for three different domains $\frac{L}{D} = 13, 52, 156$. The characteristic length scale is chosen to be the domain size L . Mesh resolution is 20 to 25 points per drop.

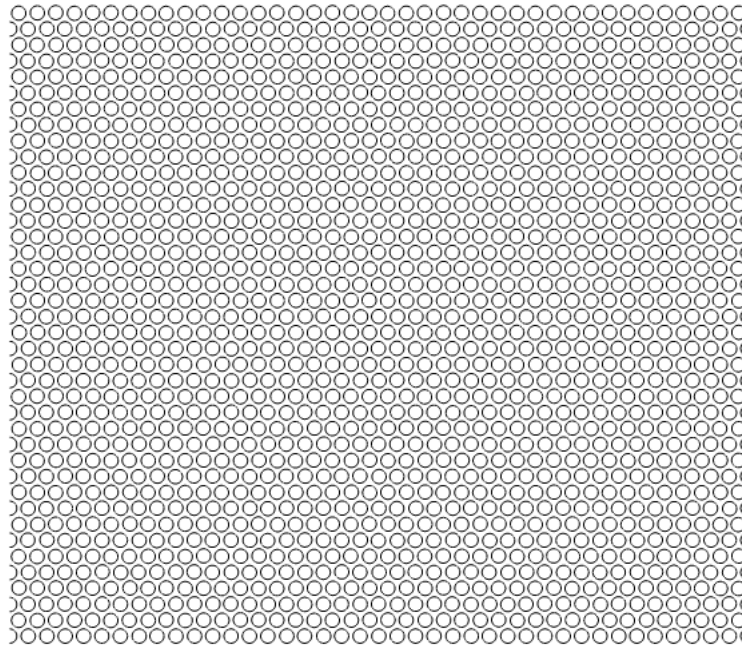


Figure 3.29: A 2D 52×52 two-phase flow domain with $\frac{L}{D} = 52$.

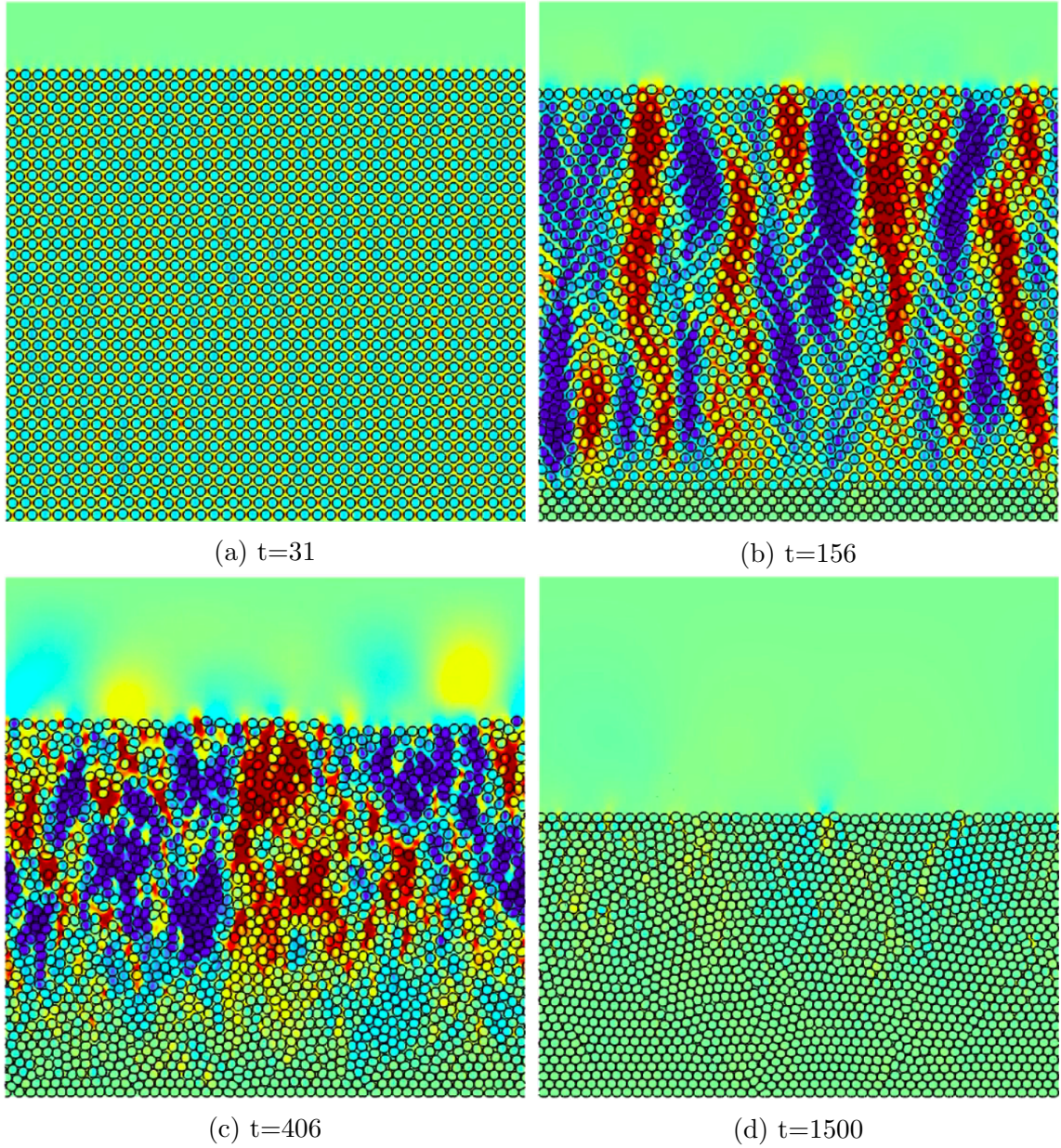


Figure 3.30: Evolution of a $\frac{L}{D} = 52$ non-coalescing emulsion at the different simulation times corresponding to the different stages. Both phases are colored with the magnitude of the y-velocity ranging from $[-0.1 : 0.1]U$ (blue to red).

Settling stage

In this stage the drops start from rest and start to settle down under the influence of gravity with minute deformations. The flow field does not show any instabilities or other characteristic features. The sub-figure 3.30a at simulation time $t = 31$ corresponds to this settling stage. By this time the bottom layer of the drops have reached the bottom boundary.

Intermediate stage

As drops start to settle down, a layer of already settled down droplets at the bottom boundary is shown in sub-figure 3.31b corresponding to simulation time $t = 156$. An instability then appears and forms alternating vertical channels. This is observed through the y-velocity field.

Later stage

As more and more of the drops settle down, the vertical channels start to shorten in the y-direction and diffuse in the x-direction. This is observed in sub-figure 3.32b.

Settled stage

As drops settle down further the strength of the velocity field is reduced and it is also observed that the drops move in layers sliding past each other (like a Couette flow in appearance). Then comes a time when the drops have completely settled down as shown in Figure 3.33b.

3.3.1 Effect of the domain size

The effect of the domain size on non-coalescing emulsions is qualitatively analyzed for three different cases ($\frac{L}{D} = 13, 52, 104$). The simulation snapshots consisting of the drops interface and the y-velocity field are compared for these three cases at different simulation times, where each time corresponds to the different stages of a non-coalescing emulsion.

Settling stage

In the initial settling stage, drops in all of the three different domain size settle similarly without showing any instabilities.

Intermediate stage

As the drops start to settle down the vertical channels start to appear in large-size domains as observed in Figure 3.31 at simulation time $t = 156$.

The $\frac{L}{D} = 13$ case does not show any instability forming vertical channels. The $\frac{L}{D} = 52$ & 104 cases show similar patterns (vertical channels). The height of the vertical channels observed from sub-figure 3.31c corresponding to the $\frac{L}{D} = 104$ is longer than that of the $\frac{L}{D} = 52$ shown in sub-figure 3.31b. Whereas the width of the patterns appears to be same. This instability increases the total settling time of

the drops due to the upward motion of the drops present in the red colored regions (upward velocity).

The smaller domains does not display instability and the larger domains capture the vertical channels of larger height.

Later stage

As the drops further settle down, the vertical channels start to disappear as observed from Figure 3.32 corresponding to simulation time $t = 406$.

At this stage, the $\frac{L}{D} = 13$ case looks similar to the bottom region of the other two large domains. Similarly the $\frac{L}{D} = 52$ domain is expected to be same as that of the bottom region of the $\frac{L}{D} = 104$.

The bottom boundary effects are seen by drops in shorter time scales compared to the larger domains which is seen in Figure 3.32.

Settled stage

The drops ultimately settle down completely. During this stage, in the large domain case it is observed that the drops settle down while sliding past each other in layers, somewhat similarly to what happens for emulsions in a Couette flow. The settled drops (still moving slightly in the x-direction) are shown in Figure 3.33.

It can be concluded that the $\frac{L}{D} = 52$ domain qualitatively behaves similarly to the $\frac{L}{D} = 104$ case. The height of the vertical channels and the magnitude of the y-velocity increase with the domain size.

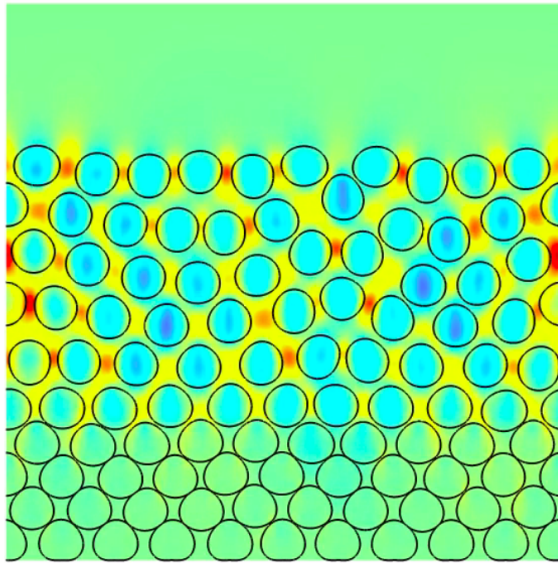
Computational cost

The non-coalescing functions employed for the simulations use very few VOF functions to avoid the coalescence. As a consequence (combined with the efficient methods for the other governing equations) it is computationally inexpensive compared to other existing non-coalescing VOF methods (where the number of VOF functions is equal to the number of drops). It is interesting to show the computational performance of non-coalescing function both in terms of the computation cost and the number of VOF functions used (though they are dependent on one another).

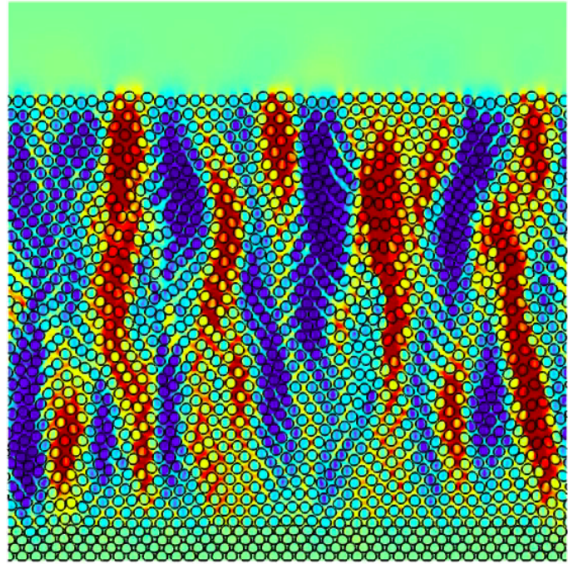
The most expensive part of the non-coalescing function is the tag function 2.3, whose computational cost scales as that of the Poisson solver. The computational time of the simulations along with the number of VOF tracers used is given in Table 3.5.

Number of drops	$\frac{D}{P}$	Number of cores	Simulation time	Computational time (CPU hours)	Number of VOF tracers
100	40	16	500	2.8	6
1600	40	144	1500	27	7
6400	20	144	1500	26	15

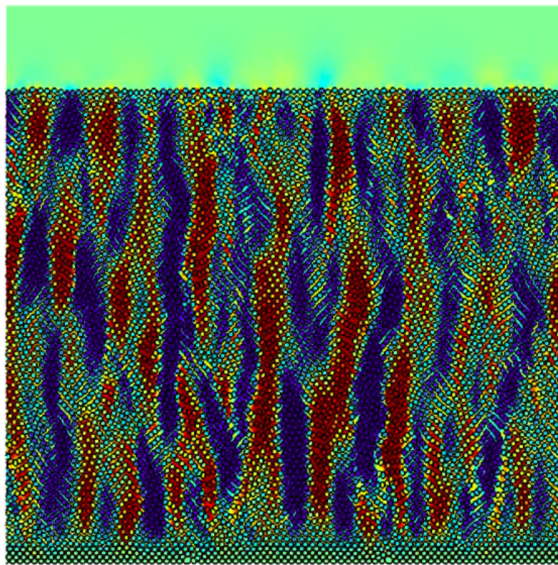
Table 3.5: Computational cost and number of VOF tracer for the non-coalescence simulations.



(a) $\frac{L}{D} = 13$

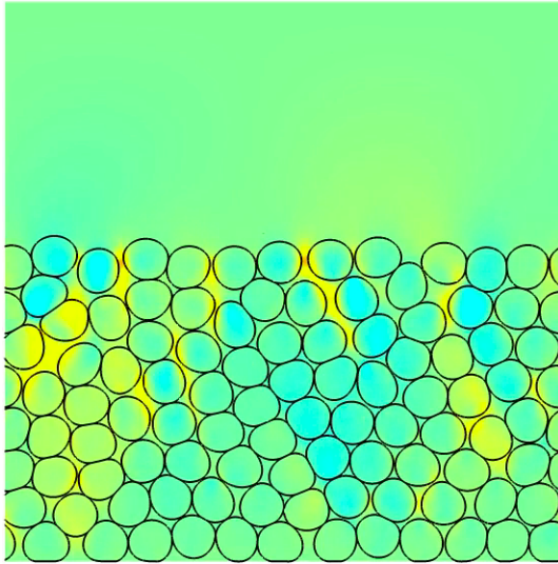


(b) $\frac{L}{D} = 52$

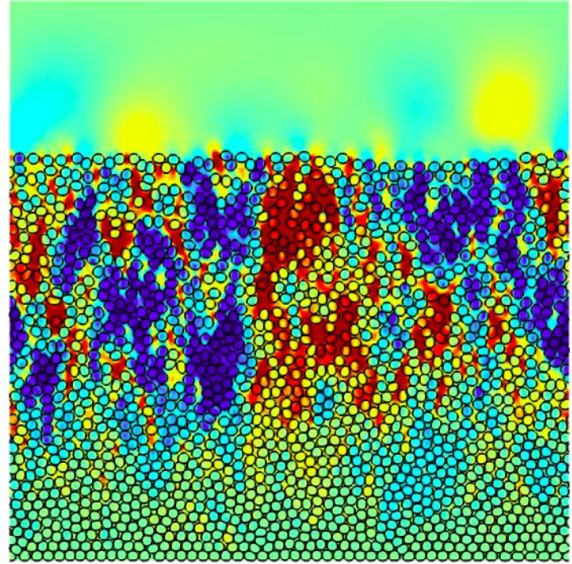


(c) $\frac{L}{D} = 104$

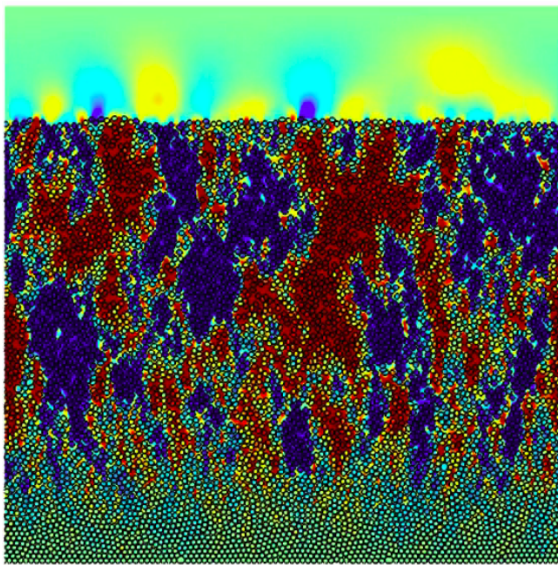
Figure 3.31: Non-coalescing emulsion corresponding to the three different domains at simulation time $t = 156$.



(a) $\frac{L}{D} = 13$

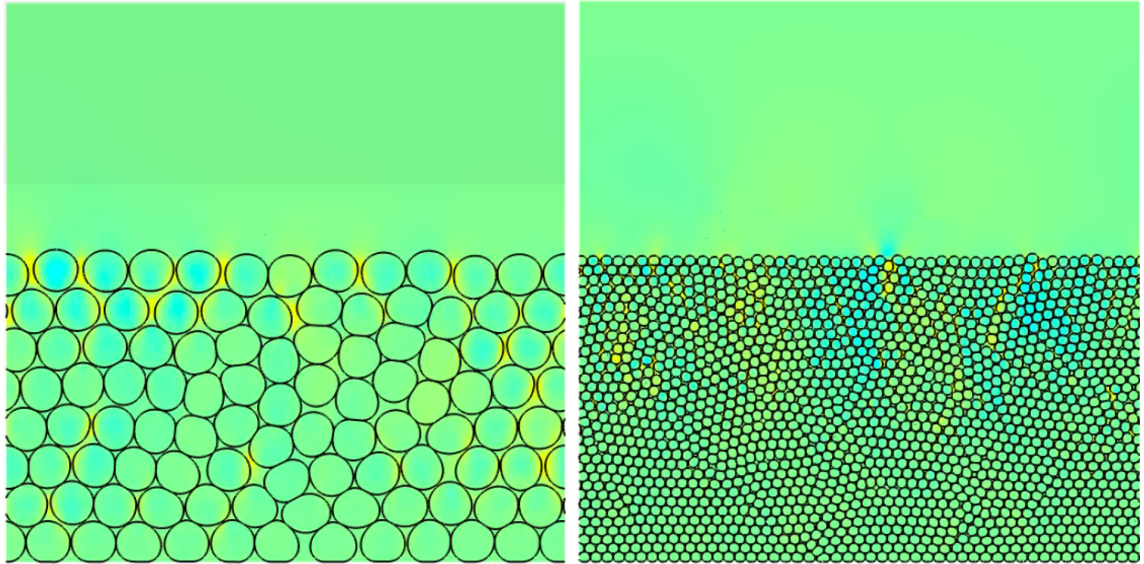


(b) $\frac{L}{D} = 52$



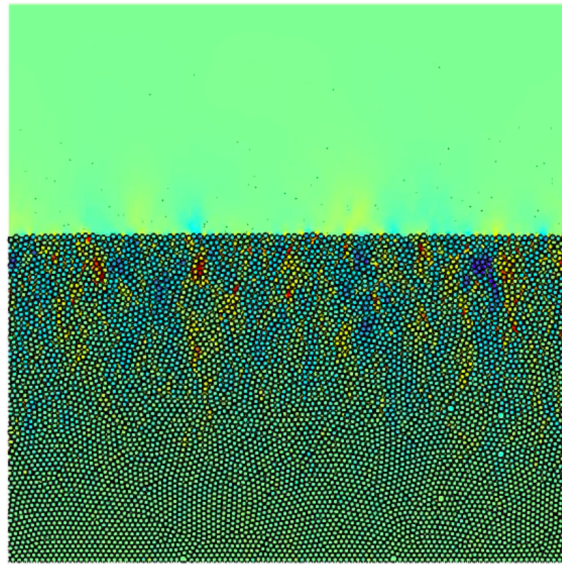
(c) $\frac{L}{D} = 104$

Figure 3.32: Non-coalescing emulsion corresponding to the three different domains at simulation time $t = 406$.



(a) $\frac{L}{D} = 13$

(b) $\frac{L}{D} = 52$



(c) $\frac{L}{D} = 104$

Figure 3.33: Non-coalescing emulsion corresponding to the two different domains ($\frac{L}{D} = 52$ & 104) at simulation time $t = 1500$ and a $\frac{L}{D} = 13$ simulation at time $t = 500$.

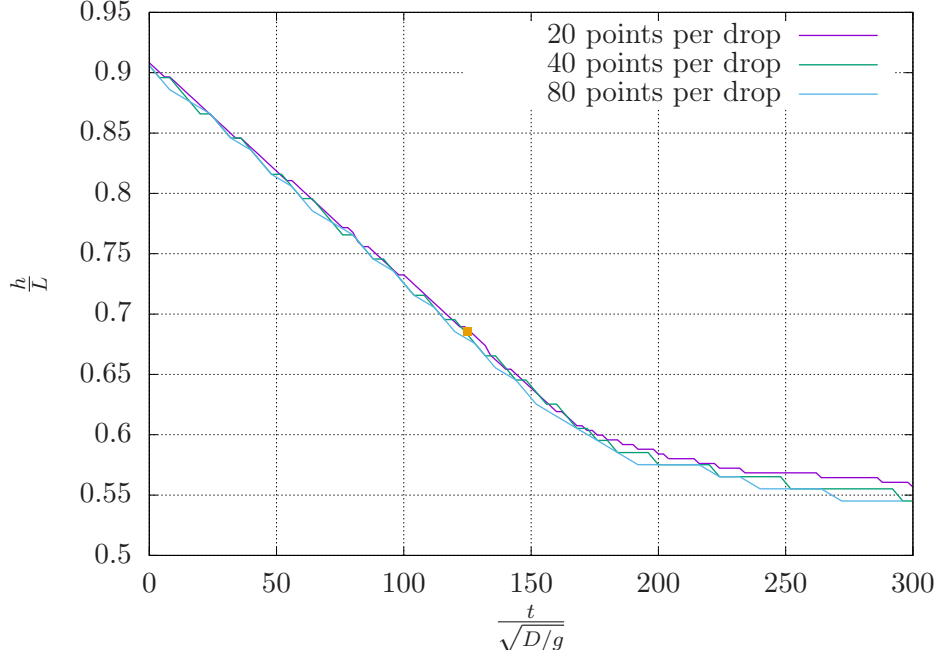


Figure 3.34: The evolution of the trailing edge of a $\frac{L}{D} = 13$ non-coalescing emulsion for three different resolutions.

In Table 3.5 we can see that a small number of VOF tracers are able to represent a large number of drops. The coalescing emulsion of $\frac{L}{D} = 13$ with a mesh resolution of 40 points per drop took 1.2 CPU hours compared to 2.8 CPU hours of the non-coalescence simulation at the same numerical resolution and ran for the same amount of time.

Quantitative analysis

3.3.2 Effect of the resolution

We expect a minimal effect due to a change in the resolution beyond 20 points per drop as there is no coalescence and the flow regime is a low to moderate Reynolds/Archimedes number.

The figure 3.34 shows the evolution of the trailing edge for the three different mesh resolutions: 20, 40 and 80 points per drop diameter. In all the stages of the evolution no significant difference between these three cases is observed.

From this, one can conclude that the 20 points per drop are sufficient to capture the trailing edge in a non-coalescing emulsion. This also re-assures that 20 points are sufficient to resolve the hydrodynamic forces around the drop.

Separation front

The trailing edge evolution of the non-coalescing emulsions for three different domain sizes are plotted in Figure 3.35.

The two large domain cases show the three stages of the evolution of the trailing edge. In the first stage, the position evolves with a constant slope until around $t = 200$. The displacement then accelerates and reaches an inflexion point, which is

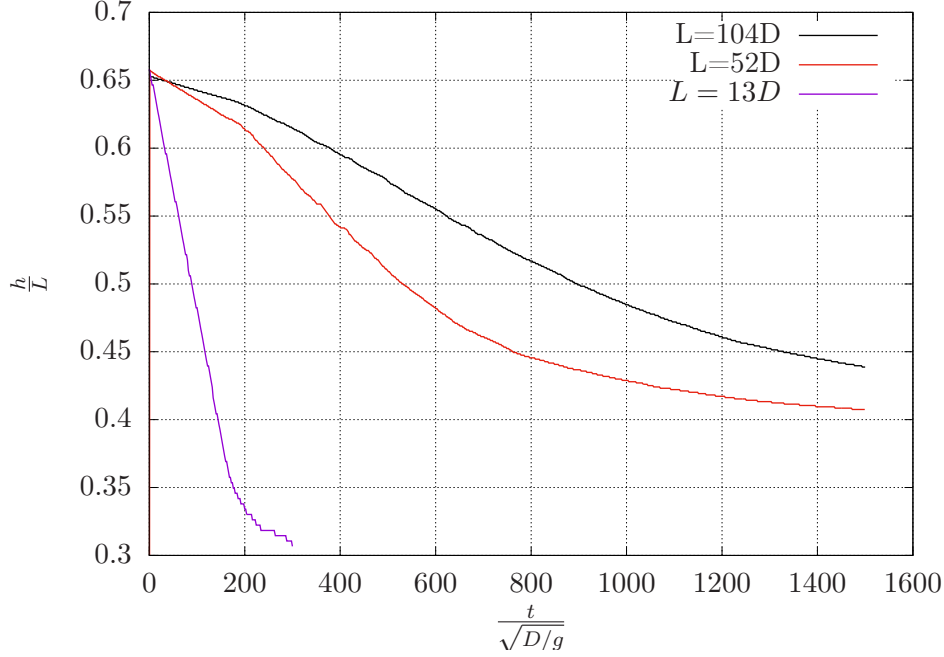


Figure 3.35: The evolution of the trailing edge of the non-coalescing emulsions corresponding to three different domain sizes. Where $\frac{L}{D} = 13$ & 52 are resolved by 40 points per diameter and $\frac{L}{D} = 104$ by 20 points per diameter. The trailing edge corresponding to the $\frac{L}{D} = 13$ has been shifted vertically down to match the initial points of the $\frac{L}{D} = 52$ & 156 cases.

between $t = 600 - 1000$ for both of the domains. The displacement then decelerates until complete settling.

The $\frac{L}{D} = 13$ case also displays the three different stages of evolution: constant slope, acceleration and deceleration. But most of the curve evolve with constant slope unlike the other two cases.

The slope at the inflection point for the $\frac{L}{D} = 52$ & 104 cases look similar, whereas the $\frac{L}{D} = 13$ case differs significantly.

It can be concluded that the $\frac{L}{D} = 52$ domain is qualitatively similar for the evolution of the trailing edge. This domain size is sufficient to qualitatively represent the trailing edge evolution of a large emulsion.

3.4 Evolution of the controlled-coalescing emulsions

A multiphase flow simulation using VOF methods with a single VOF tracer always coalesce multiple interfaces at the order of the mesh size. Hence this numerical coalescence is controlled by the mesh size. In this section, we present results of emulsion evolution using the controlled coalescence algorithm detailed in Chapter 2.

We are interested in a liquid/liquid emulsion at a moderate Reynolds number and slightly deformable drops. From the literature study, I could not find any work on controlled-coalescence emulsion simulations of such regime by solving the full

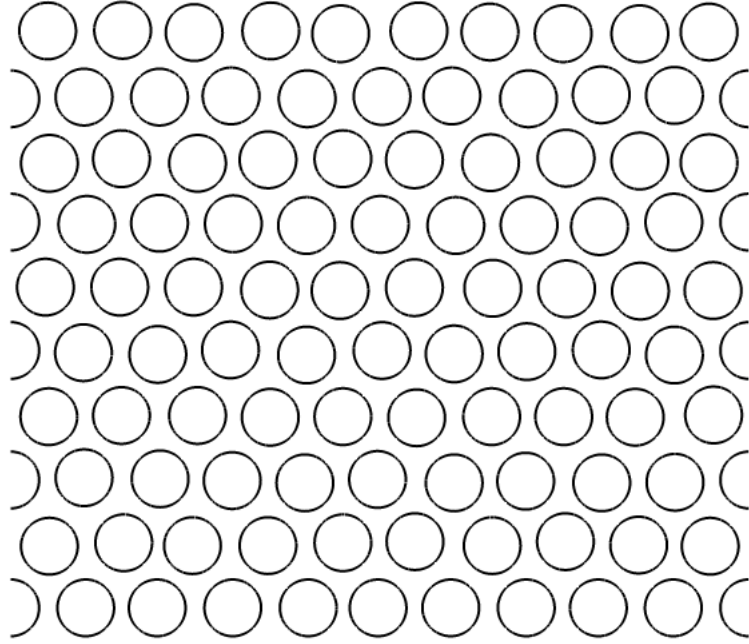


Figure 3.36: A 2D 13×13 domain of $\frac{L}{D} = 13$.

Navier-stokes equations.

The behaviour of an emulsion using the control coalescence algorithm is studied via three simulations, where the drainage time is varied. The primary control parameter in these simulations is the contact time (how long multiple interfaces can stay between one to two cells away from each other), which we refer to as the drainage time.

In reality, the drainage time for two given drops depends upon a variety of factors such as the local curvature of the interface, viscosity, density, diameter, surface tension coefficient, etc... The drainage time can be computed by using additional models under certain assumptions and using several parameters as input. It is then possible to couple these additional models to our control coalescence model. Nevertheless, for simplicity and to demonstrate the ability of such a model to control coalescence, we choose as a starting point to set the same contact time for all of the approaching pairs of drops.

In our simulations in the absence of impurities, neutrally charged drops, and constant temperature, film drainage is governed by the competition between the capillary force, viscous force, and buoyancy. Combination of these three forces gives a time scale $t_{film} = \frac{\mu_c}{\sqrt{\rho_c \sigma g}}$. For our simulation this value is $\frac{1}{\sqrt{10}}$. Hence the contact time to control the coalescence are chosen to be 0.1, 1, and 5, which are around $\frac{1}{\sqrt{10}}$ and one order more.

The purpose of this section is to demonstrate the delay in coalescence by varying the drainage time rather than resolving the film drainage scales accurately using a finer mesh. The test case is a 2D domain of $\frac{L}{D} = 13$ as shown in Figure 3.36 with a numerical resolution of 20 points per diameter. The parameters corresponding to

the test case are given in Table 3.6.

Bo	Ar	ρ_r	μ_r	$\frac{L}{D}$	n	$\frac{D}{P}$	Contact time
2.5	1.388	0.8	2	13	100	20	0.1, 1 and 5

Table 3.6: Simulation parameters corresponding to $\frac{L}{D} = 13$ control coalescence test case.

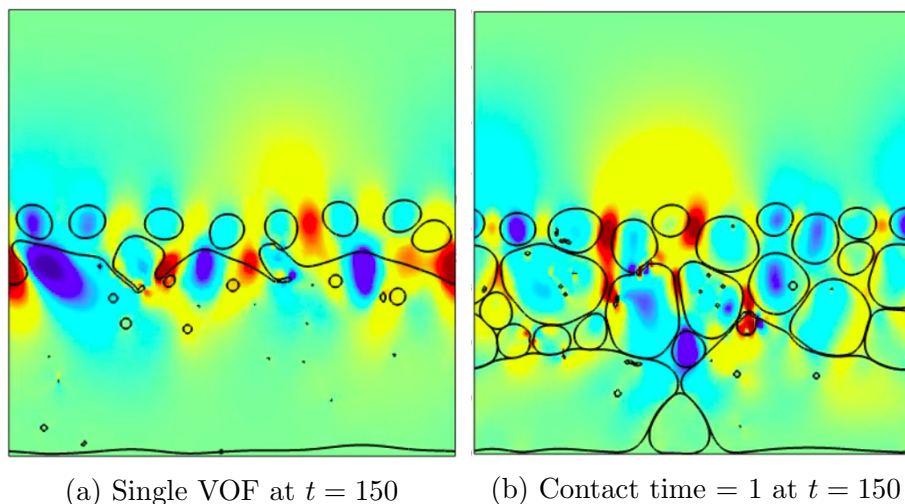


Figure 3.37: A 2D domain of $\frac{L}{D} = 13$ with numerical resolution of 20 points per diameter at simulation time $t = 150$. Both phases are colored with the magnitude of the y-velocity ranging from $[-0.1 : 0.1]U$ (blue to red).

In Figure 3.37, we compare the emulsion behaviour after time $t = 150$, when the contact time is increased. We clearly see the impact of the contact time on the coalescence process, since the larger the contact time, the larger the number of droplets. So, the controlled coalescence algorithm coupled with a simple drainage time model is able to delay the numerical coalescence, observed in a classical VOF method (using a single VOF tracer).

3.4.1 Effect of the drainage time

Separation front

The trailing edge evolution for the three different test cases with the three different contact times is shown in Figure 3.38, where the first coalescence event is identified using a color dot. We evidence here that a larger drainage time will increasingly delay the first coalescence event. However, the first stage of the time evolution of the trailing edge seems not to be sensitive to the contact time, since all the curves are superimposed until time $t = 100$. Indeed, during this first stage, most of the droplets are settling and only a few are coalescing, explaining the low impact of the drainage time on the global behaviour of the emulsion.

After $t = 100$ until $t = 200$ the trailing edge curves start to differ for different drainage times, where the settling velocity of the trailing edge increases until some

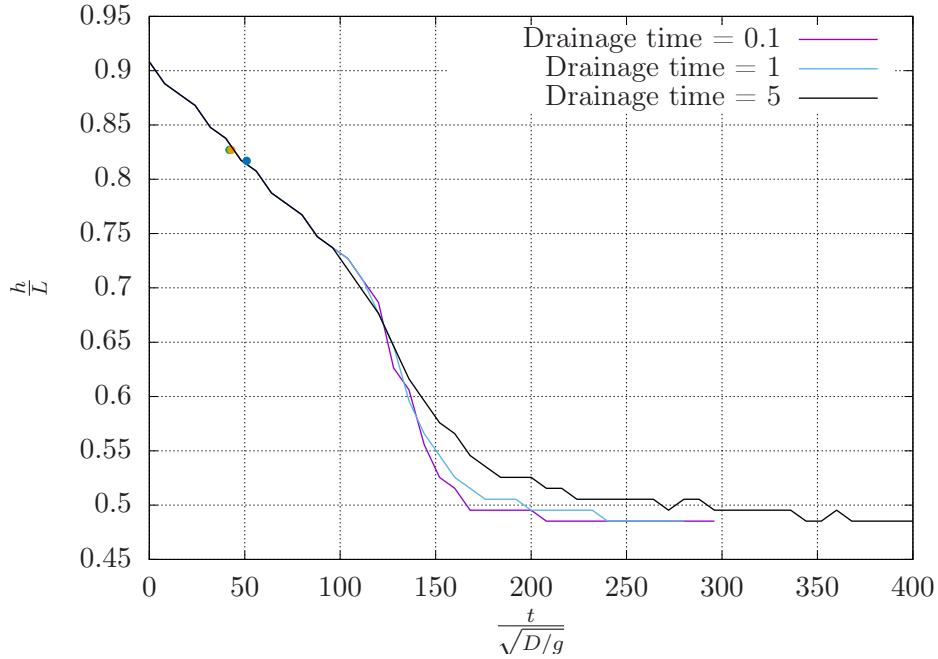


Figure 3.38: Trailing edge evolution for three different controlled coalescence test cases corresponding to the drainage time 0.1, 1, and 5. The colored dots correspond to the first coalescence. The red square at $t = 150$ corresponds to the Figure 3.37b.

point, then starts to decrease showing an inflection point. In this third stage, the coalescence process is significant and so is impacted by the contact time. Indeed, the larger the drainage time, the larger the delay of the separation. This third stage spans much longer for the test with drainage time $t = 5$ which shows the delay in the evolution of the separation front due to the delay in coalescence.

Later on in the fourth stage, drops coalesce and the two phases separate.

The increase in drainage time delays the coalescence, which will impact the evolution of the trailing edge at later stages. The total settling time is increased as observed in Figure 3.38.

Coalescence frequency

The evolution of the number of drops with the three controlled coalescence simulations with drainage times 0.1, 1 and 5 is plotted in Figure 3.39.

Initially, the number of drops is 100, until $t = 45$ there is no coalescence. This corresponds to the pure settling stage. Between $t = 45 - 50$ the first coalescence appears in all of the cases. From this point, the drops start to coalesce and the coalescence frequency (the slope of the curves) starts to increase for the three cases. As can be observed in Figure 3.39, the smaller the drainage time, the greater the coalescence rate.

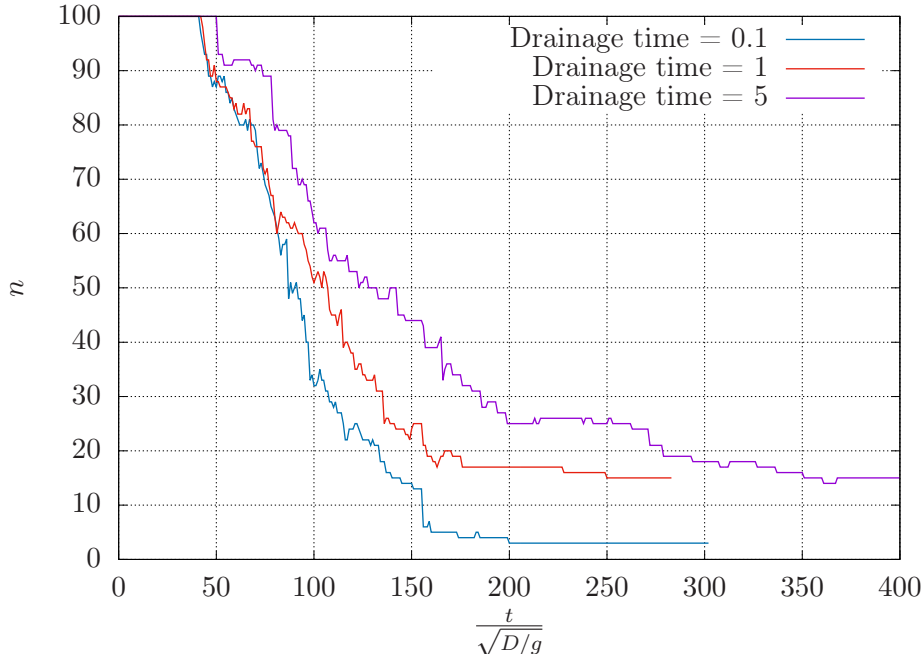


Figure 3.39: Evolution of the number of drops for three different controlled coalescence test cases corresponding to the drainage times 0.1, 1 and 5

3.5 Impact of the coalescence model on the behaviour of a 100 droplets emulsion

The evolution of the coalescing, non-coalescing and controlled-coalescing emulsions are discussed individually. In this section they will be compared to each other, which will show the effect of the newly introduced functions to avoid and control the coalescence.

3.5.1 Separation front

In coalescing emulsions using a single VOF, the coalescence is delayed using a finer mesh. This will delay the settling time, which eventually delays the evolution of multiple stages as observed in Figure 3.40. Here the trailing edge represented by the green circled points (corresponding to the coalescing emulsion of the $\frac{L}{D} = 13$ with a numerical resolution of the 20 points per dia.) has reached the settling stage quickly compared to that of the black-dotted trailing edge corresponding to the 80 points per diameter resolution. This demonstrates the delay in coalescence due to the mesh refinement.

The trailing edge of the non-coalescing emulsion (resolution of 20 points per drop) coincides with the coalescing emulsion with 80 points per drop until around $t = 200$.

In the initial settling stage, where the coalescence process is limited, neither the mesh size nor the coalescence model have any impact on the position of the trailing edge. This can be observed from Figure 3.40 until $t = 120$.

We have two extreme limits, the coalescing emulsion with 20 points per drop as a *lower limit* and the non-coalescing emulsion as an upper limit. Using the controlled

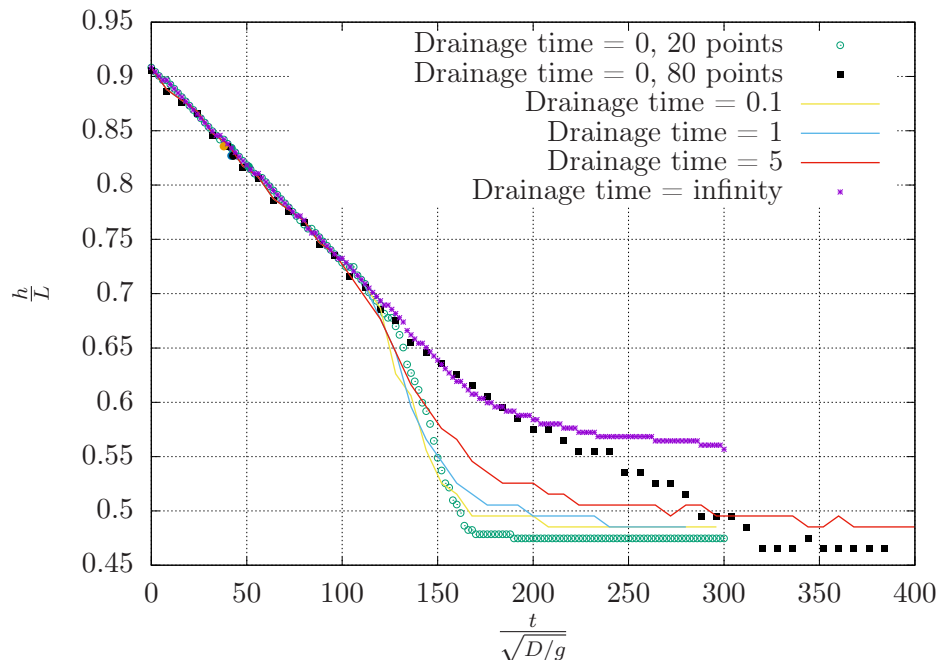


Figure 3.40: The trailing edge evolution of a 2D emulsion for the coalescing, the non-coalescing and the controlled coalescing model. The coalescing emulsions are shown in green circles and black squares, the non-coalescing emulsion is shown in purple squares and the controlled-coalescing emulsions are shown by three different colored lines with the corresponding drainage time. The numerical resolution of the controlled-coalescing emulsion is 20 points per diameter.

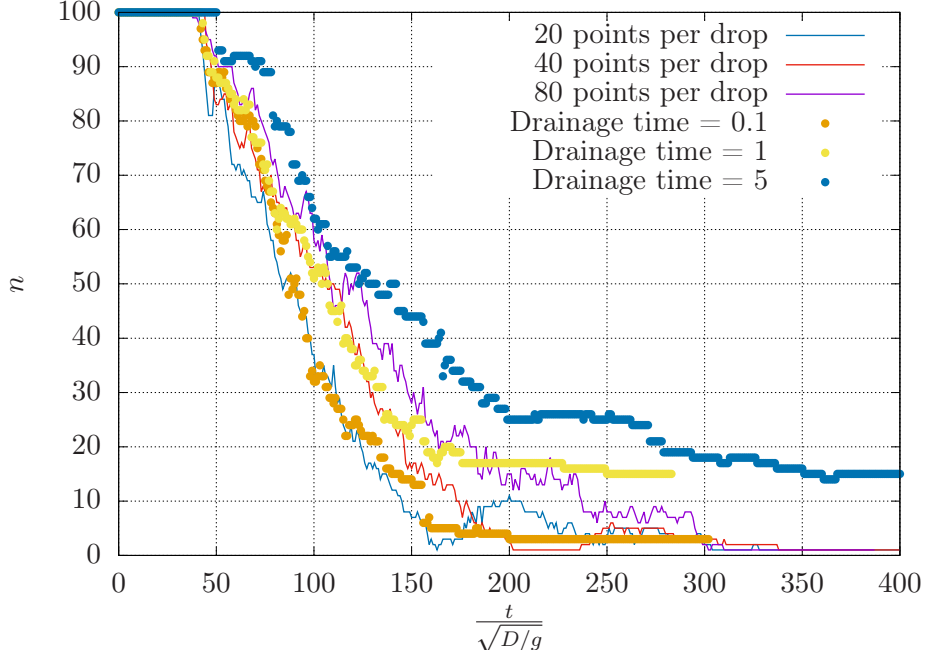


Figure 3.41: The number of drops evolution of a 2D $\frac{L}{D} = 13$ emulsion for the coalescing and controlled-coalescing emulsions. The coalescing emulsions are shown with different colored lines along with their numerical resolution. The controlled-coalescing emulsions are shown with colored dots with their drainage time. Their numerical resolution is 20 points per diameter.

coalescence model with the drainage time values 0.1, 1 and 5 and a coarse mesh (20 points per drop), the trailing edge evolution is delayed and shifts from the lower limit towards the upper limit as shown in Figure 3.40. Finally, the controlled coalescence model can be used to control the settling time of the emulsion.

3.5.2 Coalescence frequency

The rate of coalescence can be reduced by using finer meshes. This can be observed from Figure 3.41. Using the control-coalescence function and varying the drainage time the coalescence frequency is reduced as observed from Figure 3.41.

The coalescing emulsion with 20 points per diameter evolves similarly to that of the controlled-coalescing emulsion with a drainage time of 0.1. The yellow dots corresponding to a drainage time of 1 closely match the coalescing one with 40 points per diameter until $t = 140$, beyond which the number of drops evolve much more slowly than for the coalescence case with 80 points per diameter.

For the case of a drainage time of 5, the evolution of the number of drops is further delayed and always ahead of the (much more delayed coalescence) with 80 points per diameter.

Figure 3.41 has clearly demonstrated the delay of the evolution of the number of drops when using the controlled coalescence model and varying the drainage time.

Conclusion and perspectives

Numerical investigation of the two limiting cases (numerically coalescing and non-coalescing) and an intermediate case (controlled coalescing) of a buoyancy-driven emulsion (Liquid/Liquid) using a Volume-of-Fluid (VOF) method is performed in this thesis. The regime of these emulsions corresponds to slightly deformable drops ($Bo = O(1)$) and moderate Reynolds/Archimedes number ($Ar = O(1)$). There are two main parts in this study: the demonstration of a non-coalescing and a control coalescing emulsion using new numerical methods and the analysis of the physics and dynamics of the resulting emulsions. In both the coalescing and non-coalescing emulsions an instability appeared (at the stage with limited coalescence) as alternating vertical channels of the vertical velocity field component. During the evolution of a coalescing emulsion, two different length scales: the drop diameter and the domain size appeared to characterize the different stages of evolution, with a clear transition between these two characteristic scales. In large domains of a coalescing emulsion, filaments are observed due to the formation of large drops (preceding significant coalescence) and corresponding large velocity gradients. The stage leading to an instability is characterised by the drop diameter and that of the filaments is characterized by the domain size with a clear transition from one to the other. The appearance of an instability and the formation of filaments is not observed in the smaller domain size.

In an emulsion when the drops approach each other, the surrounding fluid forms a thin film which drains under the action of hydrodynamic, capillary and colloidal forces. The competition between these forces decides the timescale of the film drainage. Longer timescales prevent coalescence thus leading to a stable emulsion. A way to simulate emulsions is to solve numerically the Navier-Stokes equations using a single VOF tracer to describe multiple drops. This will always allow coalescence at the order of the mesh size (numerical coalescence) leading to incorrect timescales and length scales of the film drainage. Additional models (such as a disjoining pressure model) may moreover be necessary to capture this thin film drainage and eventual rupture accurately since they are not normally present in the continuum Navier-Stokes equations. The slow-draining thin film between two drops can be of order $O(\mu m - nm)$ and using VOF needs a mesh size of the same order to avoid numerical coalescence. This makes it impossible to accurately simulate an emulsion consisting of a large number of drops using single VOF tracer advection (with current computational resources).

Coyagee et al [41] used different VOF tracers for different drops to entirely avoid coalescence. Emulsion simulations using VOF or other methods thus have two limiting cases, one that always allows coalescence at the mesh size and the other that always avoids the coalescence. Of course, real emulsions lie between these two limiting cases. Existing solutions to achieve this intermediate stage are of two types: one

way is to couple an additional model to a single VOF advection [48], the other way is to use multiple marker functions (multiple VOF tracers) coupled with an additional model (tested only for binary coalescence) [49]. In the first case (single VOF), very fine meshes maybe necessary, while in the other case as many VOF tracers as drops are needed. These two solutions are thus very computationally expensive for large emulsions.

In this thesis, I showed that simulating a non-coalescing emulsion can be done with much fewer VOF tracers than drops. Indeed, different VOF tracers are only required for closely neighboring drops. The problem to solve is thus similar to a graph-coloring problem or color mapping of the regions of a map so that no two regions sharing a common boundary has the same color. The famous four-color theorem states that a maximum of four colors are sufficient to achieve this color mapping [50]. Our problem is a variant of a graph-coloring problem. Though we may need more than four VOF tracers, the total number of VOF tracers necessary are much less than the total number of drops. In the case of a coloring of drops in an emulsion, it is a time-varying graph-coloring problem due to the possibility of relocation of drops over time. I have showed how this problem can be solved efficiently. This has lead to a very efficient and computationally inexpensive multiple-marker method allowing to entirely avoid coalescence.

I have also proposed an extension of these algorithms which allows to control the duration during which droplets can interact before coalescing. This opens the door to controlling the coalescence timescale through additional subgrid-scale modelling of coalescence.

In the last part of the thesis, results of the different analysis are discussed. The analysis of a large (numerically) coalescing emulsion has revealed qualitatively different stages: settling, instability, coalescence, filaments and separated stage. In the second stage, instabilities in the form of alternating vertical patterns are observed. The wavelength of this instability is found to be between 4 to 8 droplet diameters and is found to be independent of the domain size when the domain size is not too small. In the next stage, significant coalescence leads to the formation of filaments. This is due to the formation of large drops, which settle at higher velocity leading to higher shear of drops compared to the surface tension (higher capillary number). A quantitative analysis is then performed by computing the top phase front (leading edge) and the number of drops evolution. The quantitative and qualitative analysis have shown that there exists two characteristic scales (drop diameter and domain size) each characterizing the different stages of an emulsion, where the drop diameter characterized the instability stage and the domain size characterized the filament stage. These two characteristic scales make a transition from one to another between these two stages. Among the different domain sizes tested ($L = 13D, 52D, 104D$ and $156D$), we found that a domain size of $52D$ is sufficient to qualitatively represent all the stages of evolution of a large emulsion.

I have repeated this analysis for the other limiting case, that of a non-coalescing emulsion, and found similar stages. The instability stage is in particular similar and is also found to be independent of the domain size, for a large enough domain. In contrast with coalescing emulsions, quantitative analysis have shown no effect of the numerical resolution on the domain $13D$. This is due to the non coalescence and the minimum resolution used (20 points per drop) which is sufficient to fully resolve the flow. Among the different domain sizes tested ($L = 13D, 52D$ and $104D$), we found

that the domain size of 52D is sufficient to qualitatively represent a large emulsion. The smallest domain (13D) tested has not shown any instabilities.

Finally I have demonstrated how the coalescence time could be controlled, using a simple constant time delay, and that the results were consistent with the two limiting cases described previously.

The developments and analysis in this thesis have opened the door for a large number of future improvements and research directions. The control coalescence subgrid model can now be explored, taking into account the macroscopic parameters such as the drops relative velocity, viscosity, surface tension etc. It will also be interesting to know if the patterns observed in our simulations corresponds to any existing instabilities such as Rayleigh-Taylor instability etc. by checking the dispersion relation (quantification) obtained using the velocity field. We could also investigate if similar patterns and regimes are observed in porous media and granular media.

For computational efficiency and as a first step, the results presented in this thesis are in two dimensions, however the algorithms developed also work in three dimensions. There are a few remaining technical issues, dealing with parallelization and the efficient tracking of the identity of individual droplets, which need to be sorted out. Once this is done, the study of three-dimensional emulsions and their qualitative and quantitative comparison with the 2D results presented here, will also be very interesting and relevant to practical applications. In particular, 3D simulations will give the opportunity to compare and validate our numerical approach with experimental results (bottle test for instance).

It is also worth noting that recently Karanakov et al [44] (using VOF) and Rajkotwala et al [43] (using the Local Front Reconstruction Method) have presented some interesting developments towards avoiding and controlling coalescence. Comparison of their methods and results would also be interesting.

The control coalescence function needs to be coupled to a film drainage model (both experimental and theoretical) to evaluate the effect of this model on the global evolution of an emulsion and also to compare to the existing numerical and experimental results. This model could include subgrid hydrodynamic and capillary forces during film drainage or additional colloidal forces, as well as the variation of surface tension coefficient due the presence of surfactants and temperature, to estimate a drainage time linked to the macroscopic parameters resolved numerically. This would lead to a complete and efficient numerical model of emulsions, directly applicable to a broad range of practical problems.

List of Figures

1	Vinaigrette emulsion, reproduced from [1].	5
2	Oil platform, reproduced from [7].	7
3	Schematic representation of the separator unit and other important length scales in the system. Reproduced from [9].	8
4	Schematic diagram of the different stages of a coalescence. Reproduced from [10].	8
5	Schematic diagram of the multiscale and multiphysics nature of an emulsion.	9
6	Schematic diagram of the multiscale nature of an emulsion.	10
1.1	The microscale of a water/oil emulsion. Reproduced from [12].	12
1.2	Schematic diagram of the emulsion breakdown process. Reproduced from [13].	13
1.3	Various breakup mechanisms of a drop, reproduced from [14].	14
1.4	Schematic representing the different stages of a collision of a pair of approaching drops, leading to either coalescence, agglomeration or repulsion. Reproduced from [9].	15
1.5	Summary of the relative velocities of a pair of drops in different flow regimes, reproduced from [9].	16
1.6	The approach and the film drainage of two different sized drops d_1 and d_2 , where $h(r, t)$ is the film thickness and $s(t)$ is the distance between the center of mass of two drops. Reproduced from [9].	16
1.7	The film profile evolution for the glycerol drops dispersed in a silicon oil. The fringe patterns obtained through optical inference of experiments and theoretical results are compared at 27s. Reproduced from [16].	17
1.8	Schematic representation of the various possible thin film shapes. Reproduced from [9].	17
1.9	The experimental images of the film rupture evolution of toluene drops in water. Reproduced from [9].	19
1.10	Representation of the surface tension variation with surfactant concentration, reproduced from [22].	19
1.11	Minimal film thickness evolution between two drops in the presence of surfactants. x denotes the surfactant concentration scaled by the theoretical maximum. Reproduced from [23].	20
1.12	Different properties governing the coalescence process. Reproduced from [9].	21
1.13	Different experimental techniques to characterise the evolution of a coalescing emulsion. Reproduced from [9].	23

2.1	Different types of mesh available in Basilisk.	26
2.2	Quadtree adaptive grid.	27
2.3	Children of a coarse cell.	28
2.4	The grey colored continuous interface is reconstructed by defragmented red colored lines using PLIC. Reproduced from [38].	32
2.5	The one dimensional advection of the 2D interface. The gray area represents the flux. Reproduced from [39].	32
2.6	Connected regions (i.e. droplets) to which will be assigned unique values.	34
2.7	Two drops with different colors. Here each color indicates an unique identity.	35
2.8	Relaxation at resolution boundaries.	36
2.9	Initially drops are assigned unique random numbers. It is then necessary to reduce this range to the maximum number of drops.	36
2.10	Drops with each uniquely assigned numbers, where these numbers range from 1 to the number of drops.	38
2.11	Droplets with the same tag value. Here the color of each droplet corresponds to different tag values. We can see the same tag value for two different droplets represented by the same blue color for two droplets.	39
2.12	Droplets with different tag values.	39
2.13	Color functions at multiple layers. Overlapping fields can be represented by combination of this fields. Each cell has a maximum of one interface. Reproduced from [44].	40
2.14	A graph and its proper colouring where the vertices are colored with the minimum number of colors so that any two vertices connected by an edge do not have the same color. Reproduced from [45].	41
2.15	Different types of planar graphs Reproduced from [45].	41
2.16	A planar graph representing packed circles. Reproduced from [46].	42
2.17	USA map coloring all of its states so that no adjacent states at each boundary have same color. Reproduced from [47].	42
2.18	Non coalescing droplets.	43
2.19	The drops associated to two different VOF tracers (f1 and f2).	43
2.20	Listing the drops that are two cell (or less) distance away from each other. The numbers on the drops represents their unique identity (tag values).	44
2.21	An array storing the closely located drops neighboring tracers information.	44
2.22	Replacing the VOF tracer (f1) of drop 1 with the other tracer (f2) corresponding to a non neighboring drop.	45
2.23	Drops colored differently such that no two interacting drops have the same color. These are essentially non-coalescing drops.	46
2.24	Data structure representation that stores the information of pairs of drops being tracked.	47
2.25	The drops and control coalescence data structure List 1 with one pair P1 at time $t - dt$	48
2.26	The non-coalescence function is passed at time t after interface advection changing the color function of the closely located drops.	48

2.27	Droplets with different VOF tracers represented by different colors.	49
2.28	Listing the information of the pairs of drops that are in close contact at time t	49
2.29	The centroid and the velocity of a pair of drops.	50
2.30	Matching the drops in List 1 at $t-dt$ to the List 2 at t . Information of drops in List 1 is update when matched to List 2. Unmatched elements in List 2 are added as new elements in List 1.	51
2.31	Detecting the pair of drops over time via motion of centroid. The dotted lined interface corresponds to the time $t-dt$ and continuous lined interface to the t	51
2.32	The contact time of the pairs of drops in List 1 is compared to the Drainage time (an input parameter suggesting coalescence). The pairs that meets the criteria are listed and allowed to coalesce.	51
2.33	Control coalescence algorithm.	54
3.1	An L 2D square domain consisting of two phases, where drops are distributed in an hexagonal packing with a slight perturbation.	56
3.2	$\frac{L}{D} = 52$ initialized with the same parameters (except the number of drops) as described in Figure 3.1.	57
3.3	A 2D domain with $\frac{L}{D} = 156$ in hexagonal packing as shown in 3.3a. The area corresponding to the white colored box in 3.3a is zoomed by 2.3x and displayed in Figure 3.3b.	58
3.4	A 2D domain with $\frac{L}{D} = 156$ at settling stage corresponding to simulation time $t = 40$. The different subdomains are presented in Figures 3.4b, 3.4c and 3.4d with border colors corresponding to the regions of the same color in the whole domain shown in Figure 3.4a. In subdomains the drops are red and the surrounding phase is colored with the magnitude of the y-velocity ranging from $[-0.1 : 0.1]U$ (blue to red).	60
3.5	A 2D domain with $\frac{L}{D} = 156$ at intermediate stage corresponding to simulation time $t = 140$. Full domain in Figure 3.5a with 3 colored regions zoomed by 3x (partial domains) in Figures 3.5b, 3.5c and 3.5d. Vertical channels appear in this stage with limited numerical coalescence.	62
3.6	A 2D domain with $\frac{L}{D} = 156$ at coalescence stage corresponding to simulation time $t = 200$. Full domain in Figure 3.6a with the 3 colored box regions zoomed by 3x in Figures 3.6b, 3.6c and 3.6d. Significant (numerical) coalescence occurs in this stage with a significant effect on the droplet size distribution.	63
3.7	A 2D domain with $\frac{L}{D} = 156$ at the filaments stage corresponding to simulation time $t = 305$. Full domain in Figure 3.7a with 3 colored box regions zoomed by 3x in Figure 3.7b, 3.7c and 3.7d.	64
3.8	A 2D domain with $\frac{L}{D} = 156$ at separated stage corresponding to simulation time $t = 900$. In this stage the two phases are completely separated except for the presence of tiny droplets.	65
3.9	Profiling of field values along the vertical direction of a 2D L square domain in bins numbered 1, 2, 3,...,N, where each bin height is $\frac{L}{N}$	66

3.10	Density profile at the initial time of the simulation, where the vertical axis is the vertical position normalized with the domain size, $\frac{y}{L}$ and the horizontal axis corresponds to the average volume fraction.	67
3.11	Density profiles at different simulation times $t = 500$ and $t = 900$, depicting the settling of drops.	67
3.12	Leading and trailing edge evolution of an emulsion of $\frac{L}{D} = 13$ settling under gravity. Depiction of the phase fronts known as the trailing edge and the leading edge at different time intervals $t = 0$, $t = 40$, $t = 140$ and $t = 200$ corresponding to Figure 3.12a, 3.12b, 3.12c and 3.12d respectively.	68
3.13	Leading and trailing edge evolution of the 14400-drops simulation computed with the help of density profiles. Three density profiles at time $t = 0$, 500 and 900 are shown along with their trailing and leading edge position on the separation front curve represented by colored drops. The blue dot on the density profile at $t = 0$ corresponds to the trailing edge at $t = 0$, similarly the red dot on the density profile at $t = 500$ corresponds to the trailing edge at $t = 500$, similarly for the leading edge with the black dot. Repeating this at the desired time intervals result in the separation front curve evolution over time as shown in Figure 3.13d.	70
3.14	Trailing and leading edge propagation curve in a coalescing emulsion of $\frac{L}{D} = 156$	71
3.15	Evolution of the number of drops in a coalescing emulsion of $\frac{L}{D} = 156$	72
3.16	Coalescence frequency evolution over time for the case with $\frac{L}{D} = 156$. This is computed as the rate of change of number of drops over time from Figure 3.15.	72
3.17	Evolution of the trailing edge corresponding to the emulsion simulation of $\frac{L}{D} = 13$ for three different resolutions: 20, 40 and 80 points per drop diameter. The first coalescence corresponding to these three test cases are represented by circular dots.	74
3.18	Evolution of the number of drops corresponding to the emulsion simulation of $\frac{L}{D} = 13$ for three different resolutions: 20, 40 and 80 points per drop diameter.	74
3.19	Simulation snapshots corresponding to $\frac{L}{D} = 52, 156$ at simulation times $t = 140$, $t = 200$ and $t = 305$. Drops are red colored in the $\frac{L}{D} = 52$ case. The surrounding phase in the $\frac{L}{D} = 52$ case and both phases in the $\frac{L}{D} = 156$ case are represented by the y-velocity field. The color scale for the y-velocity is between blue to red for a magnitude in $[-0.1 : 0.1]U$. The colored boxed regions of the $\frac{L}{D} = 156$ case in Figure 3.19a, 3.19b and 3.19c are subdomains corresponding to the $\frac{L}{D} = 52$ case. Similarly the colored boxed regions of the $\frac{L}{D} = 52$ case in Figure 3.19d, 3.19e and 3.19f are subdomains corresponding to the $\frac{L}{D} = 13$ case. The subdomains are presented in Figure 3.20, 3.21, 3.22, 3.21 and 3.24 with colored borders which exactly correspond to the same colored box in the full domain.	75

3.20	Comparison of a domain $\frac{L}{D} = 13$ to the subdomains of 52 case at $t = 140$ corresponding to an intermediate stage. The regions of subscaling corresponds to the colored boxes in Figure 3.19. Drops are red and the surrounding phase is colored with the magnitude of the y-velocity ranging from $[-0.1 : 0.1]U$ (blue to red).	77
3.21	Comparison of a domain $\frac{L}{D} = 52$ to the subdomains of the 156 case at $t = 140$ corresponding to an intermediate stage. The regions of subscaling correspond to the colored boxes in Figure 3.19.	78
3.22	Comparison of a domain $\frac{L}{D} = 13$ to the subdomains of the 52 case at $t = 200$ corresponding to the coalescence stage. The regions of subscaling corresponds to the colored boxes in Figure 3.19.	79
3.23	Comparison of a domain $\frac{L}{D} = 52$ to the subdomains of the 156 case at $t = 200$ corresponding to the coalescence stage. The regions of subscaling corresponds to the colored boxes in Figure 3.19.	80
3.24	Comparison of a domain $\frac{L}{D} = 52$ to the subdomains of the 156 case at $t = 305$ corresponding to the filament stage. The regions of subscaling correspond to the colored boxes in Figure 3.19.	81
3.25	Trailing edge evolution for three different domains corresponding to $\frac{L}{D} = 13, 52, 156$. The numerical resolution is 20 to 25 points per drop.	82
3.26	The number of drops evolution for three different domains $\frac{L}{D} = 13, 52, 156$. Numerical resolution is 20 to 25 points per drop.	82
3.27	Drift y-velocity evolution of the three different domains $\frac{L}{D} = 13, 52, 156$. The characteristic length scale is chosen to be the droplet diameter D . Mesh resolution is 20 to 25 points per drop. The dots represents the first coalescence event.	84
3.28	Drift y-velocity evolution for three different domains $\frac{L}{D} = 13, 52, 156$. The characteristic length scale is chosen to be the domain size L . Mesh resolution is 20 to 25 points per drop.	85
3.29	A 2D 52×52 two-phase flow domain with $\frac{L}{D} = 52$.	85
3.30	Evolution of a $\frac{L}{D} = 52$ non-coalescing emulsion at the different simulation times corresponding to the different stages. Both phases are colored with the magnitude of the y-velocity ranging from $[-0.1 : 0.1]U$ (blue to red).	86
3.31	Non-coalescing emulsion corresponding to the three different domains at simulation time $t = 156$.	89
3.32	Non-coalescing emulsion corresponding to the three different domains at simulation time $t = 406$.	90
3.33	Non-coalescing emulsion corresponding to the two different domains ($\frac{L}{D} = 52$ & 104) at simulation time $t = 1500$ and a $\frac{L}{D} = 13$ simulation at time $t = 500$.	91
3.34	The evolution of the trailing edge of a $\frac{L}{D} = 13$ non-coalescing emulsion for three different resolutions.	92
3.35	The evolution of the trailing edge of the non-coalescing emulsions corresponding to three different domain sizes. Where $\frac{L}{D} = 13$ & 52 are resolved by 40 points per diameter and $\frac{L}{D} = 104$ by 20 points per diameter. The trailing edge corresponding to the $\frac{L}{D} = 13$ has been shifted vertically down to match the initial points of the $\frac{L}{D} = 52$ & 156 cases.	93

3.36	A 2D 13×13 domain of $\frac{L}{D} = 13$	94
3.37	A 2D domain of $\frac{L}{D} = 13$ with numerical resolution of 20 points per diameter at simulation time $t = 150$. Both phases are colored with the magnitude of the y-velocity ranging from $[-0.1 : 0.1]U$ (blue to red).	95
3.38	Trailing edge evolution for three different controlled coalescence test cases corresponding to the drainage time 0.1, 1, and 5. The colored dots correspond to the first coalescence. The red square at $t = 150$ corresponds to the Figure 3.37b.	96
3.39	Evolution of the number of drops for three different controlled coalescence test cases corresponding to the drainage times 0.1, 1 and 5	97
3.40	The trailing edge evolution of a 2D emulsion for the coalescing, the non-coalescing and the controlled coalescing model. The coalescing emulsions are shown in green circles and black squares, the non-coalescing emulsion is shown in purple squares and the controlled-coalescing emulsions are shown by three different colored lines with the corresponding drainage time. The numerical resolution of the controlled-coalescing emulsion is 20 points per diameter.	98
3.41	The number of drops evolution of a 2D $\frac{L}{D} = 13$ emulsion for the coalescing and controlled-coalescing emulsions. The coalescing emulsions are shown with different colored lines along with their numerical resolution. The controlled-coalescing emulsions are shown with colored dots with their drainage time. Their numerical resolution is 20 points per diameter.	99

List of Tables

3.1	Simulation parameters.	58
3.2	Simulation parameters corresponding to the $\frac{L}{D} = 156$ test case.	59
3.3	Simulation parameters corresponding to $\frac{L}{D} = 13, 52, 156$ test cases.	76
3.4	The simulation parameters corresponding to the non-coalescence simulations.	84
3.5	Computational cost and number of VOF tracer for the non-coalescence simulations.	88
3.6	Simulation parameters corresponding to $\frac{L}{D} = 13$ control coalescence test case.	95

Listings

2.1 tag()	34
-----------------	----

Bibliography

- [1] *The Food Section - Food News, Recipes, and More*. URL: <https://www.thefoodsection.com/foodsection/2008/11/fact-checking-t.html>.
- [2] Tom Frising et al. “Contribution of the Sedimentation and Coalescence Mechanisms to the Separation of Concentrated Water-in-Oil Emulsions”. en. In: *Journal of Dispersion Science and Technology* 29.6 (June 2008), pp. 827–834. ISSN: 0193-2691, 1532-2351. DOI: [10.1080/01932690701781501](https://doi.org/10.1080/01932690701781501). URL: <http://www.tandfonline.com/doi/abs/10.1080/01932690701781501>.
- [3] Christine Noïk, Thierry Palermo, and Christine Dalmazzone. “Modeling of Liquid/Liquid Phase Separation: Application to Petroleum Emulsions”. en. In: *Journal of Dispersion Science and Technology* 34.8 (Aug. 2013), pp. 1029–1042. ISSN: 0193-2691, 1532-2351. DOI: [10.1080/01932691.2012.735929](https://doi.org/10.1080/01932691.2012.735929). URL: <http://www.tandfonline.com/doi/abs/10.1080/01932691.2012.735929>.
- [4] Tom Frising, Christine Noïk, and Christine Dalmazzone. “The Liquid/Liquid Sedimentation Process: From Droplet Coalescence to Technologically Enhanced Water/Oil Emulsion Gravity Separators: A Review”. en. In: *Journal of Dispersion Science and Technology* 27.7 (Oct. 2006), pp. 1035–1057. ISSN: 0193-2691, 1532-2351. DOI: [10.1080/01932690600767098](https://doi.org/10.1080/01932690600767098). URL: <http://www.tandfonline.com/doi/abs/10.1080/01932690600767098>.
- [5] D. Langevin et al. “Crude Oil Emulsion Properties and Their Application to Heavy Oil Transportation”. en. In: *Oil & Gas Science and Technology* 59.5 (Sept. 2004), pp. 511–521. ISSN: 1294-4475. DOI: [10.2516/ogst:2004036](https://doi.org/10.2516/ogst:2004036). URL: <http://ogst.ifpenergiesnouvelles.fr/10.2516/ogst:2004036>.
- [6] Fatemeh Goodarzi and Sohrab Zendehboudi. “A Comprehensive Review on Emulsions and Emulsion Stability in Chemical and Energy Industries”. en. In: *The Canadian Journal of Chemical Engineering* 97.1 (Jan. 2019), pp. 281–309. ISSN: 0008-4034, 1939-019X. DOI: [10.1002/cjce.23336](https://doi.org/10.1002/cjce.23336). URL: <https://onlinelibrary.wiley.com/doi/abs/10.1002/cjce.23336>.
- [7] *Produced Water Treatment & Recovery Companies — SAMCO*. en-US. URL: <https://www.samcotech.com/samco-innovations/platform-oil-gas-recovery/produced-water-treatment-recovery/>.
- [8] H. Pirouz Kavehpour. “Coalescence of Drops”. In: *Annual Review of Fluid Mechanics* 47.1 (2015). eprint: <https://doi.org/10.1146/annurev-fluid-010814-014720>, pp. 245–268. DOI: [10.1146/annurev-fluid-010814-014720](https://doi.org/10.1146/annurev-fluid-010814-014720). URL: <https://doi.org/10.1146/annurev-fluid-010814-014720>.

- [9] Johannes Kamp, Jörn Villwock, and Matthias Kraume. “Drop coalescence in technical liquid/liquid applications: a review on experimental techniques and modeling approaches”. en. In: *Reviews in Chemical Engineering* 33.1 (Jan. 2017), pp. 1–47. ISSN: 2191-0235, 0167-8299. DOI: [10.1515/revce-2015-0071](https://doi.org/10.1515/revce-2015-0071). URL: <https://www.degruyter.com/view/j/revce.2017.33.issue-1/revce-2015-0071/revce-2015-0071.xml>.
- [10] *Delft University of Technology - Product and Process Engineering*. URL: <https://cheme.nl/ppe/people/shah.shtml>.
- [11] *Basilisk - Basilisk*. URL: <http://basilisk.fr/>.
- [12] Sandrine Poteau et al. “Influence of pH on Stability and Dynamic Properties of Asphaltenes and Other Amphiphilic Molecules at the OilWater Interface †”. en. In: *Energy & Fuels* 19.4 (July 2005), pp. 1337–1341. ISSN: 0887-0624, 1520-5029. DOI: [10.1021/ef0497560](https://doi.org/10.1021/ef0497560). URL: <https://pubs.acs.org/doi/10.1021/ef0497560>.
- [13] Yin-Ting Hu et al. “Techniques and methods to study functional characteristics of emulsion systems”. en. In: *Journal of Food and Drug Analysis* 25.1 (Jan. 2017), pp. 16–26. ISSN: 10219498. DOI: [10.1016/j.jfda.2016.10.021](https://doi.org/10.1016/j.jfda.2016.10.021). URL: <https://linkinghub.elsevier.com/retrieve/pii/S1021949816301831>.
- [14] Ivan Fortelný and Josef Jůza. “Description of the Droplet Size Evolution in Flowing Immiscible Polymer Blends”. en. In: *Polymers* 11.5 (May 2019). Number: 5 Publisher: Multidisciplinary Digital Publishing Institute, p. 761. DOI: [10.3390/polym11050761](https://doi.org/10.3390/polym11050761). URL: <https://www.mdpi.com/2073-4360/11/5/761>.
- [15] *Principles of Colloid and Surface Chemistry, Revised and Expanded*. en. URL: <https://www.routledge.com/Principles-of-Colloid-and-Surface-Chemistry-Revised-and-Expanded/Hiemenz-Rajagopalan/p/book/9780824793975>.
- [16] Derek Y. C. Chan, Evert Klaseboer, and Rogerio Manica. “Film drainage and coalescence between deformable drops and bubbles”. en. In: *Soft Matter* 7.6 (2011), pp. 2235–2264. ISSN: 1744-683X, 1744-6848. DOI: [10.1039/C0SM00812E](https://doi.org/10.1039/C0SM00812E). URL: <http://xlink.rsc.org/?DOI=C0SM00812E>.
- [17] J. M. Frostad, J. Walter, and L. G. Leal. “A scaling relation for the capillary-pressure driven drainage of thin films”. en. In: *Physics of Fluids* 25.5 (May 2013), p. 052108. ISSN: 1070-6631, 1089-7666. DOI: [10.1063/1.4807069](https://doi.org/10.1063/1.4807069). URL: <http://aip.scitation.org/doi/10.1063/1.4807069>.
- [18] R.S Allan, G.E Charles, and S.G Mason. “The approach of gas bubbles to a gas/liquid interface”. en. In: *Journal of Colloid Science* 16.2 (Apr. 1961), pp. 150–165. ISSN: 00958522. DOI: [10.1016/0095-8522\(61\)90014-9](https://doi.org/10.1016/0095-8522(61)90014-9). URL: <https://linkinghub.elsevier.com/retrieve/pii/0095852261900149>.
- [19] Dirk G. A. L. Aarts, Matthias Schmidt, and Henk N. W. Lekkerkerker. “Direct Visual Observation of Thermal Capillary Waves”. In: *Science* 304.5672 (2004). Publisher: American Association for the Advancement of Science _eprint: <https://science.sciencemag.org/> pp. 847–850. ISSN: 0036-8075. DOI: [10.1126/science.1097116](https://doi.org/10.1126/science.1097116). URL: <https://science.sciencemag.org/content/304/5672/847>.

- [20] Dirk G. A. L. Aarts and Henk N. W. Lekkerkerker. “Droplet coalescence: drainage, film rupture and neck growth in ultralow interfacial tension systems”. en. In: *Journal of Fluid Mechanics* 606 (July 2008), pp. 275–294. ISSN: 0022-1120, 1469-7645. DOI: [10.1017/S0022112008001705](https://doi.org/10.1017/S0022112008001705). URL: https://www.cambridge.org/core/product/identifier/S0022112008001705/type/journal_article.
- [21] A.N. Zdravkov, G.W.M. Peters, and H.E.H. Meijer. “Film drainage and interfacial instabilities in polymeric systems with diffuse interfaces”. en. In: *Journal of Colloid and Interface Science* 296.1 (Apr. 2006), pp. 86–94. ISSN: 00219797. DOI: [10.1016/j.jcis.2005.08.062](https://doi.org/10.1016/j.jcis.2005.08.062). URL: <https://linkinghub.elsevier.com/retrieve/pii/S0021979705009136>.
- [22] Sara Navarro Arredondo. “Modeling Disjoining pressure using Dissipative Particle Dynamics (DPD)”. en. In: (), p. 32.
- [23] Pieter J. A. Janssen and Patrick D. Anderson. “Modeling Film Drainage and Coalescence of Drops in a Viscous Fluid”. en. In: *Macromolecular Materials and Engineering* 296.3-4 (Mar. 2011), pp. 238–248. ISSN: 14387492. DOI: [10.1002/mame.201000375](https://doi.org/10.1002/mame.201000375). URL: <http://doi.wiley.com/10.1002/mame.201000375>.
- [24] John M. Frostad, Alexandra Paul, and L. Gary Leal. “Coalescence of droplets due to a constant force interaction in a quiescent viscous fluid”. en. In: *Physical Review Fluids* 1.3 (July 2016), p. 033904. ISSN: 2469-990X. DOI: [10.1103/PhysRevFluids.1.033904](https://doi.org/10.1103/PhysRevFluids.1.033904). URL: <https://link.aps.org/doi/10.1103/PhysRevFluids.1.033904>.
- [25] L. G. Leal. “Flow induced coalescence of drops in a viscous fluid”. en. In: *Physics of Fluids* 16.6 (June 2004), pp. 1833–1851. ISSN: 1070-6631, 1089-7666. DOI: [10.1063/1.1701892](https://doi.org/10.1063/1.1701892). URL: <http://aip.scitation.org/doi/10.1063/1.1701892>.
- [26] Stéphane Popinet. “Numerical Models of Surface Tension”. en. In: *Annual Review of Fluid Mechanics* 50.1 (Jan. 2018), pp. 49–75. ISSN: 0066-4189, 1545-4479. DOI: [10.1146/annurev-fluid-122316-045034](https://doi.org/10.1146/annurev-fluid-122316-045034). URL: <http://www.annualreviews.org/doi/10.1146/annurev-fluid-122316-045034>.
- [27] *Basilisk - src/two-phase.h*. URL: <http://basilisk.fr/src/two-phase.h>.
- [28] Stéphane Popinet. “An accurate adaptive solver for surface-tension-driven interfacial flows”. en. In: *Journal of Computational Physics* 228.16 (Sept. 2009), pp. 5838–5866. ISSN: 00219991. DOI: [10.1016/j.jcp.2009.04.042](https://doi.org/10.1016/j.jcp.2009.04.042). URL: <https://linkinghub.elsevier.com/retrieve/pii/S002199910900240X>.
- [29] Stéphane Popinet. “Gerris: a tree-based adaptive solver for the incompressible Euler equations in complex geometries”. en. In: *Journal of Computational Physics* 190.2 (Sept. 2003), pp. 572–600. ISSN: 00219991. DOI: [10.1016/S0021-9991\(03\)00298-5](https://doi.org/10.1016/S0021-9991(03)00298-5). URL: <https://linkinghub.elsevier.com/retrieve/pii/S0021999103002985>.

- [30] John B Bell, Phillip Colella, and Harland M Glaz. “A second-order projection method for the incompressible navier-stokes equations”. en. In: *Journal of Computational Physics* 85.2 (Dec. 1989), pp. 257–283. ISSN: 00219991. DOI: [10.1016/0021-9991\(89\)90151-4](https://doi.org/10.1016/0021-9991(89)90151-4). URL: <https://linkinghub.elsevier.com/retrieve/pii/0021999189901514>.
- [31] J.U Brackbill, D.B Kothe, and C Zemach. “A continuum method for modeling surface tension”. en. In: *Journal of Computational Physics* 100.2 (June 1992), pp. 335–354. ISSN: 00219991. DOI: [10.1016/0021-9991\(92\)90240-Y](https://doi.org/10.1016/0021-9991(92)90240-Y). URL: <https://linkinghub.elsevier.com/retrieve/pii/002199919290240Y>.
- [32] Seungwon Shin, Ikroh Yoon, and Damir Juric. “The Local Front Reconstruction Method for direct simulation of two- and three-dimensional multiphase flows”. en. In: *Journal of Computational Physics* 230.17 (July 2011), pp. 6605–6646. ISSN: 00219991. DOI: [10.1016/j.jcp.2011.04.040](https://doi.org/10.1016/j.jcp.2011.04.040). URL: <https://linkinghub.elsevier.com/retrieve/pii/S0021999111002981>.
- [33] J. A. Sethian and Peter Smereka. “Level set methods for fluid interfaces”. In: *Annual Review of Fluid Mechanics* 35.1 (Jan. 2003). Publisher: Annual Reviews, pp. 341–372. ISSN: 0066-4189. DOI: [10.1146/annurev.fluid.35.101101.161105](https://doi.org/10.1146/annurev.fluid.35.101101.161105). URL: <https://www.annualreviews.org/doi/10.1146/annurev.fluid.35.101101.161105>.
- [34] C.W Hirt and B.D Nichols. “Volume of fluid (VOF) method for the dynamics of free boundaries”. en. In: *Journal of Computational Physics* 39.1 (Jan. 1981), pp. 201–225. ISSN: 00219991. DOI: [10.1016/0021-9991\(81\)90145-5](https://doi.org/10.1016/0021-9991(81)90145-5). URL: <https://linkinghub.elsevier.com/retrieve/pii/0021999181901455>.
- [35] Mark Sussman and Elbridge Gerry Puckett. “A Coupled Level Set and Volume-of-Fluid Method for Computing 3D and Axisymmetric Incompressible Two-Phase Flows”. en. In: *Journal of Computational Physics* 162.2 (Aug. 2000), pp. 301–337. ISSN: 00219991. DOI: [10.1006/jcph.2000.6537](https://doi.org/10.1006/jcph.2000.6537). URL: <https://linkinghub.elsevier.com/retrieve/pii/S0021999100965379>.
- [36] Grétar Tryggvason, Ruben Scardovelli, and Stéphane Zaleski. *Direct Numerical Simulations of Gas–Liquid Multiphase Flows*. Cambridge: Cambridge University Press, 2011. ISBN: 978-0-521-78240-1. DOI: [10.1017/CB09780511975264](https://doi.org/10.1017/CB09780511975264). URL: <https://www.cambridge.org/core/books/direct-numerical-simulations-of-gasliquid-multiphase-flows/C6282C4E426F95C1AC8642DA7569CF0C>.
- [37] E. Aulisa et al. “Interface reconstruction with least-squares fit and split advection in three-dimensional Cartesian geometry”. en. In: *Journal of Computational Physics* 225.2 (Aug. 2007), pp. 2301–2319. ISSN: 00219991. DOI: [10.1016/j.jcp.2007.03.015](https://doi.org/10.1016/j.jcp.2007.03.015). URL: <https://linkinghub.elsevier.com/retrieve/pii/S0021999107001325>.
- [38] *Fichier:Vof scheme with plic.png*. fr. URL: https://fr.wikipedia.org/wiki/Fichier:Vof_scheme_with_plic.png.
- [39] Stephane Popinet. “Lecture notes Introduction to numerical methods for interfacial flows”. en. In: (), p. 17.

- [40] G.D. Weymouth and Dick K.-P. Yue. “Conservative Volume-of-Fluid method for free-surface simulations on Cartesian-grids”. en. In: *Journal of Computational Physics* 229.8 (Apr. 2010), pp. 2853–2865. ISSN: 00219991. DOI: [10.1016/j.jcp.2009.12.018](https://doi.org/10.1016/j.jcp.2009.12.018). URL: <https://linkinghub.elsevier.com/retrieve/pii/S0021999109006974>.
- [41] Emil Coyajee and Bendiks Jan Boersma. “Numerical simulation of drop impact on a liquid–liquid interface with a multiple marker front-capturing method”. en. In: *Journal of Computational Physics* 228.12 (July 2009), pp. 4444–4467. ISSN: 00219991. DOI: [10.1016/j.jcp.2009.03.014](https://doi.org/10.1016/j.jcp.2009.03.014). URL: <https://linkinghub.elsevier.com/retrieve/pii/S0021999109001363>.
- [42] Marcel Kwakkel, Wim-Paul Breugem, and Bendiks Jan Boersma. “An efficient multiple marker front-capturing method for two-phase flows”. en. In: *Computers & Fluids* 63 (June 2012), pp. 47–56. ISSN: 00457930. DOI: [10.1016/j.compfluid.2012.04.004](https://doi.org/10.1016/j.compfluid.2012.04.004). URL: <https://linkinghub.elsevier.com/retrieve/pii/S004579301200134X>.
- [43] A. H. Rajkotwala et al. “Extension of local front reconstruction method with controlled coalescence model”. en. In: *Physics of Fluids* 30.2 (Feb. 2018), p. 022102. ISSN: 1070-6631, 1089-7666. DOI: [10.1063/1.5008371](https://doi.org/10.1063/1.5008371). URL: <http://aip.scitation.org/doi/10.1063/1.5008371>.
- [44] Petr Karnakov et al. “Aphros: High Performance Software for Multiphase Flows with Large Scale Bubble and Drop Clusters”. en. In: *Proceedings of the Platform for Advanced Scientific Computing Conference*. Geneva Switzerland: ACM, June 2020, pp. 1–10. ISBN: 978-1-4503-7993-9. DOI: [10.1145/3394277.3401856](https://doi.org/10.1145/3394277.3401856). URL: <https://dl.acm.org/doi/10.1145/3394277.3401856>.
- [45] *A guide to graph colouring*. en. New York, NY: Springer Berlin Heidelberg, 2015. ISBN: 978-3-319-25728-0.
- [46] Dcoetzee. *English: An illustration of the circle packing theorem on the planar graph of K5 (the complete graph on five vertices) minus one edge. The positions and colors of the vertices in the top graph and the circles in the bottom drawing correspond; any two vertices with an edge between them in the top graph have their corresponding circles touching at a tangent in the bottom drawing. The interiors of all circles are disjoint.* June 2010. URL: https://commons.wikimedia.org/wiki/File:Circle_packing_theorem_K5_minus_edge_example.svg.
- [47] *Four color theorem*. en. Page Version ID: 987792922. Nov. 2020. URL: https://en.wikipedia.org/w/index.php?title=Four_color_theorem&oldid=987792922.
- [48] Lachlan R Mason, Geoffrey W Stevens, and Dalton J E Harvie. “MULTI-SCALE VOLUME OF FLUID MODELLING OF DROPLET COALESCENCE”. en. In: (2012), p. 6.
- [49] Marcel Kwakkel, Wim-Paul Breugem, and Bendiks Jan Boersma. “Extension of a CLSVOF method for droplet-laden flows with a coalescence/breakup model”. en. In: *Journal of Computational Physics* 253 (Nov. 2013), pp. 166–188. ISSN: 00219991. DOI: [10.1016/j.jcp.2013.07.005](https://doi.org/10.1016/j.jcp.2013.07.005). URL: <https://linkinghub.elsevier.com/retrieve/pii/S0021999113004762>.

- [50] *Graph coloring*. en. Page Version ID: 977178387. Sept. 2020. URL: https://en.wikipedia.org/w/index.php?title=Graph_coloring&oldid=977178387.